THE UNIVERSITY OF QUEENSLAND

AUSTRALIA

Aerodynamic Force Interactions and Measurements for Micro Quadrotors

Edwin Blaize Davis

BEngHons

A thesis submitted for the degree of Doctor of Philosophy at

The University of Queensland in 2018

School of Information Technology and Electrical Engineering

Abstract

Unmanned Aerial Vehicles (UAVs) have become mainstream through the success of several large commercial drone manufacturers. Quadrotors have been widely adopted due to their mechanical simplicity, ability to take off from a small area and hover at a fixed location. As these aircraft are increasingly being used in urban environments and indoors their ability to maintain stable flight in the presence of disturbances and nearby obstacles is of growing importance.

Understanding the aerodynamics acting in these environments is the first step to improving quadrotor behaviour. This presents a challenge, as to characterise and verify models of the aerodynamic phenomena it is essential to collect numerous consistent experimental data points. On a typical quadrotor the motor response changes as the battery discharges, leading to variation in flight performance. Typically, this is addressed through the use high gain feedback control regulating attitude and position. To overcome this a unique voltage regulator for quadrotor power was developed to maintain constant supply voltage over the quadrotors flight. This enables the quadrotor to produce consistent and repeatable behaviour as the battery discharges.

One way to improve the performance of quadrotors flying in constrained environments with limited sensing is to exploit aerodynamic effects for passive control and stability. Ground effect and rotor inflow damping are two effects of interest: ground effect provides a quadratic increase in thrust as a rotor moves closer to the ground; rotor inflow damping acts to resist axial motion by causing a change thrust opposing the movement. By canting the rotors of a quadrotor these effects were brought from the vertical axis into the lateral axis as well. A canted quadrotor flying over a v-shaped channel was modeled and found to exhibit passive stability in position. A demonstrator aircraft and v-shaped channel were tested in a number of configurations and shown to be stable for a channel slope of 10, 15 or 20 degrees with a rotor cant of 15 or 20 degrees.

In order to observe more subtle aerodynamic effects, such as wall effect, it is necessary to have a method to measure rotor forces directly during quadrotor flight. Existing force torque sensors are too bulky, heavy, expensive or insensitive. To overcome these limitations a novel force torque sensor was developed that costs less than $50, weighs 3 g and is capable of measuring sub mN forces. These sensors utilise an array of micro-electro-mechanical system (MEMS) barometers encapsulated in rubber to measure the strain field imparted by forces acting on the

attached load plate. Mounting force torque sensors under the motors of a quadrotor allows the lateral rotor forces to be transmitted through the motor body and measured as torques at the base.

Closely related to this, one of the key limitations faced by quadrotors is their inability to directly measure the airspeed of the aircraft. Providing an oncoming wind speed measurement will allow them to compensate for disturbances improving trajectory tracking and gust rejection. Blade flapping and induced drag are aerodynamic phenomena which relate lateral motion to a force acting in opposition to the rotors motion. By measuring this force using a rotor force sensor the airspeed of the aircraft is computed directly using induced drag and rotor blade flapping models. It was found that lateral velocity could be measured for the velocities tested, up to 1.5 ms^{-1}, and showed a strong linear relationship to ground truth measurements.

The work of this thesis has led to the development of: a quadrotor platform for consistent flight behaviour; a passive position-keeping quadrotor; and a novel rotor force sensor for direct measurement of quadrotor airspeed. These technologies open up avenues to improve the flight performance of quadrotors and better understand subtle aerodynamic interactions in flight.

Declaration by the author

This thesis is composed of my original work, and contains no material previously published or written by another person except where due reference has been made in the text. I have clearly stated the contribution by others to jointly-authored works that I have included in my thesis.

I have clearly stated the contribution of others to my thesis as a whole, including statistical assistance, survey design, data analysis, significant technical procedures, professional editorial advice, and any other original research work used or reported in my thesis. The content of my thesis is the result of work I have carried out since the commencement of my research higher degree candidature and does not include a substantial part of work that has been submitted to qualify for the award of any other degree or diploma in any university or other tertiary institution. I have clearly stated which parts of my thesis, if any, have been submitted to qualify for another award.

I acknowledge that an electronic copy of my thesis must be lodged with the University Library and, subject to the policy and procedures of The University of Queensland, the thesis be made available for research and study in accordance with the Copyright Act 1968 unless a period of embargo has been approved by the Dean of the Graduate School.

I acknowledge that copyright of all material contained in my thesis resides with the copyright holder(s) of that material. Where appropriate I have obtained copyright permission from the copyright holder to reproduce material in this thesis.

Publications during candidature

Edwin Davis, and P. E. I. Pounds. (2017). "Direct Sensing of Thrust and Velocity for a Quadrotor Rotor Array". *IEEE Robotics and Automation Letters*, 2(3), pp.1360-1366, IEEE.

Edwin Davis, and P. E. I. Pounds. (2016). "Direct Thrust and Velocity Measurement for a Micro UAV Rotor". In *Proc. Australasian Conference on Robotics and Automation*, Brisbane Australia, Dec 2016. ARAA. (Awarded Best Paper)

Edwin Davis, William Mackay-Lowndes, Dion Gonano, Scott Hansen, and P. E. I. Pounds. (2016). "Towards the Stackrotor: Aerodynamics, Construction, Dynamics and Control of a Vertical Stacked-Rotor Configuration for Indoor Heavy-Lift Helicopter Robots". In *Proc. Australasian Conference on Robotics and Automation*, Brisbane Australia, Dec 2016. ARAA. (Nominated Best Paper)

Edwin Davis, James Spollard, and P. E. I. Pounds. (2015). "Passive Height Stability and Trajectory Repeatability of a Quadrotor Maneuvering in Ground Effect with Regulated Voltage Bus". In *Proc. Australasian Conference on Robotics and Automation*, Canberra Australia, Dec 2015. ARAA. (Nominated Best Student Paper)

Edwin Davis, and P. E. I. Pounds. (2015). "Passive Position Control of a Quadrotor with Ground Effect Interaction". *IEEE Robotics and Automation Letters*, 1(1), pp.539-545, IEEE.

Edwin Davis, Ben E Nizette, and Changbin Yu. (2013). "Development of a Low Cost Quadrotor Platform for Swarm Experiments". In *Proc. Chinese Control Conference*, Xi'an China, Jul 2013. IEEE.

Provisional Patent #2016904834 "Force sensing device", inventors Edwin Davis, and P. E. I. Pounds, 2016.

Publications included in this thesis

Edwin Davis, and P. E. I. Pounds. (2017). "Direct Sensing of Thrust and Velocity for a Quadrotor Rotor Array". *IEEE Robotics and Automation Letters*, 2(3), pp.1360-1366, IEEE.
Incorporated in Chapter 5 as Section 5.4.

Contributor	Statement of contribution
Edwin Davis	Hardware development (100%) Experiment design and execution (100%) Theory (20%) Writing (40%)
Pauline Pounds	Theory (80%) Writing (60%)

Edwin Davis, and P. E. I. Pounds. (2016). "Direct Thrust and Velocity Measurement for a Micro UAV Rotor". In *Proc. Australasian Conference on Robotics and Automation*, Brisbane Australia, Dec 2016. ARAA.
Incorporated in Chapter 5 as Sections 5.1–5.3.

Contributor	Statement of contribution
Edwin Davis	Concept (40%) Experiments (95%) Hardware (100%) Analysis (50%) Writing (60%)
Pauline Pounds	Concept (60%) Experiments (5%) Analysis (50%) Writing (40%)

Edwin Davis, James Spollard, and P. E. I. Pounds. (2015). "Passive Height Stability and Trajectory Repeatability of a Quadrotor Maneuvering in Ground Effect with Regulated Voltage Bus". In *Proc. Australasian Conference on Robotics and Automation*, Canberra Australia, Dec 2015. ARAA.
Incorporated in Chapters 3 and 4 as Sections 3.1–4.2.

Contributor	Statement of contribution
Edwin Davis	Hardware (40%) Experiments (80%) Analysis (30%) Writing (45%)
James Spollard	Hardware (20%) Experiments (20%) Writing (10%)
Pauline Pounds	Hardware (40%) Analysis (70%) Writing (45%)

Edwin Davis, and P. E. I. Pounds. (2015). "Passive Position Control of a Quadrotor with Ground Effect Interaction". *IEEE Robotics and Automation Letters*, 1(1), pp.539-545, IEEE.
Incorporated in Chapter 4 as Sections 4.3–4.5.

Contributor	Statement of contribution
Edwin Davis	Hardware (90%) Design Experiments (50%) Conduct Experiments (90%) Writing (50%)
Pauline Pounds	Hardware (10%) Design Experiments (50%) Conduct Experiments (10%) Writing (50%)

Contributions by others to the thesis

No contributions by others

Statement of parts of the thesis submitted to qualify for the award of another degree

None

Acknowledgements

To Pauline, thank you. Your guidance has propelled me to this point and for that I am truly grateful. Your constant support, patience, understanding and kindness helped me through difficult times. As a mentor, the experience which you have shared will serve me well long into the future.

Rob, Henry and Brad, thank you for supporting me during my time at ANU and helping me through the transition to UQ. You all provided me with great experiences and advice. Steve, Michael, Surya and Janet, thank you for welcoming me to UQ and providing me with the advice that I needed. Will, thanks for hanging out with me on late nights in the lab.

I am so grateful to be surrounded by my family and friends on this journey. Ramona, you have been there for me since I first came to Brisbane. Thank you for supporting me and looking after me through it all, I can't imagine life without you. My sister, Nina, you are an amazing and inspiring friend. My parents, Heidi and Eric, you exposed me to science and technology from a young age and actively encouraged and supported my interest. This is the greatest gift, thank you.

Keywords

Quadrotor, Unmanned Aerial Vehicle (UAV), Force Sensor, Passive Dynamics, Aerodynamics

Australian and New Zealand Standard Research Classifications (ANZSRC)

ANZSRC code: 090602, Control Systems, Robotics and Automation, 100%

Field of Research (FoR) Classification

FoR code: 0906, Electronics and Electrical Engineering, 100%

Contents

List of Figures

List of Tables

List of Abbreviations

BEM	Blade Element Method
CCW	Counter Clockwise
COTS	Commercial-off-the-shelf
CW	Clockwise
EMF	Electromotive Force
ESC	Electronic Speed Controller
ESR	Equivalent Series Resistance
GPS	Global Positioning System
I2C	Inter-Integrated Circuit
IMU	Inertial Measurement Unit
IR	Infra Red
LiPo	Lithium-ion Polymer (Battery)
MEMS	Micro-Electro-Mechanical System
PID	Proportional–Integral–Derivative (Controller)
PWM	Pulse Width Modulation
RC	Radio Control
Rx	Receiver
SPI	Serial Peripheral Interface
Tx	Transmitter
UAS	Unmanned Aerial System
UAV	Unmanned Aerial Vehicle
UQ	University of Queensland
USB	Universal Serial Bus
VTOL	Vertical Take-off and Landing

Nomenclature

a	Blade lift slope, rad^{-1}
A	Rotor disc area, m^2
α	Variable blade angle of attack, rad
b	Blade drag slope, rad^{-1}
B	Rotor radius scaling parameter
C_d	Rotor drag coefficient
C_l	Rotor lift coefficient
C_P	Rotor power coefficient
C_Q	Rotor torque coefficient
C_T	Rotor thrust coefficient
χ	Channel angle, rad
d	Distance between rotor and channel, m
F	Applied force vector, N
g	Acceleration due to gravity, ms^{-2}
i	Motor current, A
I	Rotational inertia matrix, $\text{kg}\cdot\text{m}^2$
I_r	Rotor rotational inertia, $\text{kg}\cdot\text{m}^2$
k_d	Attitude feedback derivative gain
k_p	Attitude feedback proportional gain
λ	Motor flux-linkage coefficient
m	Vehicle mass, kg
m	Rotor system mass, kg
ω	Rotor rotational velocity, $\text{rad}\cdot\text{s}^{-1}$
Ω	Rotor rotational velocity, $\text{rad}\cdot\text{s}^{-1}$
Ω	Vehicle rotational velocity vector, $\text{rad}\cdot\text{s}^{-1}$
P	Rotor power, W

Q	Rotor torque, Nm
r	Quadrotor arm length, m
R	Rotor radius, m
R	Rotation matrix
R_d	Drive circuit resistance, Ω
ρ	Air density, kg·m^{-3}
σ	Rotor solidity ratio
T	Rotor thrust, N
T_{FA}	Rotor thrust in free air, N
T_{GE}	Rotor thrust in ground effect, N
T_h	Rotor thrust in hover, N
τ	Applied torque vector, Nm
θ	Pitch angle, rad
θ_{tip}	Blade tip angle of attack, rad
$\mathbf{v}$	Velocity vector, ms^{-1}
v_i	Rotor inflow velocity, ms^{-1}
V	Battery voltage, V
ϖ	Rotor cant angle, rad
x	X axis displacement, m
y	Y axis displacement, m
z	Z axis displacement, m
ζ	Position vector, m

Chapter 1

Introduction

Unmanned aerial vehicles (UAVs) are becoming a major technology in our society with a broad array of applications from agriculture through to emergency services and freight delivery. The current commercial and consumer UAV industry is valued at $2 billion and is expected to experience rapid growth over the next five years, to exceed $10 billion by the end of the decade [Dillow, 2014]. One UAV platform which is increasingly popular, especially in cities and urban spaces, is the quadrotor helicopter. Unlike conventional helicopters, quadrotors offer greater mechanical simplicity leading to a cheaper and more reliable platform [Pounds and Mahony, 2009].

Quadrotors operating in urban environments and indoors will be flying in close proximity to the ground and walls. Small-scale quadrotors could be used for many tasks, especially indoors and in hazardous environments or confined spaces — for example, flight inside of a power plant boiler for inspection and maintenance [Burri *et al*, 2012]. Operating conventional manned helicopters and fixed wing aircraft in close proximity to hazards such as power lines is well known to be dangerous [Low *et al*, 1991]. Similar situations when quadrotors are flying near obstacles could lead to unexpected aerodynamic behaviour and control instability, resulting in a crash. An obvious solution may be to equip the quadrotor with heavy and expensive sensors, such as laser scanners, which allow it to detect objects and thereby avoid them. However, this approach is not suitable for miniature aircraft which do not have the payload capacity or computational power to support high-end sensors or intensive cognitive processing for computer vision [Troiani *et al*, 2015]. These sensors are also susceptible to environmental conditions such as featureless surface textures or smoke filled environments.

An alternative solution is to reduce or remove the dependance on sensors entirely and instead avoid obstacles by building avoidance behaviour into the physical construction so that it occurs passively. Aircraft have long used passive control techniques to achieve stable flight — for

example, the use of dihedral on an aeroplane wing [Cook, 2012]. Dihedral wings are angled up on either side of the centerline such that as the aircraft rolls to one side the wing on that side will be closer to horizontal and produce more lift, acting about a longer lever arm, to restore the aircraft to a level equilibrium. No electronics or computational processing is required to restore the aircraft to level flight after a disturbance. The dynamic response of the aerodynamic–mechanical interactions regulate the systems behaviour and ensure its stability.

This concept of using passive control techniques can be extended to include interactions between a hovering robot aircraft and its surroundings. Passive obstacle avoidance behaviour may be achieved by understanding how a quadrotor interacts with surfaces and obstacles, and then leveraging these interactions to construct repulsive control laws to safeguard the rotors. An idea which is yet to be explored.

Flight near walls and obstacles is complicated by several interacting aerodynamic phenomena:

- Ground effect
- Wall effect
- Eggbeater effect

Ground effect is an aerodynamic phenomenon which occurs when a rotor is operating such that its downwash interacts with the ground [Prouty, 1995]. In this condition, airflow through a rotor is constrained by the ground below which causes it to slow and stagnate beneath the rotor, acting as a cushion resisting the rotors descent.

Wall effect occurs when a rotor is in close proximity to a wall the wall reduces the recirculation distance at the tip of the rotor closest to the wall which leads to an increase in thrust on this side of the rotor acting to tilt the rotor up away from the wall [Lee *et al*, 2015].

When a pair of contra-rotating rotors is moved so that both rotors are close to the wall 'eggbeater effect' acts to either repel or attract the rotors from the wall depending on the rotation direction of the rotors. It behaves in the same manner as an eggbeater mixing cake batter where the airflow enters laterally on one side of the rotors and is ejected on the other.

How these effects interact with each other and flight stability of a quadrotor is unexplored. By understanding and exploiting these effects, the robustness, performance and safety of micro quadrotor control may be improved. The eventual goal of this work is to enable a hovering

robot to robustly travel through a corridor, passageway or duct without any additional direct environmental sensing.

In comparison to dihedral, the relative forces acting on a rotorcraft due aerodynamic interactions with obstacles are small. Measuring these forces requires sensors of sufficiently small size and sensitivity that did not previously exist. Thus, exploring the space of passive rotor interactions necessitates developing sensors suitable to this task.

1.1 Problem Statement

In this project I seek to understand and exploit the aerodynamic effects acting on a small scale quadrotor to regulate relative position, attitude and velocity without extrinsic sensors.

I pose four key questions:

- How can we understand the aerodynamics of rotor-surface interactions?
- Can aerodynamic surface interactions be exploited for passive trajectory control of a hovering quadrotor vehicle?
- How can we measure the aerodynamic forces acting on a rotor during flight?
- Can we use aerodynamic force measurement to infer vehicle velocity?

To answer these questions I develop a specialised indoor quadrotor platform for investigating aerodynamic effects. By flying the quadrotor close to surfaces and through various trajectories, behavioural theories may be formed and verified.

1.2 Approach

My approach combines experimental investigation into aerodynamic phenomena with developing theories to support these observations, and testing applied technical solutions to the problem. This can be broken down into six key steps:

1. Develop a quadrotor platform for investigating aerodynamic effects, and implement a controller to accurately position the quadrotor for experiments.
2. Investigate the aerodynamic effects of surface proximity on quadrotor flight.

3. Develop a method for passive positioning of a quadrotor using the aerodynamic effects explored in step 2.
4. Develop a system to measure the forces acting on a rotor during flight.
5. Investigate the relationship between quadrotor velocity and rotor forces.
6. Synthesize results into a demonstration system.

Investigation of aerodynamic surface interactions requires the development of a quadrotor system capable of highly repeatable flight. This allows subtle aerodynamic effects to be observed and their influence measured and predicted over a number of experiments. One of the most significant sources of variation between experiments is decreasing battery voltage as the battery discharges. This is also a problem of broader interest in the field due to its importance in enabling precision flight maneuvers. We overcome this limitation through the use of a novel voltage regulator connected in series with the battery and aircraft to provide constant voltage to the drive system for the duration of experiments. The regulator, along with other elements of the quadrotor hardware, is described in Chapter 3.

Using the regulated quadrotor platform to conduct experiments, we are able to examine the influence of ground effect on quadrotors in flight. We expect that by flying quadrotors with a fixed thrust set just below the thrust required to hover in free air, it is possible to achieve passive height regulation. Ground effect offers a proportional restoring force around equilibrium and rotor inflow damping acts to damp the system. By tilting the ground surface and canting the rotors this effect can be brought into the horizontal direction — we anticipate that it is possible to achieve both lateral and vertical position keeping through these methods. Passive stability and position keeping of a quadrotor is explored in Chapter 4.

To further our understanding of the aerodynamic forces acting on a quadrotor during flight we propose the direct measurement of each rotor thrust vector by using miniature force-torque sensors. The size, cost and precision of existing commercially available force-torque sensors did not allow them to be easily integrated onto a small scale quadrotor. To overcome this we seek to develop a force-torque sensor suitable for measuring rotor forces in flight. Such a sensor must be very sensitive, accurate, light weight and low-cost. The construction and performance of this sensor is detailed in Chapter 5.

Of the aerodynamic forces acing on the rotors, blade flapping is of particular interest as it is closely linked to rotor transverse velocity. As a rotor translates horizontally, the blade tilts

backwards directing the thrust vector away from the direction of motion. We expect that with accurate measurement of the thrust vector, the flapping angle and thus horizontal velocity of the rotor can the inferred. Combining the sensor measurements from all motors the entire vehicle translational velocity can be estimated. Velocity estimation through blade flapping is discussed in Chapter 5.

1.3 Roadmap

This thesis is comprised of five chapters followed by a conclusion. Chapter 2 presents a literature survey of quadrotor aerodynamics and associated methods for measuring aerodynamic effects. Chapter 3 details the quadrotor platform hardware and software, and flying arena setup used throughout this thesis for flight experiments. Chapter 4 explores quadrotor aerodynamic surface effects including ground effect and wall effect, utilising them to achieve passive position regulation. Chapter 5 describes the development and application of a micro rotor force sensor, including its ability to measure vehicle velocity. The conclusion, Chapter 6, summarises the key outcomes of this thesis. Appendix A contains enlarged versions of the passive position response plots from Chapter 4. Appendix B contains additional velocity measurement plots using the force sensor from Chapter 5. Appendix C contains response plots using the force sensor for velocity feedback control also from Chapter 5.

Chapter 2

Literature Review

2.1 Unmanned Aerial Vehicles

An Unmanned Aerial Vehicle (UAV) or Unmanned Aerial System (UAS) is an aircraft which flies without a human pilot onboard. UAVs can be divided into two main groups: fixed wing and vertical take-off and landing (VTOL). Fixed wing aircraft, such as aeroplanes, typically require a much larger area to take-off and are unable to achieve stationary hover in flight, making them less suited to urban and indoor environments. Conversely, VTOL aircraft can operate in much more compact confines, and are thus much better suited to cluttered operating spaces — they can take-off from an area not much larger than the aircraft itself and hover at a fixed position once in flight. This capability comes at the cost of significantly reduced payload and loiter time, limiting the sensors and processing resources available. Quadrotors are a typical modern VTOL aircraft used in research and are gaining substantial popularity in industrial and commercial applications.

2.1.1 Quadrotor UAV

Modern research into the field of quadrotor helicopters took off in the early 2000s following the release of the Dragan Flyer in 1999 [Draganfly Innovations, 2016]. Pounds *et al* sought to develop and model a large more capable quadrotor, the X-4 flyer [Pounds *et al*, 2002, Pounds *et al*, 2004, Pounds *et al*, 2006]. Bouabdallah *et al* investigated different controller designs for attitude stabilisation [Bouabdallah *et al*, 2004, Bouabdallah and Siegwart, 2005]. Hoffmann *et al* explored outdoor flight and position control [Hoffmann *et al*, 2007].

Since the early theoretical work, the field has seen an explosion in many different directions. Parrot and DJI have developed successful low-end drones targeted at consumers [Parrot Inc., 2016, DJI Technology, 2017]. DIY Drones, 3D Robotics and ArduPilot have been core to drone

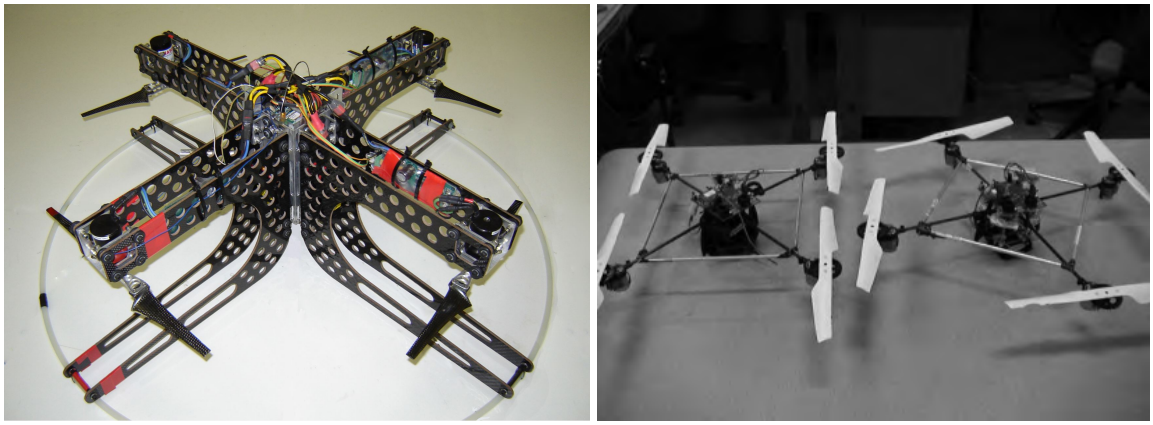

Figure 2.1: Early research quadrotors. Left: X-4 flyer [Pounds, 2007]. Right: STARMAC [Hoffmann *et al*, 2004]

enthusiast and research community development, providing flight control systems for affordable and capable UAVs [DIY Drones Community, 2017, 3D Robotics Inc., 2017, ArduPilot Dev Team, 2016]. The success of these companies is built on the development of low cost Micro-Electro-Mechanical Systems (MEMS) devices for gyroscopes and accelerometers along with efficient attitude estimation algorithms capable of running on low cost and low powered devices [Mahony *et al*, 2005].

In the research domain, quadrotors as a platform are used in the development and experimental testing of advanced control systems [Hehn and D'Andrea, 2011], swarm behaviour [Michael *et al*, 2010], aerial manipulation [Orsag *et al*, 2013], aircraft–object interaction [Müller *et al*, 2011], cargo delivery [Mellinger *et al*, 2013], environmental exploration [Achtelik *et al*, 2009] and other advanced robotic technologies. This has lead to an array of impressive demonstrations including quadrotors that can map and navigate a building [Blösch *et al*, 2010] through to quadrotors that can perform choreographed musical performances [Schöllig *et al*, 2010] and acrobatics displays [Mellinger *et al*, 2012]. While substantial progress has been made, this work faces significant challenges in extending to outdoor environments, due to the requirement for the precision tracking systems that underly much of the capabilities seen in contemporary aerial robotics research.

2.1.2 Commercial Quadrotors and Multirotors

Commercial quadrotor platform have been available since the launch of the Draganflyer in 1999 [Draganfly Innovations, 2016]. The Draganflyer was a radio control (RC) model targeted at

Figure 2.2: Left: the original Draganflyer, one of the first commercial quadrotors [Draganfly Innovations, 2016]. Right: the DJI Phantom 3, currently one of the most ubiquitous quadrotors [DJI Technology, 2017].

hobbyists that provided the pilot with gyroscope-derived angular velocity damping. It was used in some of the early research on quadrotor modelling and control [Altuğ *et al*, 2002]. Since then Draganfly and other companies have continued development of multirotors targeted at consumers and industry.

Ascending Technologies offers two quadrotors the Hummingbird and Pelican which represented the first commercially available 'smart' quadrotor [Ascending Technologies, 2017]. It was a complete package with features including drift compensation, position control and high performance hardware capable of fast response. Both of these quadrotors were used extensively in the research domain because they lowered the barrier to entry by providing complete flying platform which could easily be extended. The Hummingbird was utilised for its high power to weight ratio and ability to achieve aggressive and agile flight [Mellinger *et al*, 2012]. The Pelican offered a large, 650 g payload and onboard computer allowing for the use of additional sensors and advanced autonomous capabilities [Weiss *et al*, 2011].

Mikrokopter offered an alternative solution which was a more basic and cheaper flying platform designed so that it could easily be adapted [MikroKopter, 2017]. Its aluminium construction and the ability to use different power systems allowed it to be adapted to different applications and payloads [Hou and Mahony, 2013].

3d Robotics produced two key quadrotor platforms the IRIS and Solo [3D Robotics Inc., 2017]. These grew out of the research and open source UAV communities. The IRIS was geared towards researchers and hobbyists offering a robust flight platform to which cameras, sensors and other accessories can be mounted. The Solo attempted to take this at step further

creating a more integrated platform targeting consumers.

The most ubiquitous consumer drone brand is DJI. They released their first fully integrated ready-to-fly Phantom quadrotor in January 2013 and now offer four models the Phantom, Mavic, Inspire and Mattrice [DJI Technology, 2017]. The Phantom and Mavic are marketed at consumers offering stabilised video capabilities, waypoint following and target tracking. The Inspire is a larger professional equivalent offering a camera with a large sensor and interchangeable lens targeted at videographers. The Mattrice is targeted at researchers and industrial users offering a flying platform with sensors for obstacle avoidance, onboard computational resources and an SDK allowing it to be tailored to a specific payload and application.

Another major company in the consumer drone market is Parrot which offers the ArDrone and Bebop [Parrot Inc., 2016]. These drones were the first consumer drones to feature computer vision, initially in the form of downward facing optical flow systems for position keeping and later including target tracking and digital image stabilisation.

Yuneec offers Typhoon and Breeze drones which compete almost directly with DJI drones as aerial video platforms [Yuneec, 2017]. GoPro, known for their action cameras, have released the Karma drone designed to work with their Hero cameras [GoPro Inc., 2017]. It has a unique feature in that the gimbal can be removed and used to achieve hand-held stabilised video.

Microdrones offers large industrial quadrotors capable of carrying payloads of several kilograms with flight times of 45 minutes [Microdrones, 2017]. These platforms are generally used with high resolution scanning and image sensors for mapping, inspection and surveying applications.

There are now a wide array of commercial multirotors available. Ranging from the Cheerson CX-10 palm sized drone [Cheerson, 2017], all the way up to the Olaeris AEVA, a conventional helicopter alternative geared to the aviation market [Olaeris Inc., 2017]. There are even companies developing multirotors as personal aerial vehicles [Ehang Inc., 2017, Volocopter GmbH, 2017]. The availability multirotors over such varied markets demonstrates the prominence of the platform and suggests that any improvements to their aerodynamic performance and capabilities could have wide reaching impact.

2.2 Quadrotor Aerodynamics

2.2.1 Rotor Performance

Quadrotor propulsion and lift are provided by the rotors, which convert rotation of the motors into thrust by accelerating a column of air.

Using the Blade Element Method (BEM) the thrust, torque and power of a rotor can be modelled [Prouty, 1995, p15]. For an ideal rotor of uniform airfoil profile thrust is given by:

$$T = C_T \rho A \Omega^2 R^2 \tag{2.1}$$

where ρ is the density of air, A is the rotor disc area, Ω is the rotor angular velocity, R is the rotor radius and C_T is the rotor thrust coefficient, a geometric property of the rotor, given by:

$$C_T = \frac{C_l \sigma}{6} \tag{2.2}$$

where C_l is the rotor lift coefficient, σ is the rotor solidity ratio.

Ideal rotor torque is given by:

$$Q = C_Q \rho A \Omega^2 R^3 \tag{2.3}$$

where C_Q is the rotor torque coefficient given by:

$$C_Q = C_T \sqrt{\frac{C_T}{2}} + \frac{C_d \sigma}{8} \tag{2.4}$$

where C_d is the rotor drag coefficient.

Correspondingly, ideal rotor power is given by:

$$P = C_P \rho A \Omega^3 R^3 \tag{2.5}$$

where C_P is a power coefficient, such that:

$$C_P = C_Q \tag{2.6}$$

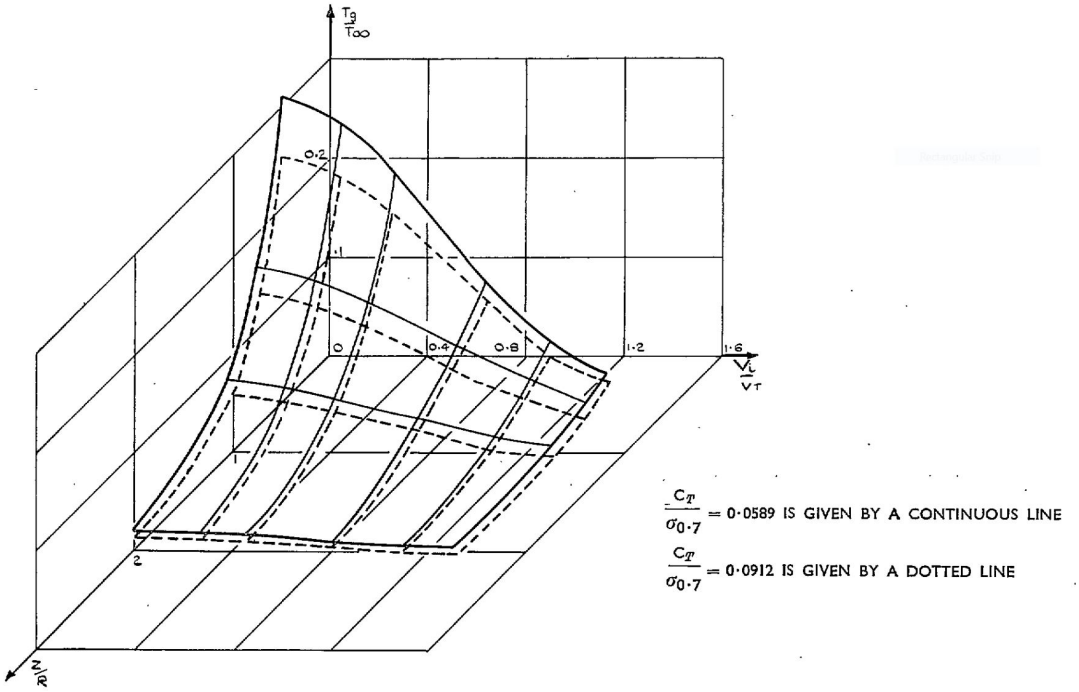

Figure 2.3: Variation of thrust ($\frac{T_g}{T_\infty}$) with height ($\frac{Z}{R}$), speed ($\frac{V_i}{V_T}$) and blade loading ($\frac{C_T}{\sigma 0.7}$) [Cheeseman and Bennett, 1955].

The rotor thrust (2.1) shows that for a given blade profile thrust can be increased by increasing the radius, angular velocity or solidity ratio of the rotor. Rotor solidity ratio can be increased by adding additional blades to the rotor. However, there will be trade offs as changing these parameters also impacts rotor torque and power.

Due to the scaling of rotor torque and power with rotor radius and angular velocity, the same increase in thrust can be achieved with 30 per cent less power by increasing rotor radius rather than increasing rotor angular velocity. Therefore for maximum efficiency it is preferable to use large slow spinning rotors over small fast rotors.

2.2.2 Ground Effect

In free air, rotor wake disperses beneath the quadrotor and attenuates some distance downstream [Prouty, 1995]. However, when close to the ground (within approximately two rotor radii distance), the wake of the rotors is contained by the surface underneath them, creating a cushion of air referred to as 'ground effect' [Leishman, 2002]. This cushioning increases the lift generated by the rotors and behaves as a repulsive force resisting the quadrotor's descent [Pounds and Dollar, 2010].

Cheeseman and Bennett developed an analytical model for a rotor in ground effect by using the method of images [Cheeseman and Bennett, 1955]. This involves a copy of the rotor reflected about the ground plane and modelling the interaction between the source and image rotors. Their model first showed the quadratic relationship between hover thrust and height above ground, in ground effect as illustrated in figure 2.3. The relationship is given by:

$$T_{GE} = \frac{1}{1 - (\frac{BR}{4z})^2} T_{FA} \tag{2.7}$$

where T_{GE} is the thrust generated in proximity to the ground, T_{FA} is the thrust generated in free air, r is the rotor radius and z is rotor height above ground, and B is a rotor radius scaling parameter — typically taken as $B = 1$ for helicopters.

In the 1970's, Heyson conducted extensive analysis on the induced velocities for helicopters and VTOL aircraft [Heyson, 1973]. This work paid particular attention to the changes in airflow when the aircraft were operating in ground effect, between 0.3 and 2 rotor radii from the ground. It showed that ground effect produces a quadratic decrease in power required to hover, with 20 per cent less power required when the rotor was one rotor radii from the ground [Heyson, 1977].

Powers *et al* conducted experiments with a micro quadrotor flying close to the ceiling and ground [Powers *et al*, 2013]. They obtained experimental data showing the decrease in hover thrust experienced as the quadrotor moved closer to either the ceiling or ground.

Sharf *et al* explored further and modelled ground effect for quadrotors using the analytical models developed for helicopters [Sharf *et al*, 2014]. Helicopter models show ground effect is significant up to 2 rotor radii from the ground. However, they found experimentally that the ground effect zone extended out to 5 rotor radii. They theorised that this was due to the proximity of the four rotors not allowing the ground effect airflow to taper out at the center of the quadrotor, instead bunching up where it meets flow from the other rotors. This shows that ground effect could have a greater effect on quadrotors than previously assumed using the 2 rotor radii rule.

Schmaus *et al* have attempted to exploit ground effect for performance gains in a human powered pedal-driven helicopter [Schmaus *et al*, 2012]. The Gamera, Gamera II [Berry *et al*, 2012] and Atlas [Robertson and Reichert, 2014] quadrotor vehicles made use of ground effect in their attempts towards the Sikorsky prize for human powered helicopter flight. In a similar vein,

the wing-in-ground effect vehicle developed at Tohoku University made use of ground effect in a channel [Sugahara *et al*, 2011]. This vehicle flew 4 to 5 cm above the ground, and was shown to be controllable in both simulation and experiments. However, it did not have passive position stability and requires active control to maintain separation from the walls [Sugahara *et al*, 2012].

2.2.3 Wall Effect

The effect of wall proximity on quadrotors is well known in the research community but as yet under referenced in the literature. During his study of ground effect Heyson also examined the interactions of VTOL aircraft operating in proximity to walls and enclosed spaces [Heyson, 1974]. He showed that in some cases much of the lift generated by fans is due to wall interference and experiments conducted in proximity to walls can follow opposite trends to flight in free air. Due to the complex nature of these interactions current strategies on quadrotors are to avoid walls by detecting them with sensors.

2.2.4 Rotor Inflow Damping

As a rotor moves upwards through a vertical air column, the inflow has an added vertical velocity component as it meets the rotor blade which, in combination with the motion of the rotor, leads to a reduced effective angle of attack, as shown in figure 2.4. This results in a reduction in the thrust produced by the rotor, acting in opposition to the upward motion of the rotor. Similarly as the rotor moves downwards the vertical velocity component of the air meeting the blade leads to an increased effective angle of attack, and consequent increase in thrust produced. Again, this increase in thrust acts to resist the downward motion of the rotor [Prouty, 1995]. Together, these have a net effect of damping the vertical movement of the rotor.

This may be modelled as a change in force relative to hover thrust. The variable thrust coefficient is given by:

$$C_T = \frac{\sigma a}{4}\left[\theta_{tip} - \frac{(v_i + \dot{z})}{\Omega R}\right] \tag{2.8}$$

where σ is the rotor solidity ratio, a is the blade lift slope, θ_{tip} is geometric angle of attack at the blade tip, v_i is air inflow velocity, $\dot{z}$ is vertical velocity of the rotor, Ω is the rotor angular

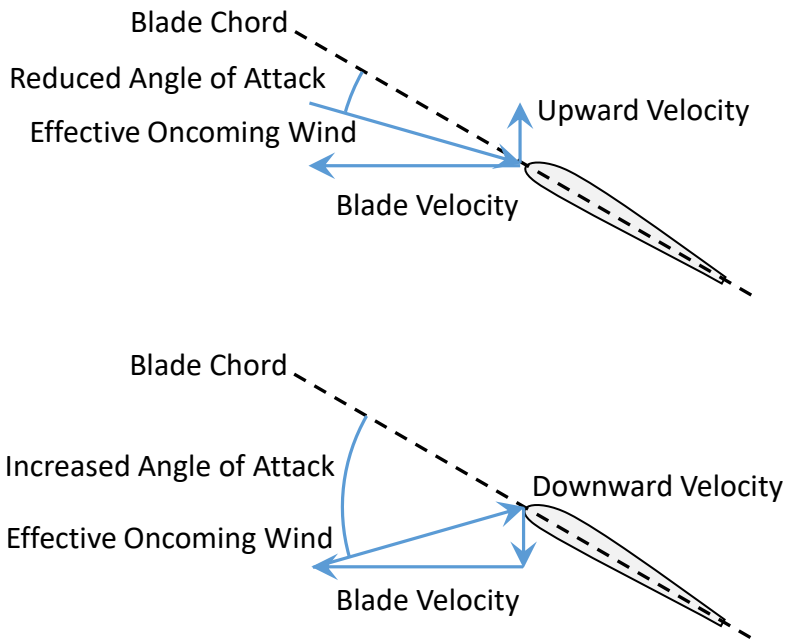

Figure 2.4: Rotor inflow damping.

velocity and R is the rotor radius.

On a quadrotor roll and pitch motions leads to opposite rotors moving up and down relative to one another as a consequence they experience rotor inflow damping [Pounds *et al*, 2006]. This leads to roll and pitch attitude velocity damping.

2.2.5 Rotor Blade Flapping and Induced Drag

When translating laterally, a rotor experiences localised changes in angle of attack as it rotates [Pounds *et al*, 2004, Mahony *et al*, 2012]. As the rotor blade sweeps towards the direction of translation the effective oncoming wind leads to an increased angle of attack on the blade and a subsequent increase in thrust. Conversely as the retreating rotor blade experiences a decreased angle of attack and thrust as it moves with the effective oncoming wind. The cyclic nature of this thrust imbalance on opposing blades causes the rotor plane to tilt away from the direction of translation. As a result of this tilting, a component of the trust is directed into the horizontal plane acting in opposition to the lateral translation of the rotor. This force acts to damp the lateral motion of the rotor.

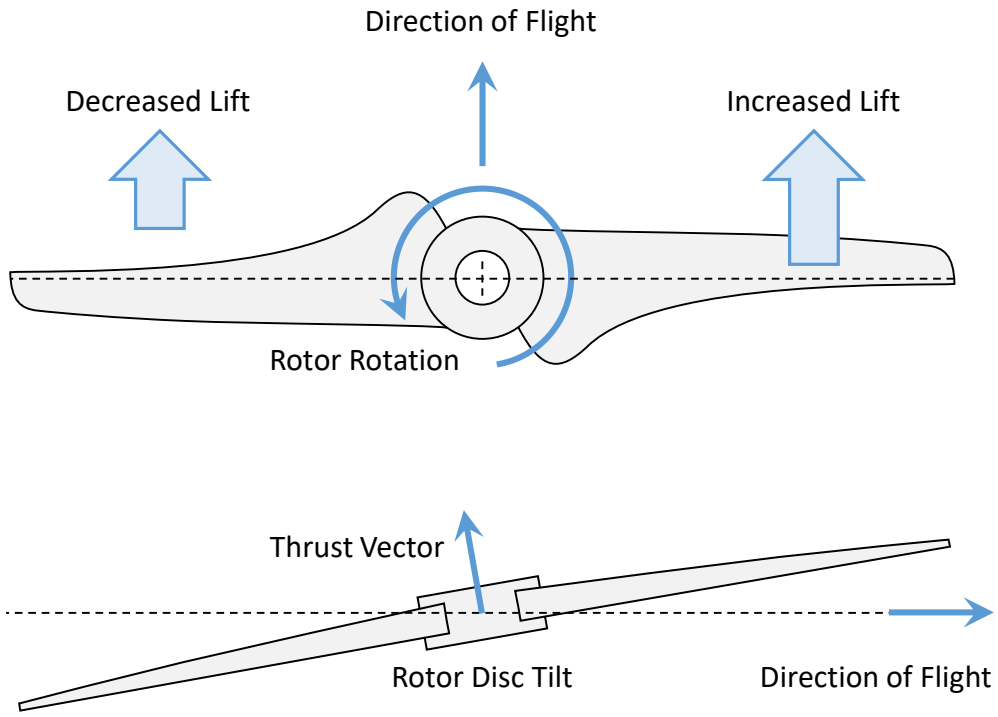

Figure 2.5: Blade flapping.

The rotor blade flapping angle can be approximated as a linear function of lateral velocity, $\dot{x}$, and pitch velocity, $\dot{\theta}$: [Pounds *et al*, 2010]

$$a_1 = q_1\dot{x} - q_2\dot{\theta} \tag{2.9}$$

where q_1 and q_2 are the translation and pitch velocity coefficients given by:

$$q_1 = \frac{4\theta_{tip} - 2v_i}{\omega R} \tag{2.10}$$

$$q_2 = \frac{16}{\gamma\omega} \tag{2.11}$$

where θ_{tip} is the geometric angle of attack at the blade tip, v_i is the inflow velocity, ω is the rotor rotational velocity, R is the rotor radius and γ is the Lock Number, a ratio of aerodynamic to inertial rotor forces.

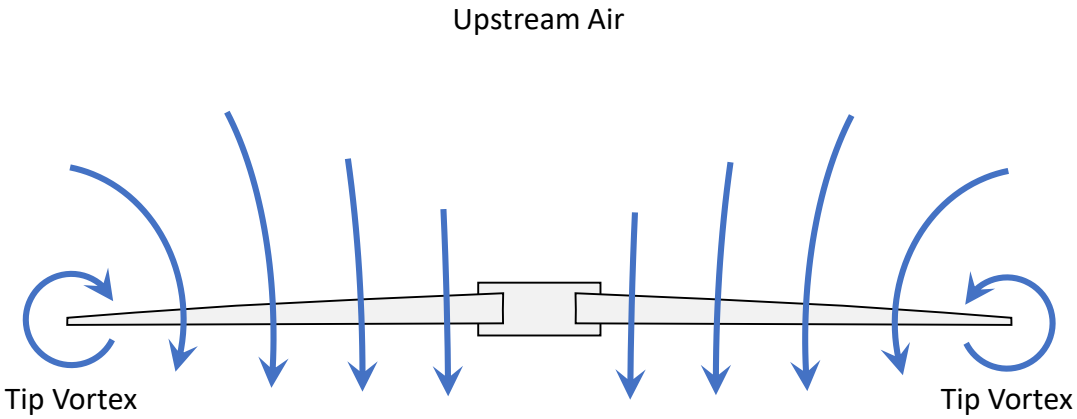

Figure 2.6: Tip vortices.

2.2.6 Tip Vortices

At the tip of a rotor blade, part of the airflow exits the rotor and circulates upwards and re-enters the rotor, as shown in figure 2.6. This circulation of air is referred to as rotor blade tip vortices [Prouty, 1995, p55]. As a consequence of this behaviour, the recirculated air entering the tip of the blade already has some velocity. This reduces the rotors ability to accelerate the air and as a consequence less lift is produced. Disrupting these tip vortices is one of the reasons that ducted rotors can be more efficient.

2.3 Quadrotor Dynamics and Control

A quadrotor uses four rotors to achieve flight. Vertical control is achieved by increasing or decreasing all four motors collectively. Pitch control is achieved by a difference in speed of the front and rear pairs of motors, similarly roll is controlled by a speed difference in left and right pairs. Yaw is more subtle: each pair of diagonal rotors spins in the opposite direction — by commanding a difference in speed between diagonal pairs a net moment imbalance results causing the quadrotor to yaw. As the quadrotor only has four actuators it is an under-actuated system, meaning that position and orientation are coupled.

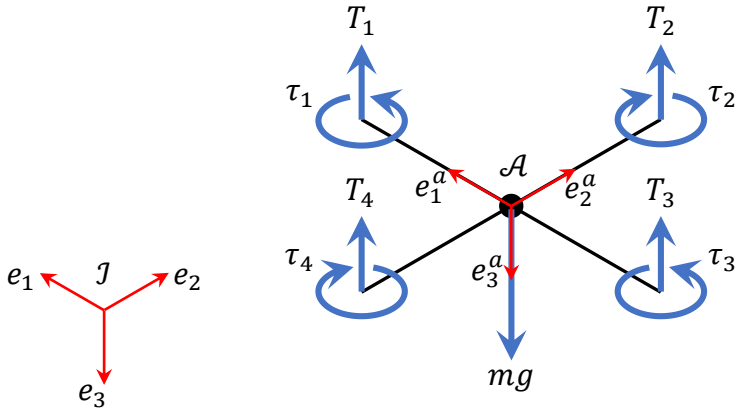

Figure 2.7: Quadrotor free body diagram.

2.3.1 Quadrotor Dynamic Models

The basic rigid body dynamics of the quadrotor can be derived by treating the quadrotor as a mass with four thrust-torque generators, as shown in figure 2.7 [Pounds *et al*, 2006, Mahony *et al*, 2012].

$$\dot{\xi} = \mathbf{v} \tag{2.12}$$

$$m\dot{\mathbf{v}} = mg\mathbf{e_3} + RF \tag{2.13}$$

$$\dot{R} = R\Omega_\times \tag{2.14}$$

$$I\dot{\Omega} = -\Omega \times I\Omega + \tau \tag{2.15}$$

where ξ is the position, R is the rotation matrix from body fixed to static reference frames, $\mathbf{v}$ is the vehicle linear velocity, m is the vehicle mass, g is the acceleration due to gravity, $\mathbf{e_3}$ is the z direction in the fixed frame, F is the thrust force affected by the motors, I is the vehicle rotational inertia, Ω is the vehicle rotational velocity, $_\times$ is the skew symmetric matrix operator such that $a_\times b = a \times b$, and τ is the moment affected by the motors.

The thrust force produced is given by the combination of all four motors:

$$F = \sum_{i}^{N} T_i \tag{2.16}$$

2.3.2 Quadrotor Control

Quadrotor control is principally directed to the regulation of aircraft attitude and position by varying motor speeds based on sensor inputs. Attitude control is the most important as it directly affects the quadrotors ability to remain airborne. At its most basic, the rotational dynamics of the system is a double-integrator, where differential motor speed corresponds to angular acceleration. Thus orientation control requires damping, as proportional feedback alone would lead to constant oscillation [Franklin *et al*, 2009]. In practice an integral term is also required to correct steady-state errors due to center of mass offsets and individual rotor and motor performance variations. Thus PID regulation is an industry norm for such aircraft.

Other control strategies have been explored. Bouabdallah *et al* investigated the performance of LQ (Linear Quadratic) optimal control vs PID (Proportional-Integral-Derivative) applied to a micro quadrotor [Bouabdallah *et al*, 2004]. While they showed that theoretically LQ should achieve a marginal performance increase in practice this was not found to be the case. It is likely that due to insufficiencies in the model the LQ approach was unable to achieve free flight.

Bouabdallah and Siegwart also implemented backstepping and sliding-mode controllers for quadrotor attitude stabilisation [Bouabdallah and Siegwart, 2005]. Both of these non-linear controllers were able to achieve stability in simulation and on a suspended test-bed, with backstepping offering a 50 per cent decrease in settling time. The sliding-mode controller exhibited high frequency oscillations due to its switching nature.

All of the control strategies described thus far employed 3 separate controllers running on the pitch, roll and yaw angles. Tayebi and McGilvray implemented one of the first quaternion controllers for quadrotors, which unlike Euler angles do not suffer from gimbal lock [Tayebi and McGilvray, 2006]. By accounting for coriolis and gyroscopic torques along with a PD^2 structure, the controller was shown to be exponentially stable.

Altuğ *et al* used visual feedback from a ground mounted camera to control the pose of a quadrotor along with feedback linearisation and backstepping controllers [Altuğ *et al*, 2002]. They were able to demonstrate stable flight on an experimental platform using a commercial RC quadrotor. This was also one of the first examples of quadrotor position control.

Hoffmann *et al* implemented the first position and attitude control on an outdoor quadrotor operating in hover and at moderate translational velocities [Hoffmann *et al*, 2007]. They showed that blade flapping and induced drag substantially impacted the quadrotors ability to accurately

regulate attitude as lateral velocity increased. At low speeds of 0.5 to 2.0 ms^{-1} they achieved pre-generated trajectory tracking using a PI controller, from position to commanded attitude, along the desired trajectory and PID orthogonal to the trajectory. Tracking was achieved within 0.1 m of the desired path.

Huang *et al* implemented some of the first control algorithms to compensate for aerodynamic effects present during aggressive maneuvers at higher speeds , 6 to 8 ms^{-1} [Huang *et al*, 2009]. At higher speeds the translational lift and angle of attack of the rotor result in significant additional thrust. By modelling these effects and using feedback linearisation they were able to compensate for these effects during aggressive maneuvers leading to better attitude and altitude trajectory tracking.

Bouffard *et al* used learning based model predictive control (LBMPC) to improve trajectory tracking of a quadrotor [Bouffard *et al*, 2012]. They showed that when compared to the step response of a linear MPC the LBMPC exhibits considerably less overshoot, over 50 per cent less. LBMPC was also able to account for deficiencies in the linear model when operating in ground effect and reduce the motor commands to reach goal positions close to the ground.

Ultimately, despite the early and on-going interest in alternate control strategies, PID remains the prevailing stabilisation and control method for research and commercial multirotor flight control. It is simple to implement and does not require detailed system models of the aircraft.

2.3.3 Passive Stability

Passive stability can be an effective way of achieving robust systems and reducing reliance on active control, which can require additional sensing and computational resources. The use of dihedral on an aeroplane wing is an archetypical example of a passive system used to maintain stable flight [Cook, 2012]. Aerodynamic-mechanical interactions regulate the system and bring it back to equilibrium in the absence of pilot input.

Purely passive systems are necessarily stable and will always act to either maintain or reduce the total energy in the system over time. Consider a system with input $u(t)$, output $y(t)$ and energy $V(t)$, then the system is passive if [Lozano *et al*, 2007, p13]:

$$\dot{V}(t) \leq y^T(t)u(t) - d(t) \tag{2.17}$$

and

$$\int_0^t d(s)ds \geq 0, \forall t \geq 0. \tag{2.18}$$

where $y^T(t)u(t)$ is the energy supplied and $d(t)$ is the energy dissipated by the system.

Typically quadrotors utilise an Inertial Measurement Unit (IMU) and feedback control to achieve stable attitude regulation. However, Piccoli and Yim were able to design a modified quadrotor capable of passive attitude stability with no active sensing [Piccoli and Yim, 2015]. Their design resembles a box kite constructed around the quadrotor with four stabilising surfaces above and below the rotor plane. The effective oncoming wind due to lateral motion combined with the vertical wind produced by the rotors result in the angle of attack on the stabilisers. The resultant lift acts as a restoring force resiting the motion. Body drag on the stabilisers acts to damp the system.

Position regulation and obstacle avoidance is another area where quadrotors could benefit from a passive system approach. This would be especially useful in micro quadrotors where resources and payload capacity are limited. It could also allow quadrotors to operate in difficult environments, for example indoor, dark or smoke filled environments where conventional sensors such as GPS, cameras and lidar are ineffective.

2.4 Quadrotor Construction and Systems

A typical RC quadrotor is comprised of eight key components: rotors; motors; electronic speed controllers; a flight controller; a radio receiver; a battery; a frame; and a wiring harness.

2.4.1 Avionics / Flight Control

The flight controller is the heart of a quadrotor. This system includes the sensors and processing power to measure and estimate the quadrotor pose, run the main control loop for attitude feedback (and position feedback if available), receive set-points from a radio or onboard autonomy computer, and output commands to the motors. There are a wide array of flight controller hardware and software solutions available, ranging from basic attitude stabilisation through to advanced trajectory control with triple redundancy.

Mikrokopter offered some of the earliest commercial-off-the-shelf (COTS) flight controllers targeted specifically at quadrotors [MikroKopter, 2017]. The FlightCtrl V1.0 had a three separate gyroscopes and a three axis accelerometer connected to a Atmega644 MPU. It was designed to be used with their own BL-Ctrl motor controllers communicating over I2C and optionally the NavCtrl and GPS for waypoint following.

KKMulticopter flight controllers offered basic stabilisation capabilities with low cost hardware [Bakke, 2011]. Early versions included gyroscopes and were capable of attitude rate stabilisation only. The latest version includes an accelerometer for attitude stabilisation and an onboard display for programming the control loop gains in the field [HobbyKing, 2017].

Openpilot developed one of the first flight controllers based around a 32-bit MPU offering a substantial increase in processing power [OpenPilot Team, 2017]. This allowed the implementation of faster control loops and more advanced attitude estimators, such as an extended Kalman filter. The open source firmware was forked and developed further by the Tau Labs and Libre Pilot projects to offer more advanced capabilities including waypoint following [Tau Labs, 2015, LibrePilot, 2016].

MultiWiiCopter, BaseFlight, CleanFlight and BetaFlight are a series of open source flight controllers and software [MultiWiiCopter, 2017,Baseflight Team, 2017,Cleanflight Team, 2017, Betaflight Team, 2017]. The original MultiWiiCopter was designed to utilise the IMU for a Wii Nunchuck controller connected to an Arduino. It was primarily a software project. From there the software was extended by BaseFlight, and subsequently CleanFlight and BetaFlight, to run on 32-bit flight controllers such as the OpenPilot CopterControl or those made with STM32 development boards and 10-DoF IMU modules. More recently flight controllers have been designed and released specifically for the CleanFlight and BetaFlight firmware, which is used extensively in FPV racing.

The Px4 autopilot, and later Pixhawk, originated from the Pixhawk research project at ETH Zurich and was commercialised in collaboration with 3D Robotics [Pixhawk Team, 2017, 3D Robotics Inc., 2017]. It uses a 32-bit ARM cortex M4 processor running at 180 MHz, which is much more powerful than the 8-bit alternatives, and a secondary failsafe processor to handle motor and receiver signals. It features multiple IMUs for redundancy and improved pose estimation performance. The open source Px4 firmware was developed alongside the hardware and offers a number of modules to extend its capabilities with different sensors and algorithms [PX4

Dev Team, 2017].

ArduPilot Mega grew out of the ArduPilot project which was interested in the development of low cost open source hardware and software for fixed wing UAVs [ArduPilot Dev Team, 2016]. The early versions used thermopiles to detect the horizon and determine aircraft attitude. When the project shifted to the use of MEMS sensors for the IMU interest in using the platform for quadrotor and multirotor control began. Since then the project has continued to grow and is now one of the most powerful open source autopilot software projects capable of running on a wide array of hardware platforms including Pixhawk.

DJI makes the NAZA and A3 autopilots [DJI Technology, 2017]. The NAZA is a simple stabilisation platform with possible GPS waypoint following and is designed to be easilty configured for different quadrotor platforms. The A3 is a high performance flight controller designed for use in applications where high reliability is required. This is achieved through triple sensor redundancy.

2.4.2 Quadrotor Power Systems

It is desirable to have consistent rotor performance for ease and precision of regulating flight trajectory. However, quadrotors are predominantly powered by lithium polymer cells which, while providing excellent energy density and discharge rates, suffer from non-constant output voltages [Tuta Navajas and Roa Prada, 2014]. They range from 4.2 V when fully charged, down to $<$3 V when depleted, following a non-linear discharge curve, as shown in figure 2.8. As a consequence, the voltage to the motor controller reduces over time and the same throttle command will lead to decreased rotor output power. Furthermore, diminishing battery voltage will reduce the available current draw to affect motor torque for dynamic rotor response. Podhradsky *et al* found that sagging battery voltage increased motor command response latency and gave rise to a noticeable reduction in the agility of the craft [Podhradsky *et al*, 2013].

Compensators designed to overcome this problem employ either endogenous techniques such as battery voltage models, or exogenous controllers based on sensor feedback. Podhradsky *et al* use a characteristic discharge curve to apply an open-loop compensation term to thrust control loop [Podhradsky *et al*, 2013]. However, this approach cannot adjust for small inconsistencies in the discharge curves between different models of battery. Efe developed an active control solution which measures instantaneous battery voltage to maintain constant thrust [Efe,

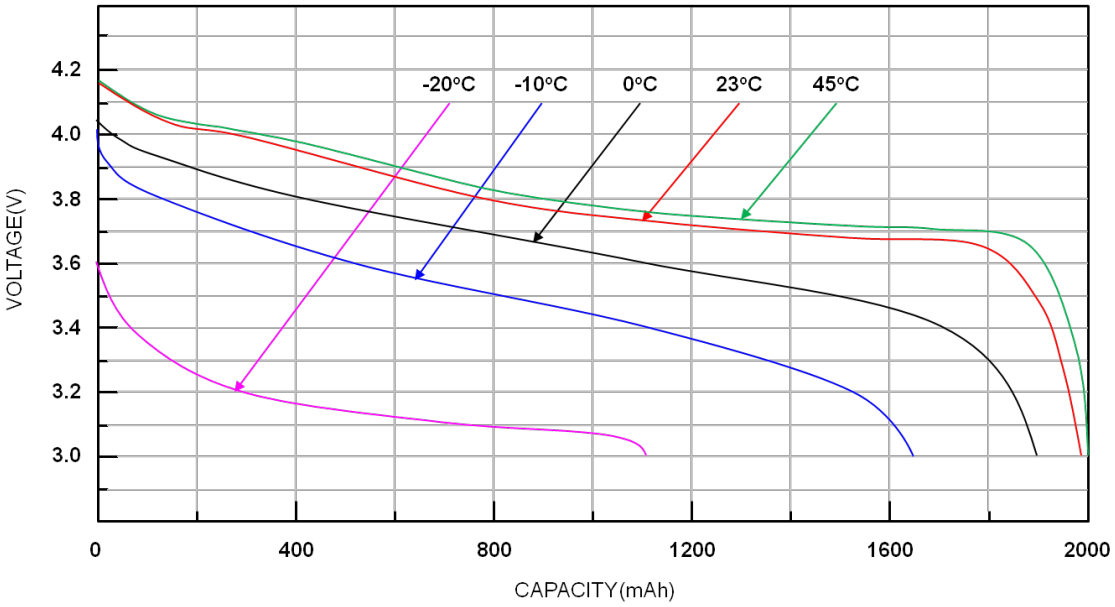

Figure 2.8: Lithium polymer battery discharge curve [Richtek Technology Corporation, 2014].

2012]. The findings demonstrated that accounting for differential battery voltage within the control loop had desirable performance effects.

Bangura *et al* regulate aerodynamic power via onboard measurements of rotor speed and current for each motor [Bangura *et al*, 2014]. These were used to estimate usage of electrical power and thus the total contribution to aerodynamic power, resistive loss within the motor and mechanical power being produced by the motor. Their testing focused on validating the effectiveness of the aerodynamic controller at rejecting wind disturbances in axial and planar direction. The controller was able to resist induced changes in translational lift due to imposed horizontal and axial airflow disturbances at altitudes well outside of the ground effect. The controller was able to achieve a finer degree of thrust manipulation than state-of-the-art motor control based on regulating rotor RPM.

2.4.3 Drive System

The drive system of the quadrotor is responsible for providing the actuation forces that allow the quadrotor to fly and maneuver. The three principal components are the rotors, the motors and the electronic speed controllers.

The key considerations when choosing the rotors are driven by application and required performance. Recently the hobby quadrotor community has seen substantial growth in racing,

which requires high speed forward flight and agility [Gebhardt *et al*, 2016]. As a consequence, rotors designed for racing are often more similar to propellers for aeroplanes with an increased angle of attack to provide high thrust in forward flight. However, this comes at the expense of decreased efficiency and endurance.

Conversely, industry and research communities are often interested in improving rotor efficiency in order to achieve longer flight times [Ure *et al*, 2015]. The maximum efficiency of a helicopter rotor in practice is approximately 80 per cent [Prouty, 1995]. The highest efficiency quadrotor rotors developed to date were used on the ANU X4 flyer achieving 77 per cent [Pounds *et al*, 2009]. Another way in which vehicle efficiency can be improved is using large rotors, as they will be accelerating a larger volume of air by a smaller velocity leading to less viscous drag for the same thrust [Driessens and Pounds, 2015].

The motor used to drive the rotors is equally important for achieving an efficient drive train. While brushed motors are cheap and easy to control they are not very well suited to quadrotors as they require periodic maintenance, can have significant friction losses and do not meet the high torque requirements of quadrotors [Alciatore and Histand, 2012, chap. 10]. Quadrotors such as the original Draganflyer which utilise brushed motors include gear boxes in order to meet the torque demand [Draganfly Innovations, 2016].

Today most quadrotors utilise Brushless Direct Current (BLDC) motors which, while more expensive to construct, offer a number of advantages. They are more efficient and have a higher output power and torque in the same size. Plus the lack of brushes reduces friction, mechanical and electrical noise and thus reduces the need for maintenance [Alciatore and Histand, 2012, chap. 10]. The torque demands of efficient rotors indicate that high torque, low speed or high kV motors will be the best match for an efficient design. Pounds *et al* suggested that motors need to be large diameter flat design with a low kV, which at the time were not readily available [Pounds, 2007]. Today a number of pancake style BLDC motors offered by different manufacturers [T-motor, 2017, KDE Direct, 2017].

An Electronic Speed Controller (ESC) is used to control power deliver and commutation of the motor. Typical ESCs control the voltage amplitude going to the motor phases and monitor back Electro-Motive-Force (EMF) to determine motor speed [Iizuka *et al*, 1985]. Many also utilise regenerative braking which allows the motor to be decelerated more quickly than free-wheeling alone and recovers some of the power back into the battery. The hobby community

and FPV racing has lead to the rapid advance of ESC technology with efforts especially focused on the development of powerful open source firmware BlHeli and SimonK [Skaug, 2017, Kirby, 2017]. Most manufactures now offer ESCs which utilise BlHeli firmware. This firmware has the ability to accept motor commands at 2 KHz to 32 KHz reducing the system latency and significantly exceeding the natural frequency of the motor rotor system [Bangura *et al*, 2014].

2.4.4 Airframe

The airframe provides a rigid mechanical link between the components of the quadrotor. The batteries and electronics are typically centrally located with the motors and rotors mounted on the ends of four long arms. By centralising much of the mass, the rotational inertia of the aircraft is minimised to allow for better control response and more agile flight. There are several common approaches to airframe construction: aluminium arms; carbon fibre balsa wood core; plastic arms; plastic molded monocoque; carbon fibre tube arms; and single piece carbon sheet.

Aluminium arms bolted between two fibreglass central plates was the method of construction adopted by Mikrokopter [MikroKopter, 2017]. The aluminium arms were hollow square profile allowing the motors to be bolted directly to the arms and motor wires could be routed down the arms. The central core was a stack of control electronics boards and the battery attached with velcro straps.

Ascending Technologies used carbon fibre with a balsa wood core for the frame of their Pelican quadrotor [Ascending Technologies, 2017]. This method allowed for a light weight frame with exceptional rigidity. The arms were also attached to the central frame with fasteners to allow replacement of individual frame components should they become damaged. The ESCs were mounted along the arms which allows them to be cooled by airflow from the rotors. The centre was constructed from four uprights to which shelves of the same material could be attached at various heights to allow the attachment of different components and sensors.

The DJI Flame Wheel airframe was constructed from plastic arms and fibreglass centre plates [DJI Technology, 2017]. The arms were molded from a fibreglass reinforced nylon for additional strength and rigidity. The central body was two printed circuit boards one of which included power distribution capabilities for easy wiring of the power and signal to the motor controllers.

The DJI Phantom used a plastic monocoque construction [DJI Technology, 2017]. This

simplifies assembly and allows all of the electronics to be housed within the airframe enclosure. However, the obvious disadvantage is that any non-trivial damage would require replacement of the entire airframe.

Carbon fibre tubes are used in a variety of frames such as the Tarot X690 [Tarot RC Helicopters, 2017]. They are usually fixed to carbon fibre plates at the centre of the quadrotor with machined aluminium mounting brackets. Tubes do not readily support direct mounting of the motors so a plastic or aluminium mounting bracket is required.

Single piece carbon fibre airframes are often used on smaller quadrotors — especially those used to First Person View (FPV) flight, such as the Armattan MRP 130 [Armattan Quads, 2017]. They are usually designed to withstand repeated high speed crashes without any damage to the frame. As a result they are extremely rigid but also relatively heavy for their size.

2.5 Embedded Force Measurement

Force sensing is fundamental to measuring robotic interaction with the environment since all physical interaction occurs through the transmission of force, such as through a serial manipulator's end effector. This is no different for a quadrotor, which interacts through the force applied by its rotors on the air. Understanding this force interaction can allow improved precision and performance of both a robotic arm and quadrotor alike.

Several force measurement modalities have been explored in robotics. We consider load cells and MEMS force sensors for our application due to their simplicity, compact size, precision and light weight.

2.5.1 Load Cells / Force Torque Sensors

Load cells are used to convert mechanical force into an electrical signal proportional to the load applied. One type of load cell is based on the use of a strain gauge attached to a load bearing member, usually metal, as a load is applied the metal flex or deformation is measured by the strain gauge which changes resistance [Alciatore and Histand, 2012, p. 391]. This resistance change is usually measured through the use of a wheatstone bridge configuration in combination with a precision ADC. A load cell is only capable of measuring force along a single axis, however it is common to combine a number of load cells into a multi-axis sensor.

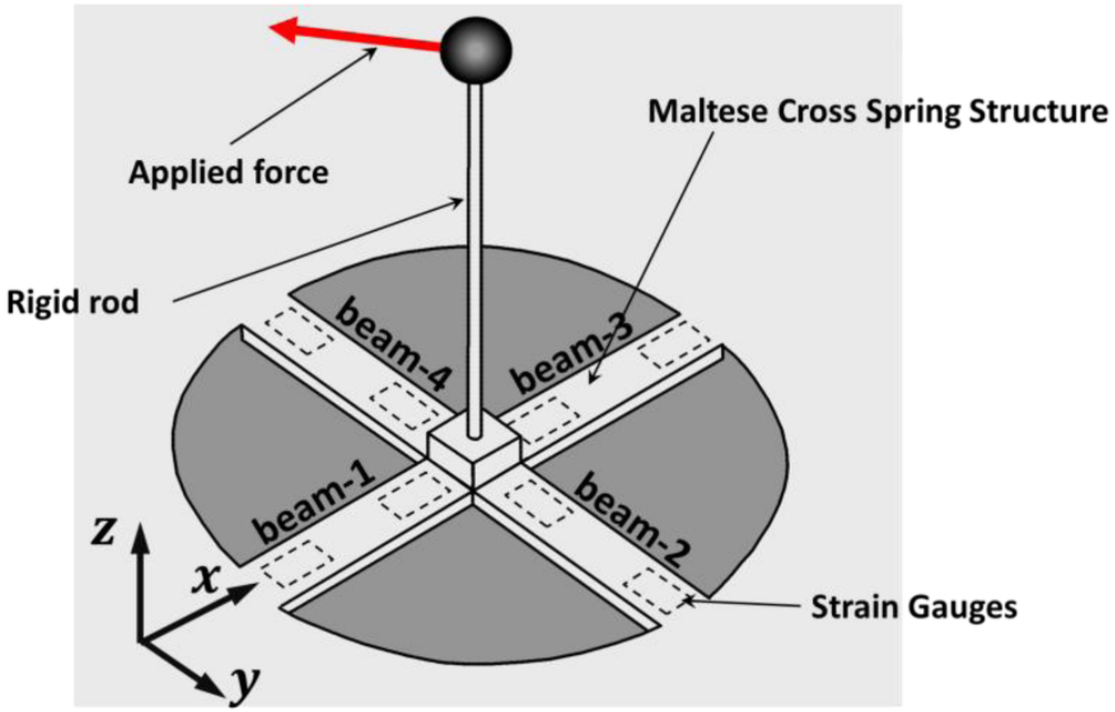

Figure 2.9: Maltese cross 6-DoF force torque sensor configuration [Fontana *et al*, 2012].

Two key types of multi axis force sensors are the 3-DoF linear force sensor and the 6-DoF linear and rotational force torque sensor. A 3-DoF linear force sensor can be simply constructed from three orthogonal load cells. A 6-DoF load cell requires at least six load cells for construction however one of the earliest methods of construction is a maltese cross configuration which utilises the equivalent of eight load cells as shown in figure 2.9 [Fontana *et al*, 2012].

There are a number of commercially available 6-DoF force torque sensors [ATI Industrial Automation, 2017, JR3 Inc., 2017, OptoForce Kft., 2016, Robotiq, 2017]. These have a number of limitations as they are typically designed for robotic manipulators. As a result they are designed for very large forces, which makes them insensitive to small forces such as those experienced by the rotors of a quadrotor. They are generally too heavy or have separate acquisition units making then unsuitable for use on a flying quadrotor. Furthermore these cost far too much to feasibly be integrated with quadrotors in any production capacity.

2.5.2 MEMS Barometer Tactile Sensors

Barometric pressure sensors are used for measuring air pressure. They operate by measuring the deflection of a load plate due to the air pressure difference on opposing sides of the plate. One

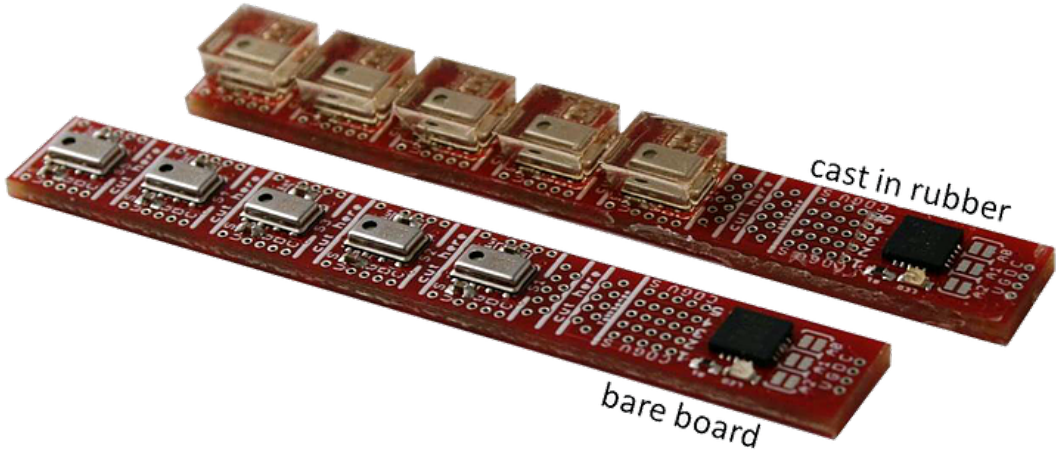

Figure 2.10: Tactile sensors available from RightHand Robotics [RightHand Robotics Inc., 2017].

key application of barometric pressure sensors is within pitot tubes on aeroplanes, where they measure the difference between still air and the oncoming wind [Ower and Pankhurst, 2014]. Through this pressure difference the airspeed of the aircraft can be estimated. Barometers can also be used to estimate altitude by measuring the ambient air pressure, which decreases with elevation above sea level, against a fixed reference.

MEMS barometers are constructed from a silicon load plate with properties that cause its electrical resistance to change as it is deflected [Rai-Choudhury, 2000]. The MEMS technology has enabled the construction of compact and low cost barometric pressure sensors which are now included in almost all new smart-phones. Given the highly sensitive load plate design offered by these sensors they can also be repurposed for measuring small mechanical forces beyond those imparted by air pressure.

One novel application of barometric pressure sensors is to utilise them as a tactile sensor, a method pioneered by Robert Howe's Biorobotics Lab at Harvard [Tenzer *et al*, 2014]. By casting MEMs barometric pressure sensors into a block of rubber Tenzer *et al* created a physical connection between the sensor element and the external surface of the rubber encapsulant, as shown in figure 2.10. This allowed them to utilise the barometric pressure sensor to measure contact forces and give robot grippers a sense of touch or tactile feedback.

The small contact forces which encapsulated pressure sensors are able to detect suggest that it may be possible to use this technology in the creation of a multi axis load cell. Such a system should be compact, cheap and sensitive enough to enable direct measurement of forces due to

second-order aerodynamic effects during flight.

2.5.3 Quadrotor Instrumentation

Force torque sensors have been used in the characterisation of rotors for quadrotors. Hoffmann *et al* used a multi-axis load cell and static test stand to characterise rotor thrust, torque and side force under various loads and simulated lateral wind conditions [Hoffmann *et al*, 2007]. Powers *et al* also used a static rotor test stand to measure the thrust force in various lateral wind and rotor speed configurations [Powers *et al*, 2013]. However they found that the results were not always consistent with observed free flight behaviour. Bangura *et al* used a load cell mounted rotor in combination with an axial and lateral wind generators to characterise aerodynamic power with varying inflow velocity and develop a closed loop thrust controller [Bangura *et al*, 2014]. Mueller and D'Andrea used a force torque sensor to characterise rotor performance for research into quadrotors operating with propeller failure [Mueller and D'Andrea, 2014].

Testing has also been extended by mounting an entire quadrotor to a fixed force torque sensor. Fields *et al* used a quadrotor mounted to a force torque sensor to measure the forces during simulated maneuvers for a hardware in the loop (HIL) simulation [Fields *et al*, 2015]. Intaratep *et al* used a quadrotor mounted to a load cell to compare the thrust and acoustic performance of various rotors inside an anechoic chamber [Intaratep *et al*, 2016]. Gioioso *et al* utilised a force sensing plate mounted to a wall to measure the forces exerted by a quadrotor as it made contact through a rigid tool [Gioioso *et al*, 2014].

These examples show some of the areas where force torque sensors have been used to measure and characterise rotor and quadrotor forces. However, to date there has not been any utilisation of force torque sensors to measure rotor forces during free air flight. It is expected that instrumented free flight will allow subtle aerodynamic forces and rotor interactions to be captured.

Chapter 3

Experimental Platform and Apparatus

Development of the apparatus focused on constructing a flexible control and command scheme that would allow for repeatable experiments and the capture of time-stamped measurements. This is essential to the collection of a statistically significant set of data over multiple trials and confidence in the result being observed. While it could be argued that an aggressive closed loop controller is the solution this could act to mask the impact of various aerodynamic effects.

3.1 Quadrotor Platform

Two aircraft were developed in the course of this research. The first platform, the ground effect flyer, was used during repeatability, ground effect, and interaction experiments, it features in Chapter 4. The second platform, the force measurement flyer, included a Raspberry Pi 3B and motor force sensors. It was used for rotor force and velocity experiments featured in Chapter 5. A review of common components and considerations when designing a quadrotor is presented in Section 2.4.

3.1.1 Power Regulation

For the application of investigating aerodynamic phenomena, passive obstacle avoidance and position control, thrust consistency and regularity in dynamic response are important parts of a research apparatus. In initial experiments, it was found that varying voltage over the course of several tests made results impossible to compare. For this reason, I seek to develop an onboard power regulation system that maintains constant battery voltage to the drive system. This is a challenging task due to the high instantaneous current demands during active maneuvers. Power regulation will allow us to better study the effects of coupled airstream-vehicle-object dynamics

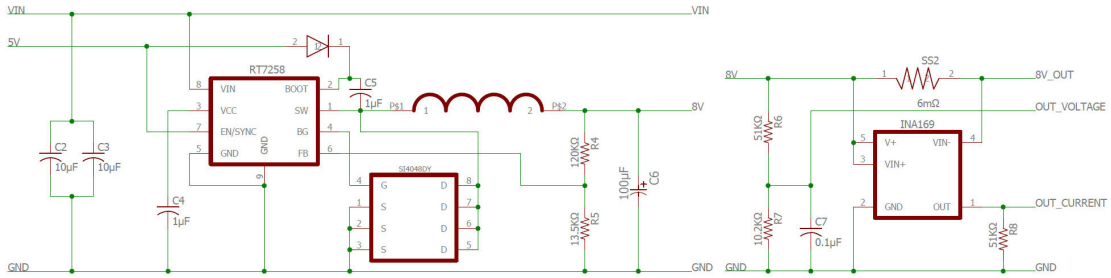

Figure 3.1: Schematic of the ground effect flyer power regulation circuit (left) and motor voltage sensor (right)

due to the uniformity of applied voltage, especially across multiple tests.

I developed a quadrotor platform equipped with onboard power regulation to provide constant voltage to the motor ESC. The current draw of the entire quadrotor in hover is 3.5 A. We designed a step-down buck regulator capable of supplying 6 A with a large output inductor to give a low output voltage ripple of 50 mV(pp) at full load. The ESCs receive a constant 8.1 V, even during periods of higher instantaneous current demand. The primary voltage regulator was combined with a 5 V regulator for avionics, power measurement sensors on the input and output of the regulator, and power and control signal distribution to the motor drivers and flight controller. The circuit diagram and Printed Circuit Board (PCB) are shown in figures 3.1 and 3.2 respectively.

The regulator PCB also forms the structure of the airframe. Two parallel woven carbon fibre tubes were attached using high strength double-sided tape and cable ties through the pairs of holes at each end. Woven carbon fibre was selected for its high torsional strength, as required in quadrotors [Davis *et al*, 2013]. The brushless motors were attached to these arms using 3D printed ABS mounts. The complete quadrotor is shown in figure 3.3.

A second iteration of the platform switched the regulator to a boost topology and reduced its size in order to create a more symmetric aircraft and save weight. The frame was instead constructed from two woven carbon fibre tubes notched and fitted together in an ‘X’ sandwiched between two thin woven carbon fibre centre plates.

3.1.2 Flight Hardware

In the ground effect flyer, the drive system consisted of four 100 mm 4x4.5 propellers each driven by a brushless 1306-3100 kV motor and KISS 12 A ESC. The main flight control board

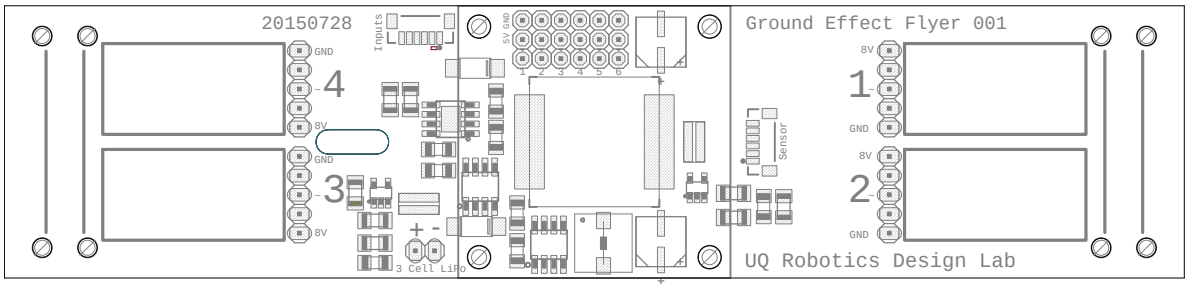

Figure 3.2: Ground effect flyer PCB layout at 1:1 scale

was a Sparky2 running Taulabs code. Two 2 cell 300 mAh Lithium-ion Polymer (LiPo) batteries supplied the power. The system could be configured to selectively disable the regulation subsystem. In the regulated voltage configuration the batteries were connected in parallel and regulated down to a constant 8.1V. In the unregulated configuration the batteries were connected in series to the ESCs directly, giving a varying voltage of 8.4V to 6.6V at cell exhaustion.

In the force measurement flyer the rotors were switched out in favour of larger and more flexible 6.5x3.5 propellers to enhance blade flapping and induced drag effects. Power was supplied by a 2 cell 950mAh LiPo battery. An additional 5V 3A regulator was used to power the onboard Raspberry Pi 3.

3.1.3 Position Tracking

Accurate position tracking is a fundamental requirement for investigating aerodynamic interactions on a quadrotor. These interactions are directly related to the motion of the quadrotor and its proximity to the environment, including the ground, walls and obstacles. As the position measurements will be differentiated to obtain the velocity of the quadrotor it is important to have high position and temporal resolution and accuracy.

The position of the quadrotor was tracked using an Optitrack Prime 13 motion capture system with twelve cameras spread over four 1.7 m tripods (see figure 3.4). A tracking frame comprised of four retro-reflective spheres was fixed to the quadrotor at the top, as shown in figure 3.3. Together this system is capable of tracking the quadrotor position and orientation with sub-mm resolution at a rate of 240 Hz.

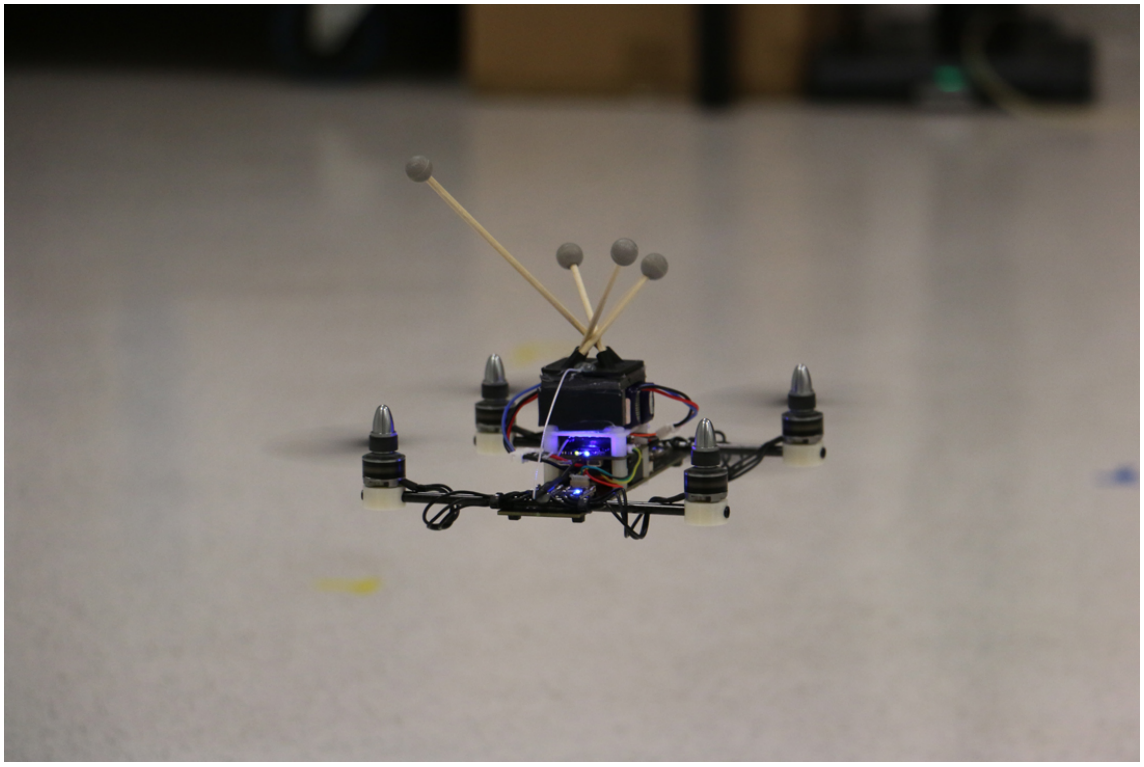

Figure 3.3: Mini quadrotor with voltage regulator

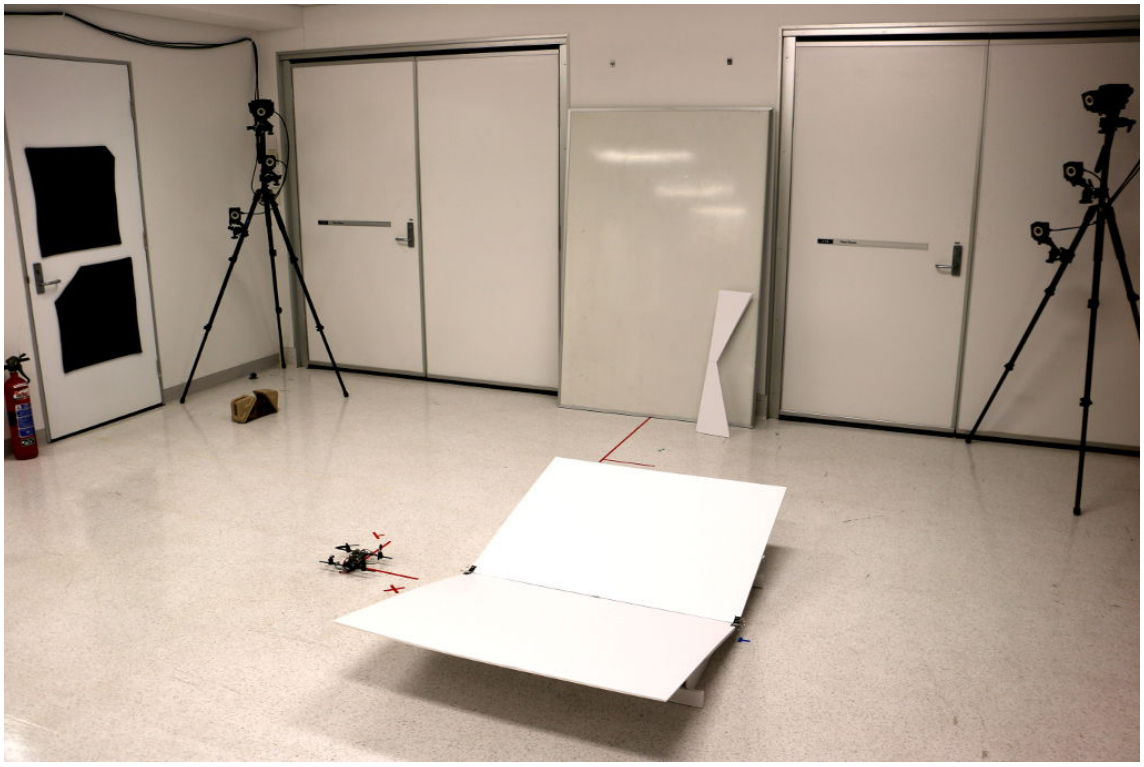

Figure 3.4: Experimental arena with interaction channel.

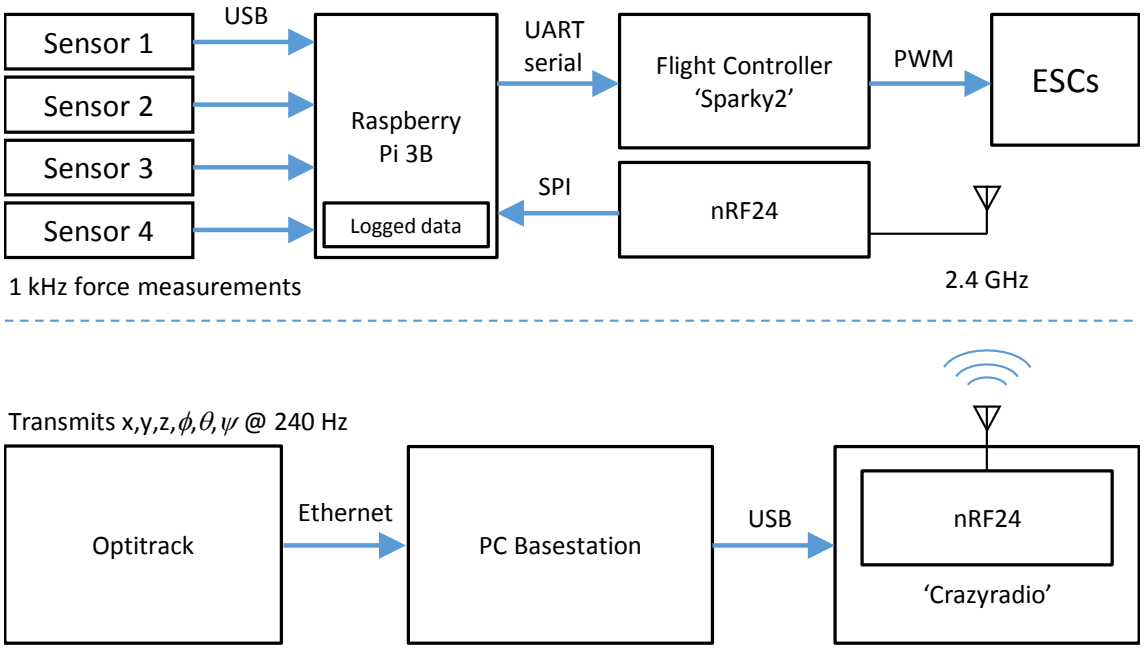

Figure 3.5: Sensor and Avionics Architecture.

3.1.4 Control and Command Architecture

For position control the current quadrotor pose needs to be transmitted to the onboard flight controller with minimal latency. This was achieved by using the burst mode on Nordic nrf24 radios. A USB crazyradio with a nrf24U01+ chip connected to the based station, Optitrack computer, transmitted to a nrf24L01+ module connected via SPI to UART converter to the quadrotor flight controller. The wireless link has a latency of 0.4 ms.

During each experiment the quadrotor was commanded, using a 3-DOF PD translational position controller, to take off and hover at 0.4 m above level ground for 10 s, during this time the average roll and pitch inputs were recorded. These were applied to all future control inputs as a constant adjustment offset to trim the vehicle.

The force measurement flyer has force sensors mounted under each rotor. The sensors are connected to a central processor for reading measurements and communicating via a wireless link to a basestation PC, see figure 3.5.

3.1.5 Interaction Furniture

To conduct experiments into the aerodynamic interaction of a quadrotor with surfaces it was necessary to construct structured environments which would allow interactions to be controlled

and adjusted precisely. To do this an array of 'interaction furniture' was constructed from large sheets of 5 mm foam core board.

A ground channel was constructed using 5 mm foam core board. The top surface of the channel was 1.0 by 1.6 m hinged in the middle lengthwise and supported by three cross members along its length. The cross members are cut to the specified angle for each configuration of channel slope. The complete channel is shown in figure 3.4.

A similar construction technique was used to construct the ramp for the dynamic repeatability experiments.

3.2 Validation of Dynamic Repeatability of Motion with Changing Battery Voltage

It is important to verify the functioning and repeatability of the aircraft trajectory control under regulated power to ensure that it is suitable for aerodynamics experiments. Consistent repetitions of each experiment are required to form a good understanding of these dynamic effects. A high gain controller is not a suitable solution to obtain consistency as the measurable impact of any aerodynamic effects will be masked by corrective action of the controller.

To test the quadrotor trajectory tracking consistency and height response over an uneven surface, an experimental arena was setup with a small ramp (see figure 3.6). The ramp is 1 by 1.6 m with a peak of 0.12 m. The quadrotor was commanded to follow the same pre-generated trajectory, for multiple laps, until the battery was exhausted or the quadrotor collided with the ramp. Four experiment configurations were tested, they are outlined in Table 3.1. The z and y axis performance during these experiments is shown in figures 3.7 and 3.8 respectively.

The results for the z axis show that the addition of a regulator improves feedback height control flight consistency (see figures 3.7a and 3.7c). Initially it appears that the addition of a regulator in the constant throttle configuration decreases performance in height tracking consistency (see figures 3.7b and 3.7d). However, the unregulated experiment had a significantly shorter duration, 25 vs 40 laps. It began with flying laps at the top of the height range, touching the ground at several points in the final laps and eventually impacting the ramp. Conversely, the regulated configuration maintained flight without contacting the ground or slope for the duration of the experiment.

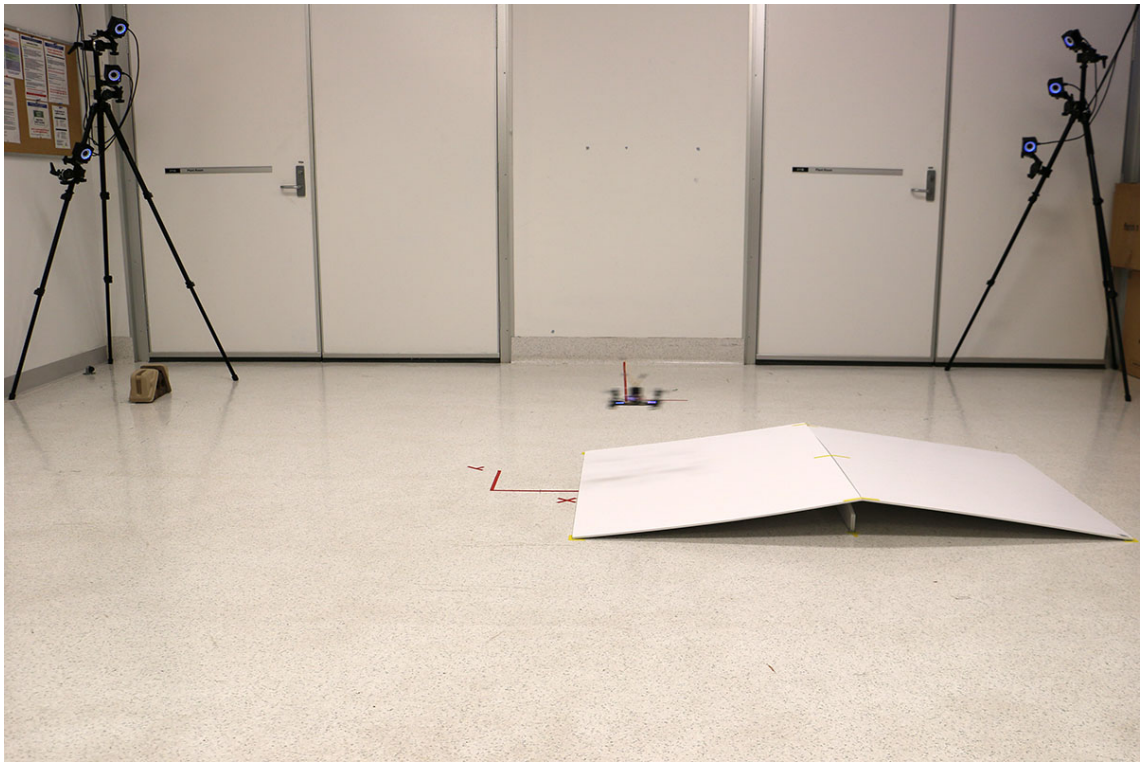

Figure 3.6: Experimental arena with uneven ground surface

From the y axis, with height control, it can be seen that the regulated voltage quadrotor offers greater consistency than the unregulated configuration, as shown by the smaller standard deviation and range (see figures 3.8a and 3.8c). This was expected, as the regulator should lead to uniform motor response. Constant throttle gave an unexpected result: in the case of the regulated quadrotor it lead to greater lateral consistency than all other configurations (see figure 3.8b), despite the large variation observed in the z axis.

This improvement in lateral consistency observed is thought to be due to a coupling between the height and position on-board controllers. By removing the height controller, the lateral position controller is able to achieve greater repeatability as the motors are only changing speed in relation to the attitude commands, without reducing throttle headroom to affect height control (see figure 3.9). This allows the motors to respond more quickly as the changes in speed required will be smaller. The regulator buffers the power bus, allowing the voltage sag due to instantaneous current demand to be resisted.

The unanticipated improvement in performance for the regulated platform without height control raises interesting questions about the tradeoffs being made in attempting to slavishly follow prescribed trajectories, rather than accepting consistent performance for less strictly pre-

Table 3.1: Configurations for path following experiments

Exp.	Supply Voltage	Throttle Control	Achieved Laps
(a)	regulated	height feedback	41
(b)	regulated	fixed value (44.4%)	40
(c)	unregulated	height feedback	46
(d)	unregulated	fixed value (46.8%)	25

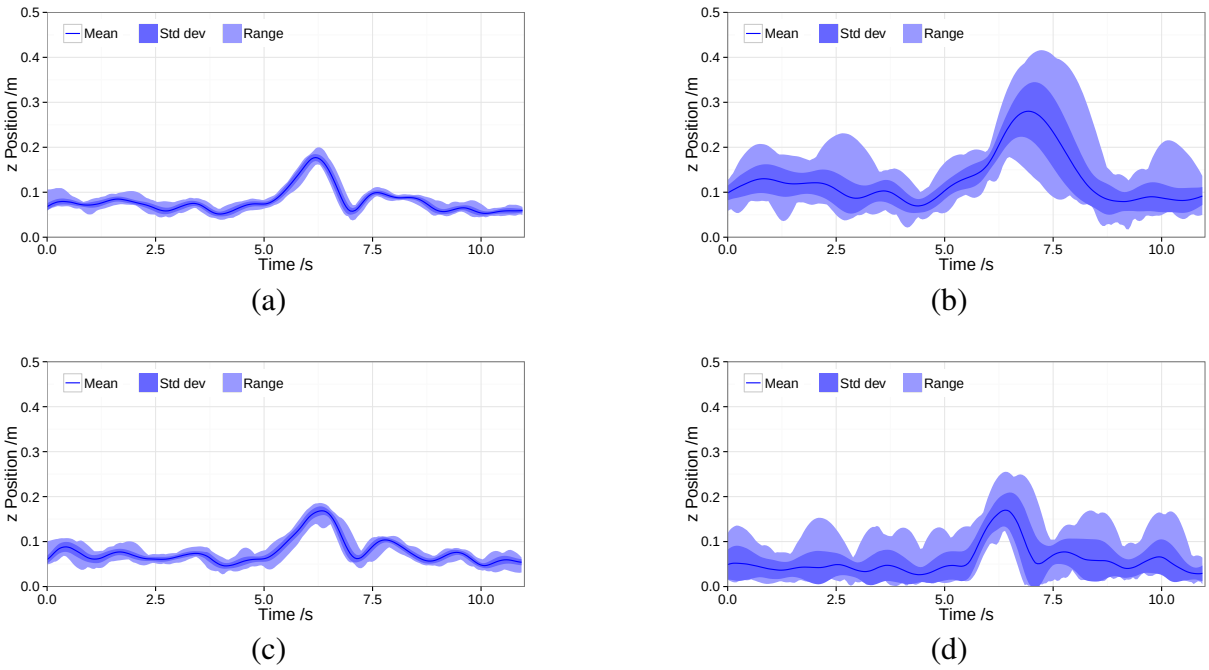

Figure 3.7: z axis path following consistency, configurations a–d as outlined in Table 3.1

scribed paths. This may have ramifications for developing more robust flight control schemes for maneuvering through complex environments.

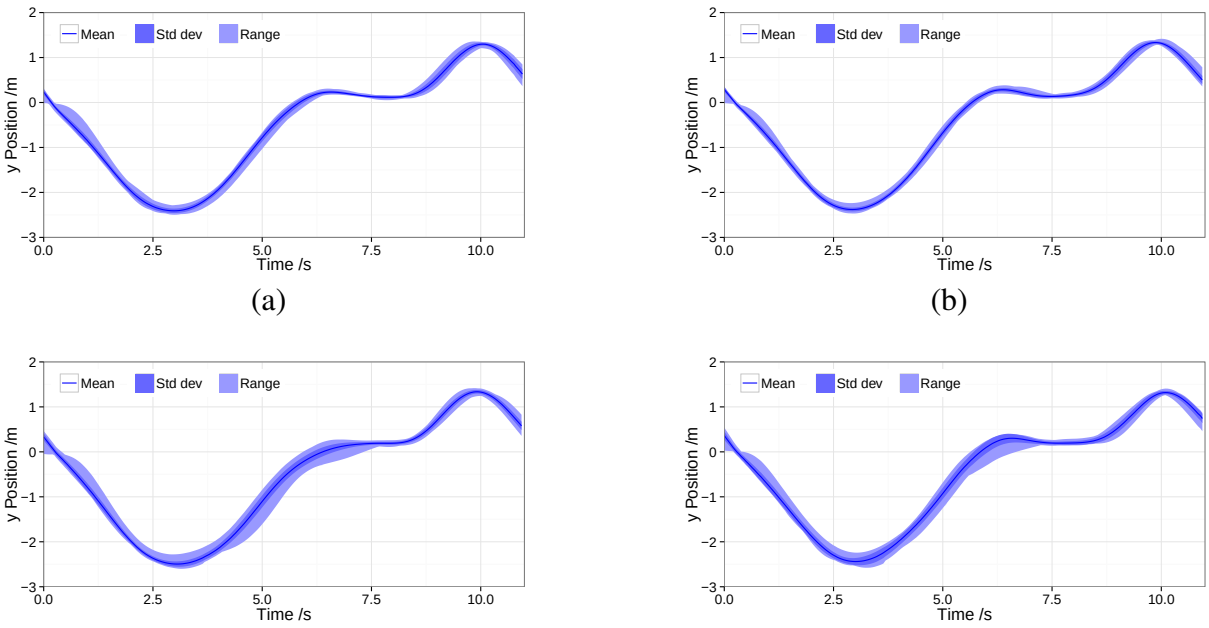

Figure 3.8: *y* axis path following consistency, configurations a–d as outlined in Table 3.1

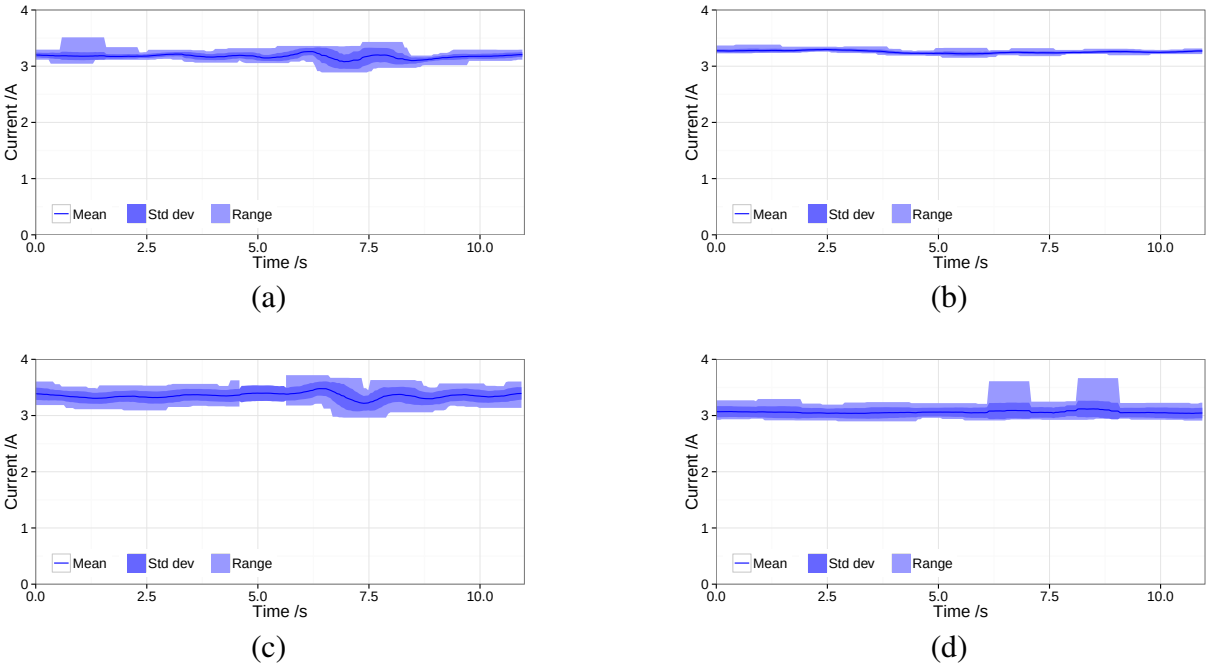

Figure 3.9: Supply current during path following, configurations a–d as outlined in Table 3.1

Chapter 4

Aerodynamic Force Interactions

While flight control of robot aircraft conventionally employs active feedback to maintain the desired trajectory, some designs — most notably fixed-wings — use passive stabilisation techniques that do not require additional sensing and actuation. This chapter reports development of a miniature multirotor craft that uses passive aerodynamic feedback to stabilise position and avoid obstacles and surfaces. Of particular interest are two key capabilities: self-stabilisation of altitude in ground effect and self stabilisation of lateral position.

Passive height control exploits the increase in thrust due to ground effect when flying close to the ground. This phenomenon is well known [Leishman, 2002, Prouty, 1995, Sharf *et al*, 2014]; Kushleyev *et al* found that micro rotors within 1 rotor radii to the ground required 15 per cent less power to hover [Kushleyev *et al*, 2013]. By setting the throttle slightly below that required to hover in free air, the aircraft will descend until the increased thrust exactly balances gravity. However, the dynamics of hovering thrust are complicated by coupled rotor speed mechanics and inflow dynamics of the rotor system — passive vertical motion must be shown to be stable.

Passive horizontal behaviour is less strongly expressed and less explored. When a quadrotor is flying close to a wall it is sometimes repelled and sometimes attracted to the wall. There is, as far as we are aware, no published exploration of these phenomena.

4.1 Ground Effect Model Comparison

The regulated drive voltage of the micro quadrotor testbed provides a useful platform for calibrating the aerodynamic ground effect performance of the aircraft. This has previously been done for full-size helicopters [Cheeseman and Bennett, 1955, Heyson, 1977], but not for quadrotors [Bangura and Mahony, 2012].

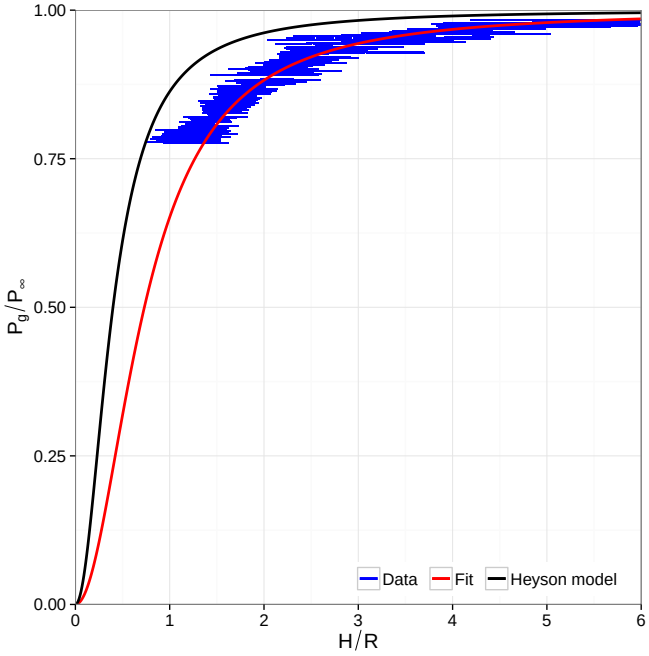

Figure 4.1: Experimental results for normalised hover power vs height with model

The regulated quadrotor was commanded to maintain lateral position over flat ground with fixed throttle, and allowed to come to equilibrium hover altitude over 30 seconds. In each experiment, the throttle was decreased from 44.8 per cent to 41.6 per cent in steps of 0.2 per cent. Total power to the motors was measured along with vertical position of the quadrotor. From this, we calculated the power ratio required to hover compared to free air, as a function of normalised hover height relative to single rotor radius (see figure 4.1). Where the single rotor radius is the hub to tip distance for each of the four identical rotors.

The results follow the general trend for a helicopter presented by Heyson [Heyson, 1977]. However, it is clear that ground effect has a greater effect on the quadrotor relative to its rotor size. We believe this is due to the rotor wake interaction from multiple rotors in proximity, entraining airflow in the central volume of the vehicle. Adjusting for fit, we find that a correction factor of $B = 2.5$ — reflecting the equivalent distance from the outside rotor tip to the centre of the quadrotor times the rotor radius — gives a compelling fit. We posit that this is a more appropriate dimension for estimating ground effect for multirotors.

Furthermore, ground effect is commonly held to be negligible for helicopters beyond 2 to 3 rotor radii from the ground. However, we found that with a quadrotor the ground effect zone extends up 5 to 6 single blade rotor radii, a result which has also been observed by Sharf *et al* [Sharf *et al*, 2014]. We believe that this is due to the concentrated stream tubes of small

rotors.

4.2 Passive Altitude Stability and Ground Effect Interaction

The vertical dynamics of a rotor have often been modeled with tacit assumptions about constancy of power, thrust or rotor speed, but this is not the case for a rotor moving vertically close to ground. The rotor has numerous dynamic states:

- Power bus voltage
- Drive circuit current draw
- Rotor angular velocity
- Inflow velocity
- Airfoil induced angle
- Height above ground
- Vertical velocity

Of these, bus voltage and current draw are usually measured, and rotor angular velocity is often available, integrated into the motor's electronic speed controller. Height above ground and vertical velocity are sometimes available with added sensors such as GPS; Rotor inflow velocity and airfoil induced angle are only rarely measured. Consequently, rotor velocity is often closely regulated, with longer control loops around aircraft position and velocity. Thus, their interactions are typically not observed in practice. The relationships between rotor speed, vertical motion and air flow mechanics are typically treated as instantaneous and abstracted into thrust generation. These unsensed and uncontrolled states must be intrinsically stable for systems where the only feedback is passive aerodynamic interaction.

4.2.1 Rotor Coupled Dynamics Model

The vertical motion of a simple quarter-quadrotor model, ignoring pitching and rolling, is given by simple Newtonian mechanics:

$$m\ddot{z} = -mg + T \tag{4.1}$$

where m is the rotor system mass, z is rotor height above ground, g is acceleration due to gravity and T is the applied thrust.

Basic motor electrodynamics can be modelled with a simple linear system:

$$V = \omega\lambda + iR_d \tag{4.2}$$

$$\mathrm{I}_r\dot{\omega} = \lambda i - Q \tag{4.3}$$

where V is the battery voltage, ω is the rotor angular velocity, λ is the motor flux-linkage coefficient, i is the drawn electrical current, R_d is the combined drive circuit resistance (motor plus battery), I_r is the rotor rotational inertia and Q is the rotor drag torque. Lithium polymer cells can exhibit impulse responses with peak and relaxation behaviour [Pounds *et al*, 2009]; it is expected that fast voltage regulation will eliminate this dynamic.

Using a BEM model for free-air thrust and drag, with non-constant inflow velocity [Prouty, 1995], using airfoil lift-slope and variable inflow angle in place of a non-dimensionalised thrust coefficient:

$$T_{FA} = \frac{a\sigma}{4}\alpha\rho AR^2\omega^2 \tag{4.4}$$

$$Q = \frac{(a\sigma)^{3/2} + 2b\sigma}{16}\alpha^{3/2}\rho AR^3\omega^2 \tag{4.5}$$

$$\alpha = \theta - \frac{v_i}{\omega R} - \frac{\dot{z}}{\omega R} \tag{4.6}$$

where T_{FA} is the equivalent free-air thrust, a and b are the rotor airfoil lift and drag slopes, σ is the rotor disc solidity ratio, θ is the fixed geometric rotor tip angle, v_i is the induced velocity, R is the rotor radius, ρ is the density of air and A is the rotor disc area. The term α is collectively the variable airfoil angle of attack; vertical velocity term $\dot{z}/\omega$ gives rise to passive inflow damping.

The Cheeseman and Bennett model is used for scaling the thrust generated in ground effect [Cheeseman and Bennett, 1955, Leishman, 2002]:

$$T_{GE} = \frac{1}{1 - (\frac{BR}{4z})^2}T_{FA} \tag{4.7}$$

where T_{GE} is the thrust generated in proximity to the ground, R is the rotor radius and z is rotor height above ground, and B is a rotor radius scaling parameter — typically taken as $B = 1$ for

helicopters.

The inflow velocity is problematic — it is difficult to measure during flight, and depends on the generated thrust, ground effect, lateral flight motion and ground surface geometry. Carpenter and Fridovich associate a temporal delay with the air's response, which they call 'apparent mass' [Carpenter and Fridovitch, 1953], but we consider this negligible on the scales of micro drones and do not treat it as a dynamic state. Instead the induced velocity-thrust relationship is used to facilitate the incorporation of ground effect [Prouty, 1995, p4]:

$$v_i = \sqrt{\frac{T}{2\rho A}} \tag{4.8}$$

Note that the inflow velocity depends on the thrust generated, which itself is effected by the magnitude of rotor inflow.

Solving the complete electromechanical non-linear dynamical system explicitly is challenging, and simulating it requires resolving the recursive inflow velocity calculation. Leishman notes that ground effect can be assumed to influence induced power only [Leishman, 2002, p260]. The free air thrust value T_{FA} can therefore be used for computing the inflow angle correction in rotor drag, and the drag mechanic does not inform the calculation for v_i. The BEM and momentum theory thrust inflow relation are linked to get a closed-form description for $T_F A$:

$$T_{FA} = \frac{1}{4}\left[\frac{K\omega R}{\sqrt{2\rho A}} - \left(\frac{(K\omega R)^2}{2\rho A} + 4K(\theta\omega R - \dot{z})\omega R\right)^{\frac{1}{2}}\right]^2 \tag{4.9}$$

where $K = \frac{a\sigma}{4}\rho A$ is a constant coefficient. This then yields a straight-forward expression for v_i from (4.8) to apply to (4.6):

$$v_i = \frac{\left((a\sigma\omega R)^2 - 32a\sigma\omega R(\dot{z} - \theta\omega R)\right)^{1/2} - a\sigma\omega R}{16} \tag{4.10}$$

4.2.2 Vertical Stability

The system was implemented in Matlab Simulink to simulate a quadrotor with constant voltage flying close to the ground (see figure 4.2). The quadrotor has the parameters of the ground effect flyer in Chapter 3, as given in Table 5.2. The simulation initial conditions are $z_0 = 0.5$, $\dot{z}_0 = 0$, $\omega_0 = 1150$, with $V = 7.4$ at 49 per cent throttle setting.

Table 4.1: Micro Quadrotor Simulation Parameters

I_r	Rotor inertia	0.001	kgm^2
m	Quarter mass	$0.2/4$	kg
θ	Blade tip angle	$6.8\frac{pi}{180}$	rad
σ	Rotor solidity ratio	0.1273	
R	Rotor radius	0.05	m
A	Rotor area	0.0157	m^2
a	Airfoil lift slope	5.5	rad^{-1}
b	Airfoil drag slope	0.1215	rad^{-1}
λ	Flux linkage coefficient	0.0031	NmA^{-1}
R_d	Drive circuit resistance	0.02	Ω

It can be seen that the vertical velocity decays to zero and the height above ground converges to a constant value. The rotor speed and current draw are approximately constant. Small variation in inflow velocity and thrust caused by ground effect can be seen. When the quadrotor moves close to the ground, the inflow velocity decreases and thrust increases significantly. This shows that supplying a constant voltage to the quadrotor will allow passive height stability to be achieved. It is useful to note that, for small motions around the equilibrium hover height in ground effect, the behaviour of the system is approximately linear.

The simulation was replicated in experiment with the test platform and exhibited similar large-scale behaviour (see figure 4.3), including the asymmetrical sharp 'bounce' as the aircraft approaches the ground. The physical experiment exhibited a slower oscillation period than the simulated result (2.3 s compared to 0.6 s), possibly due to parameter estimation error or unmodelled damping (eg. airframe drag).

Further examination of this difference showed that the simulation model is sensitive to the estimation of the rotor tip angle. Changing the rotor tip angle from 6.8 to 9.75 degrees resulted in a much slower oscillation period as shown in figure 4.4. This leads to good temporal agreement with the experimental results. Both values of rotor tip angle are reasonable for the rotor used as it tapers to a point making a true tip angle difficult to measure directly. It also highlights the potential inadequacies of modeling the rotor using few parameters.

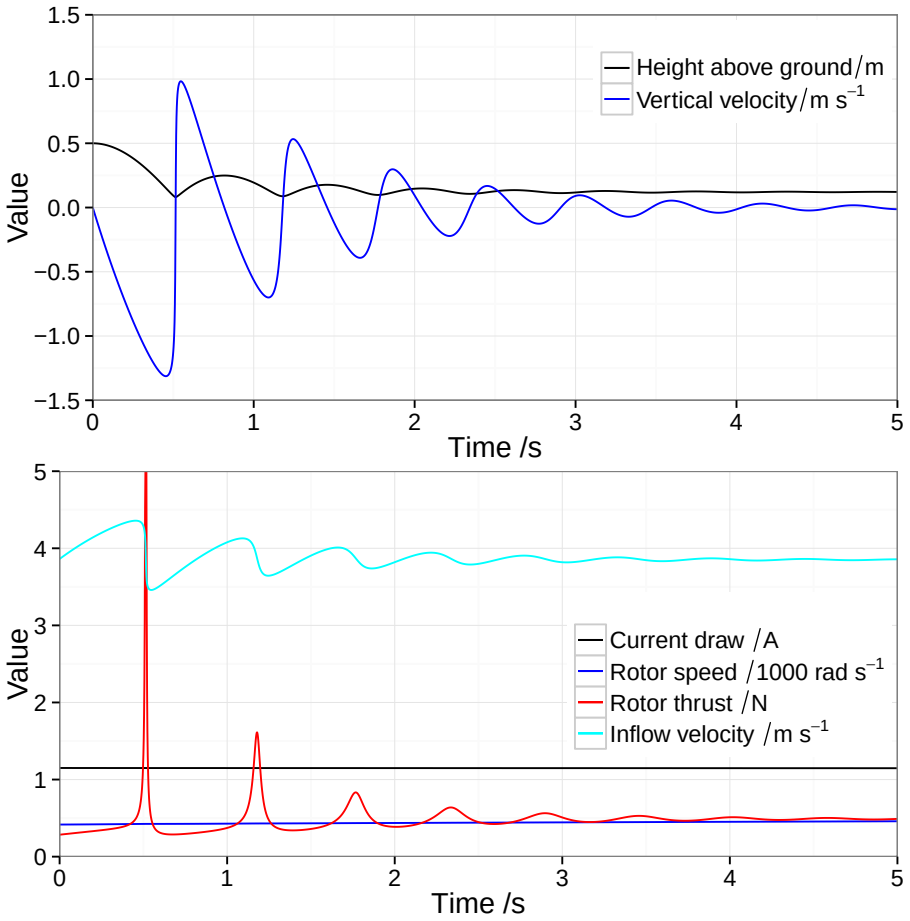

Figure 4.2: Simulation results for a rotor in ground effect with a constant voltage

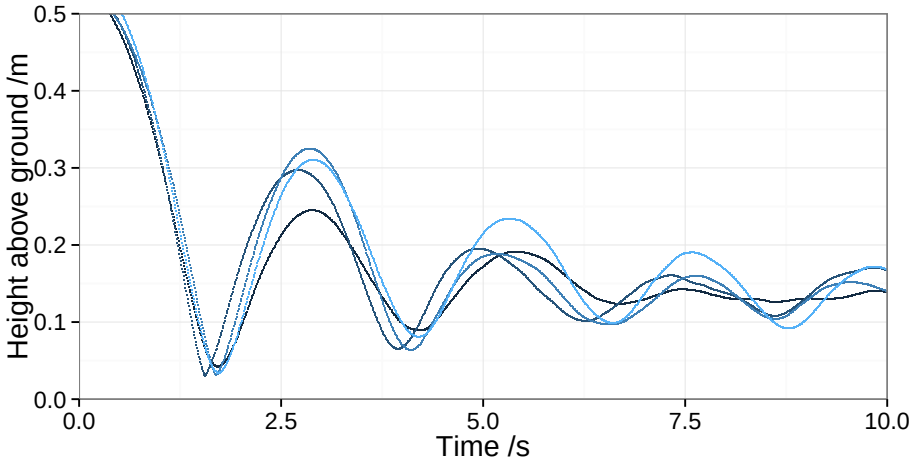

Figure 4.3: Experimental results for quadrotor in ground effect with a constant voltage

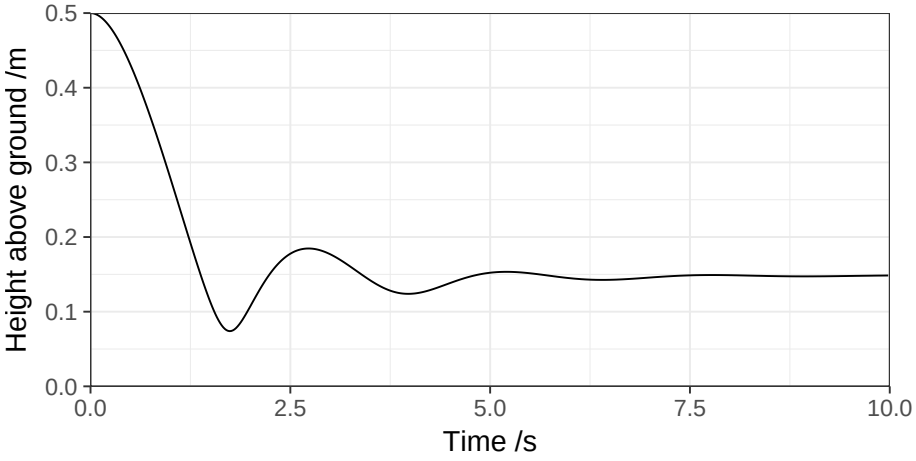

Figure 4.4: Simulated height response with tip angle increased to 9.75 degrees

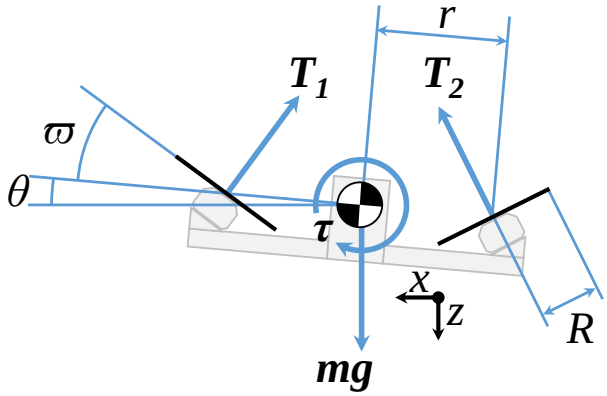

Figure 4.5: Free body diagram of a quadrotor with canted rotors

4.3 Free Air Canted Rotor Velocity Stability

In free air, the velocity of a typical quadrotor is lightly damped by drag: given an initial velocity, it will travel for some distance before coming to rest. In contrast, a quadrotor with canted rotors will exhibit rotor inflow damping, in which some component of sideways oncoming air will enter the top or bottom surface of the rotors, locally changing the angle of attack of the blades and thus producing a change in thrust counteracting the direction of translation. A quadrotor with canted rotors can be shown to be stable in velocity. However, neither is stable in position.

Consider a canted quadrotor in free air (see figure 4.5). The equations of motion are:

$$m\ddot{x} = -\sin(\varpi+\theta)T_1 + \sin(\varpi-\theta)T_2 \tag{4.11}$$

$$m\ddot{z} = -\cos(\varpi+\theta)T_1 - \cos(\varpi-\theta)T_2 + mg \tag{4.12}$$

$$I\ddot{\theta} = T_1 r\cos\varpi - T_2 r\cos\varpi + \tau \tag{4.13}$$

where x, z, and θ are the horizontal position, vertical position and pitch angle of the quadrotor respectively; m is the mass of the quadrotor; g is acceleration due to gravity; I is the moment of inertia in pitch; T_1, and T_2 are the rotor thrust forces; r is the distance between rotor and quadrotor centres; τ is the torque produced by the onboard pitch feedback control; and ϖ is the rotor cant angle.

Assuming that the quadrotor is flying at a constant vertical height, the rotor thrust forces T_1 and T_2 decompose into two components: steady state hover thrust, and force due to rotor inflow damping. Hover thrust is given by:

$$T_h = \frac{mg}{2\cos\varpi} \tag{4.14}$$

Axial motion of a rotor through its own induced flow produces a change in thrust, which can be treated as a simple damper [Pounds and Dollar, 2010].

$$F_{RD} = -c_{RD}\dot{d} \tag{4.15}$$

where, $\dot{d}$ is the velocity of the rotor through the air. The damping coefficient is given by:

$$c_{RD} = \left[\frac{a}{4}\frac{\sigma}{\omega R}\right]\rho\pi R^2(\omega R)^2 \tag{4.16}$$

where, a is the blade lift slope; σ is the rotor solidity ratio; ω is the rotor angular velocity; R is the rotor radius; and ρ is the air density.

The total thrust forces are given by:

$$T_1 = T_h - c_{RD}(\dot{x}\sin\varpi + (\dot{\theta}r - \dot{z})\cos\varpi) \tag{4.17}$$

$$T_2 = T_h - c_{RD}(-\dot{x}\sin\varpi + (-\dot{\theta}r - \dot{z})\cos\varpi) \tag{4.18}$$

Attitude PD feedback control is treated as an applied torque given by:

$$\tau = k_p(\theta + k_d\dot{\theta}) \tag{4.19}$$

where, k_p and k_d are proportional and derivative gains respectively.

Combining (4.11), (4.13) and (4.17–4.19), and linearising, yields an expression for coupled

translational and pitch dynamics:

$$m\ddot{x} = -2c_{RD}\dot{x}\sin^2\varpi - \dot{\theta}c_{RD}r\sin(2\varpi) - \theta mg \tag{4.20}$$

$$I\ddot{\theta} = -c_{RD}2r\cos\varpi(\sin\varpi\dot{x} + \cos\varpi r\dot{\theta}) - k_p(\theta + k_d\dot{\theta}) \tag{4.21}$$

Substituting (4.21) into (4.20) and taking the Laplace transform yields the characteristic polynomial of translational mechanics:

$$a_4s^4 + a_3s^3 + a_2s^2 + a_1s \tag{4.22}$$

where,

$$a_4 = Im \tag{4.23}$$

$$a_3 = 2mc_{RD}r^2\cos^2\varpi + mk_pk_d + 2Ic_{RD}\sin^2\varpi \tag{4.24}$$

$$a_2 = mk_p + 2c_{RD}k_pk_d\sin^2\varpi \tag{4.25}$$

$$a_1 = 2c_{RD}\sin\varpi(k_p\sin\varpi - mgr\cos\varpi) \tag{4.26}$$

This system has a pure integrator which results in neutral stability in position, at best; however it does exhibit velocity stability.

Consider instead the characteristic polynomial of the differentiated system:

$$a_4s^3 + a_3s^2 + a_2s + a_1 \tag{4.27}$$

To satisfy the Routh-Hurwitz stability criteria, $a_n > 0$ and $a_3a_2 > a_4a_1$.

Given that all system parameters are positive, $a_n > 0$ will be satisfied so long as $k_p\sin\varpi > mgr\cos\varpi$. Setting $\varpi = 0$ would result in $a_1 = 0$ and the system would have a second pure integrator, as per a typical quadrotor with level rotors. Given k_p, r, m and ϖ may be set freely, choosing some reasonable $\varpi > 0$ and adjusting the other parameters, the inequality can be satisfied.

Similarly $a_3a_2 > a_4a_1$ will always be satisfied. Taking the sum $a_3a_2 - a_4a_1$ it can be shown

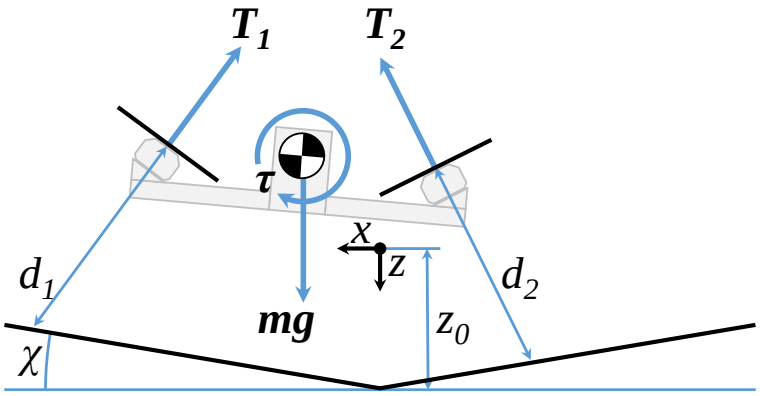

Figure 4.6: Free body diagram of a quadrotor in ground effect channel

that it is comprised of only positive elements:

$$\begin{aligned} a_3a_2 - a_4a_1 \;=\; & 2m^2r^2k_pc_{RD}\cos^2\varpi \\ & +4mr^2k_pk_dc_{RD}\sin^2\varpi\cos^2\varpi \\ & +m^2k_p^2k_d \\ & +2mk_p^2k_d^2c_{RD}\sin^2\varpi \\ & +4Ik_pk_dc_{RD}^2\sin^4\varpi \\ & +2Im^2grc_{RD}\sin\varpi\cos\varpi \end{aligned} \tag{4.28}$$

Thus, the system is stable in velocity and will come to rest, if perturbed, with some accumulated position error.

4.4 Lateral Position Stability Through Ground Effect Interaction

With the addition of a sloped ground surface, a canted quadrotor flying in ground effect (see figure 4.6) can be shown to be stable in position. Constant height control is achieved by providing a constant power to the rotors and hovering within the ground effect zone, since power required to hover decreases quadratically with height as per Section 4.1 [Heyson, 1977].

Rotor thrust forces T_1 and T_2 now contain an additional component, the ground effect force.

Around equilibrium conditions ground effect can be treated as a simple spring [Pounds and

Dollar, 2010].

$$F_{GE} = -k_{GE} d \tag{4.29}$$

where the spring constant is given by:

$$k_{GE} = \frac{32R^2 d_0}{(R^2 - 16d_0^2)^2} \tag{4.30}$$

where d is the distance between the rotor and the channel, and d_0 is this distance when hovering at the origin.

$$d_0 = (z_0 - r\sin\chi)\frac{\cos\chi}{\cos(\varpi - \chi)} \tag{4.31}$$

where z_0 is the distance of the origin above the channel bottom; and χ is the channel angle.

Thrust forces are given by:

$$T_1 = T_h - k_{GE} d_1 - c_{RD}(\dot{x}\sin\varpi + (\dot{\theta}r - \dot{z})\cos\varpi) \tag{4.32}$$

$$T_2 = T_h - k_{GE} d_2 - c_{RD}(-\dot{x}\sin\varpi + (-\dot{\theta}r - \dot{z})\cos\varpi) \tag{4.33}$$

The distances between the rotors and the sides of the channel are given by:

$$d_1 = d_0 + (z - x\sin\chi + \theta r)\frac{\cos\chi}{\cos(\varpi - \chi + \theta)} \tag{4.34}$$

$$d_2 = d_0 + (z + x\sin\chi - \theta r)\frac{\cos\chi}{\cos(\varpi - \chi - \theta)} \tag{4.35}$$

again, assuming that the quadrotor is flying at a constant vertical height.

Combining equations (4.11), (4.13) and (4.32–4.35), and linearising, yields an expression for coupled translational and pitch dynamics:

$$\begin{aligned} m\ddot{x} &= -2k_{GE}(x\sin\chi + \theta r)\cos\chi\sin\varpi\sec(\varpi - \chi) \\ &\quad -2c_{RD}\dot{x}\sin^2\varpi - \dot{\theta}c_{RD}r\sin(2\varpi) - \theta mg \end{aligned} \tag{4.36}$$

$$\begin{aligned} I\ddot{\theta} &= -k_{GE} r\cos\varpi\frac{2\cos\chi}{\cos(\chi - \varpi)}(\theta r - x\sin\chi) \\ &\quad -c_{RD}2r\cos\varpi(\sin\varpi\dot{x} + \cos\varpi r\dot{\theta}) - k_p(\theta + k_d\dot{\theta}) \end{aligned} \tag{4.37}$$

Substituting (4.37) into (4.36) and taking the Laplace transform yields the characteristic

polynomial of translational mechanics:

$$a_4 s^4 + a_3 s^3 + a_2 s^2 + a_1 s + a_0 \tag{4.38}$$

where,

$$\begin{aligned}
a_4 &= Im && (4.39)\\
a_3 &= 2mc_{RD}r^2\cos^2\varpi + mk_pk_d + 2Ic_{RD}\sin^2\varpi && (4.40)\\
a_2 &= mk_p + mc_1r^2\cos\varpi + Ic_1\sin\chi\sin\varpi \\
&\quad + 2c_{RD}k_pk_d\sin^2\varpi && (4.41)\\
a_1 &= 4c_1c_{RD}r^2\sin\chi\sin\varpi\cos^2\varpi \\
&\quad + c_1k_pk_d\sin\chi\sin\varpi \\
&\quad + 2c_{RD}\sin\varpi(k_p\sin\varpi - mgr\cos\varpi) && (4.42)\\
a_0 &= k_pc_1\sin\chi\sin\varpi + 2c_1^2r^2\sin\chi\sin\varpi\cos\varpi \\
&\quad + mgc_1r\sin\chi\cos\varpi && (4.43)
\end{aligned}$$

and,

$$c_1 = 2k_{GE}\cos\chi\sec(\chi-\varpi) \tag{4.44}$$

For a fourth order characteristic polynomial, the Routh-Hurwitz stability criterion requires, $a_n > 0$, $a_3a_2 > a_4a_1$, and $a_3a_2a_1 > a_4a_1^2 + a_3^2a_0$. As the system is known to be stable in free air, out of ground effect, $k_p\sin\varpi > mgr\cos\varpi$ and thus $a_n > 0$. Satisfying $a_3a_2a_1 > a_4a_1^2 + a_3^2a_0$ necessarily satisfies $a_3a_2 > a_4a_1$, as $a_n \in \mathbb{R}^+$.

The coefficients are dominated by a_2, due to the k_pm term which is large compared to the products of I. Coefficients a_4 and a_0 are small as they contain common factors of I and k_{GE} respectively, which are both usually small. Therefore, $a_3a_2a_1 > a_4a_1^2 + a_3^2a_0$ will be satisfied for typical quadrotors, and the system will be stable in position.

This stability was analytically assessed for both small and large quadrotor configurations with parameters detailed in Tables 4.2 and 4.3 respectively, and the craft were found to be stable.

It is important to note that the cant of the rotors is necessary for position stability. Consider

Table 4.2: Aircraft and control parameters for a small quadrotor

Aircraft Parameters					
g	9.81	ms^{-2}	ρ	1.184	kgm^{-3}
m	0.215	kg	I	0.000539	kgm^2
ω	1570	$rads^{-1}$	R	0.05	m
a	5.5	rad^{-1}	r	0.06	m
ϖ	0.262	rad	χ	0.262	rad
d_0	0.075	m			
Control Parameters					
k_p	7.0		k_d	0.5	
Model Parameters					
c_{RD}	0.128		k_{GE}	0.784	

Table 4.3: Aircraft and control parameters for a large quadrotor [Pounds, 2007]

Aircraft Parameters					
g	9.81	ms^{-2}	ρ	1.184	kgm^{-3}
m	4.34	kg	I	0.0820	kgm^2
ω	870	$rads^{-1}$	R	0.165	m
a	5.5	rad^{-1}	r	0.315	m
ϖ	0.262	rad	χ	0.175	rad
d_0	0.5	m			
Control Parameters					
k_p	400.0		k_d	0.3	
Model Parameters					
c_{RD}	1.08		k_{GE}	0.0276	

a quadrotor with flat rotors, $\varpi = 0$, in this case $a_1 = 0$. Therefore, $a_3a_2a_1 = 0$ and the inequality $a_3a_2a_1 > a_4a_1^2 + a_3^2a_0$ can not be satisfied. Thus, quadrotors with level rotors derive no benefit from a symmetric sloped channel. However, as the instability is due to an unstable pole pair, the flat rotor configuration exhibits repulsive behaviour, such that the robot rebounds from the sides of the channel. This can be exploited by a single sided slope design to repel even conventional level-rotor quadrotors away from walls and obstacles, with no modification required.

Examining the size of the smallest real pole in figure 4.7 the relative position stability of the system can be assessed: increasing the channel slope degrades stability; increasing rotor cant improves stability. It is also apparent that rotor cant has a greater impact on stability than channel slope for the same angular variation.

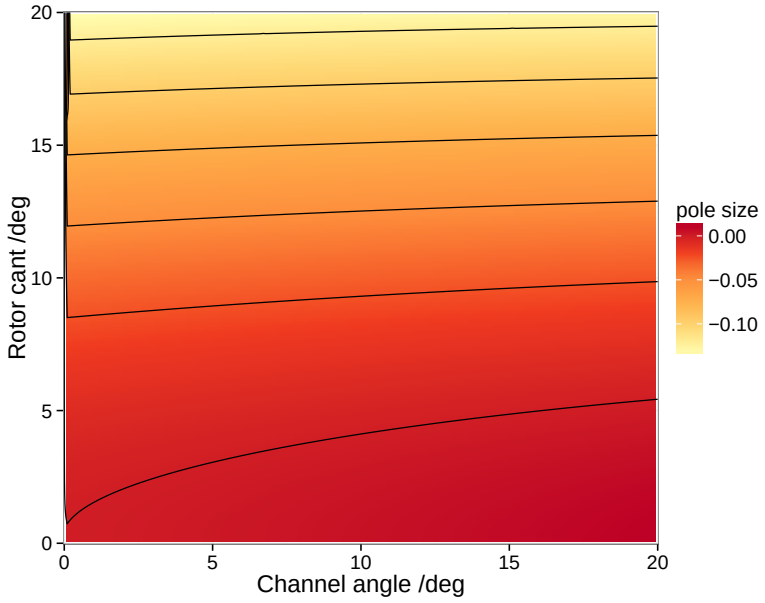

Figure 4.7: Size of the minimum real pole vs rotor cant and channel angle

4.5 Passive Position Keeping Experiments

An array of experiments was carried out to explore the passive lateral position stability of a quadrotor in a ground effect channel, testing a matrix of rotor cant and channel slope combinations. Rotor cant was varied from 0° to 20° and channel slope angle from 5° to 20°, both in 5° increments. Below 20° rotor cant, the reduction in vertical thrust is low — less than 6 per cent — beyond this the power penalty becomes more significant. We also conducted these tests over flat ground with flat rotors and 15° canted rotors. The experimental setup is shown in figure 4.8.

The quadrotor was trimmed and then flown over the middle of the sloped channel to an initial position 0.2 m offset from the centre line. The throttle was set to a constant value just below hover thrust, adjusted for rotor cant, and the lateral position control was disabled. The quadrotor was allowed to respond for 30 s before control was resumed, and the aircraft returned to the start position. Ten trials were conducted for each configuration of rotor tilt and channel angle.

The lateral position response for an example configuration is show in figure 4.9. It shows the mean of 10 trials, along with one standard deviation either side of the mean, and the maximum range of values. The simulated dynamic response from equation (4.38) has been overlaid. The results for the complete array of configurations are shown in figure 4.14, with enlarged versions included in Appendix A. It was seen that low channel slope and rotor cant angles produced

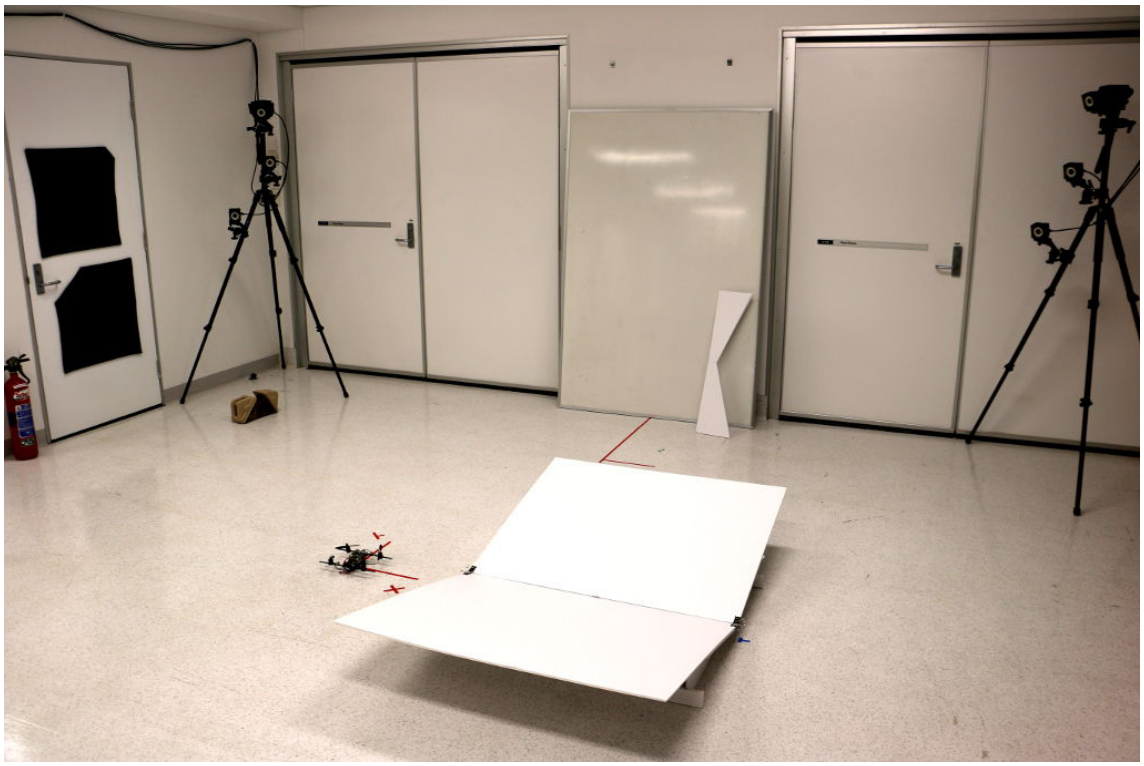

Figure 4.8: Experimental setup

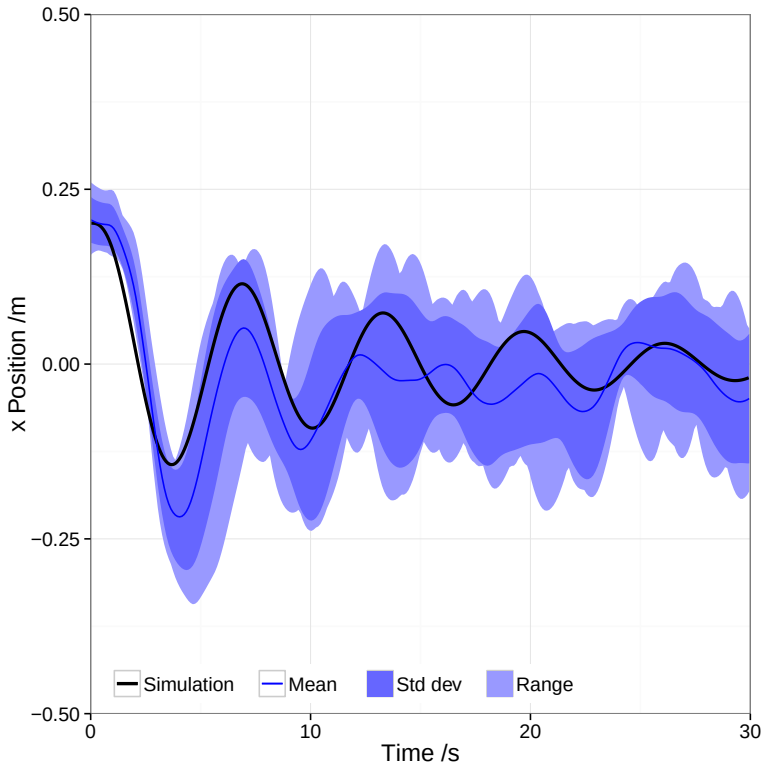

Figure 4.9: Lateral position response with 15° channel slope and 15° rotor cant, over 10 repetitions, and simulation

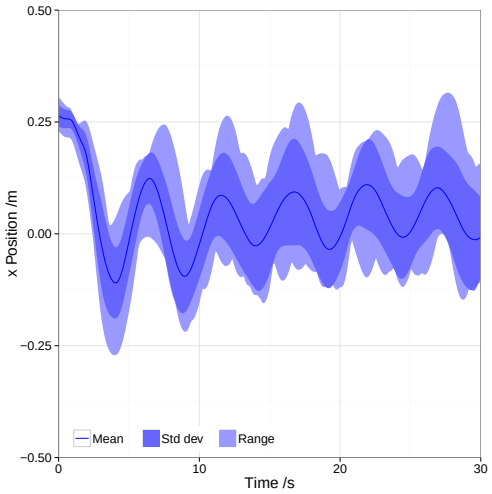

a. 10° rotor cant

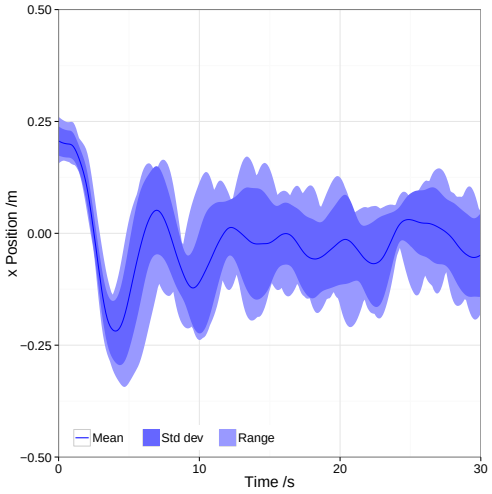

b. 15° rotor cant

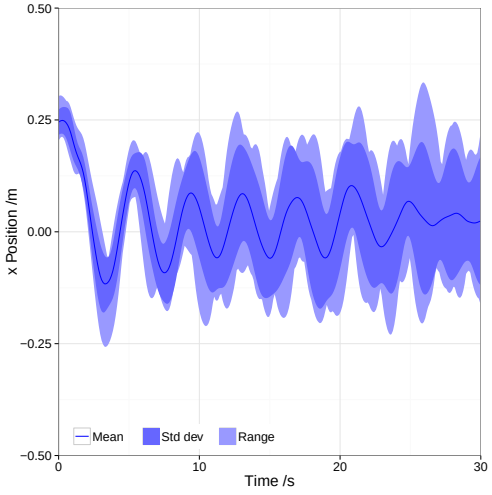

c. 20° rotor cant

Figure 4.10: Lateral position response with 15° channel slope and increasing rotor cant, over 10 repetitions

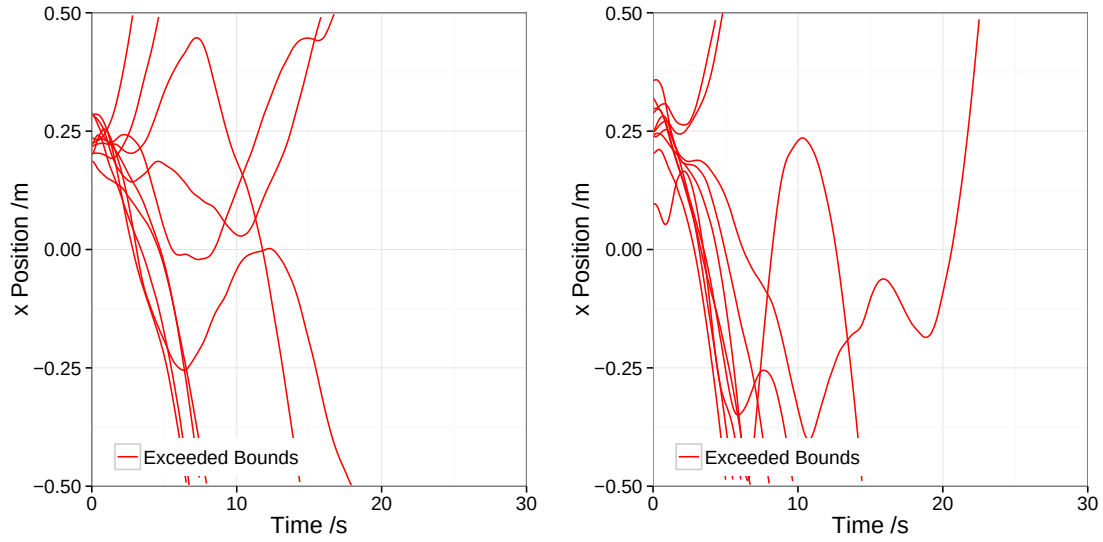

a. flat rotors b. 15° rotor cant

Figure 4.11: Lateral position response above flat ground, over 10 repetitions

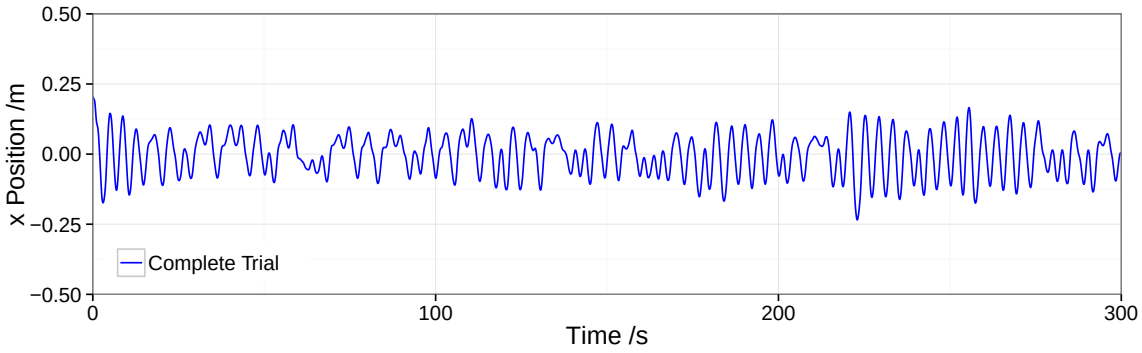

Figure 4.12: Extended duration lateral position response with 15° channel slope and 15° rotor cant

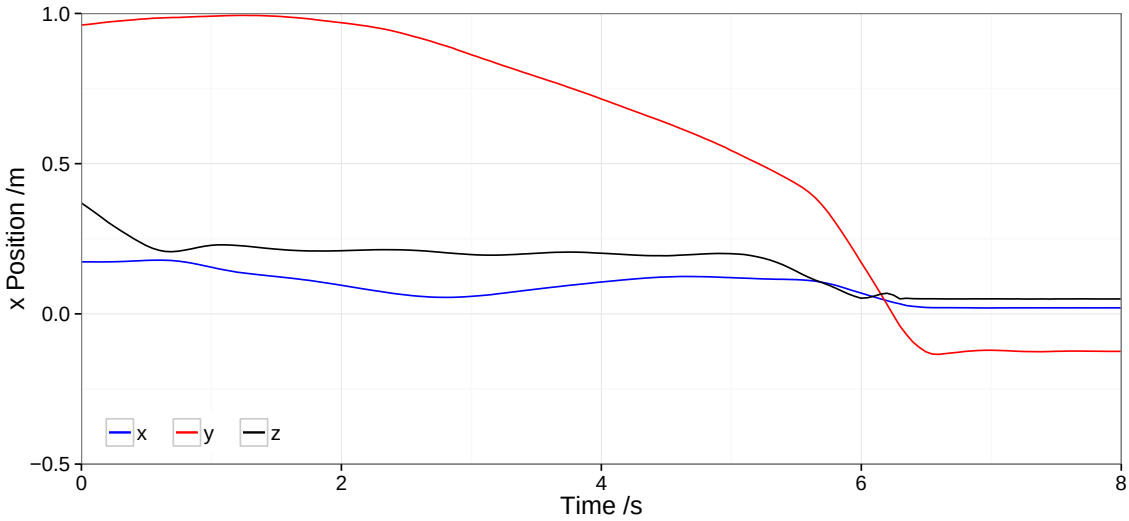

Figure 4.13: Passive landing position response with 3° channel tilt, 15° channel slope and 15° rotor cant, motors stopped at 6 s

unstable configurations. Channel slope and rotor cant increased stability of the system, up to an angle of 20° where constant oscillations were introduced.

A subset of experiments is shown figure 4.10 with mean and standard deviation plotted to more clearly show the effect of increasing rotor cant on system response — an initial increase damped oscillations and reduced steady state error, increasing further high frequency oscillations arose. For comparison the position instability of the system over flat ground with flat rotors and 15° rotor cant is shown in figure 4.11.

Long term stability was assessed by performing a single trial with an increased duration of 300 s as shown in figure 4.12.

To test the utility of ground interaction for assisting landing, we tilted the channel to direct the quadrotor towards a target landing point. The slope was angled 3° longitudinally, and longitudinal position control was turned off. Power to the motors was cut after 6 s. The position response of the quadrotor is shown in figure 4.13.

Flying a quadrotor with canted rotors in a sloped ground channel we have achieved passive lateral position stability. Stability was observed in 98.9 per cent of trials with a rotor cant and channel slope of 10° to 20°.

The full array of experimental results is shown in figure 4.14 with enlarged versions included in Appendix B. Each graph presents the lateral position response for a single configuration over 10 trials. In each graph complete trials and those which exceeded the bounds of the experimental setup are plotted separately.

The matrix of results, figure 4.14, exhibits two key trends; increasing rotor cant produces more damping of the system, and increasing channel slope leads to higher oscillation and faster response. From equation (4.36) we would expect increasing rotor cant to produce more lateral damping, and increasing channel slope to provide a greater lateral restoring force.

The damping trend can be seen more clearly in figure 4.10, where increasing the rotor cant from 10° to 15° decreases overshoot and steady state oscillations. Further increasing the rotor cant to 20° introduces an expected high frequency oscillation which we believe are due to unmodelled dynamics.

Of the configurations tested, the most effective arrangement was found to be a channel slope of 15° and rotor cant of 15° (see figure 4.14-o): it provided a consistently low overshoot, fast settling time and low long-term oscillation, which are favourable for the position control task.

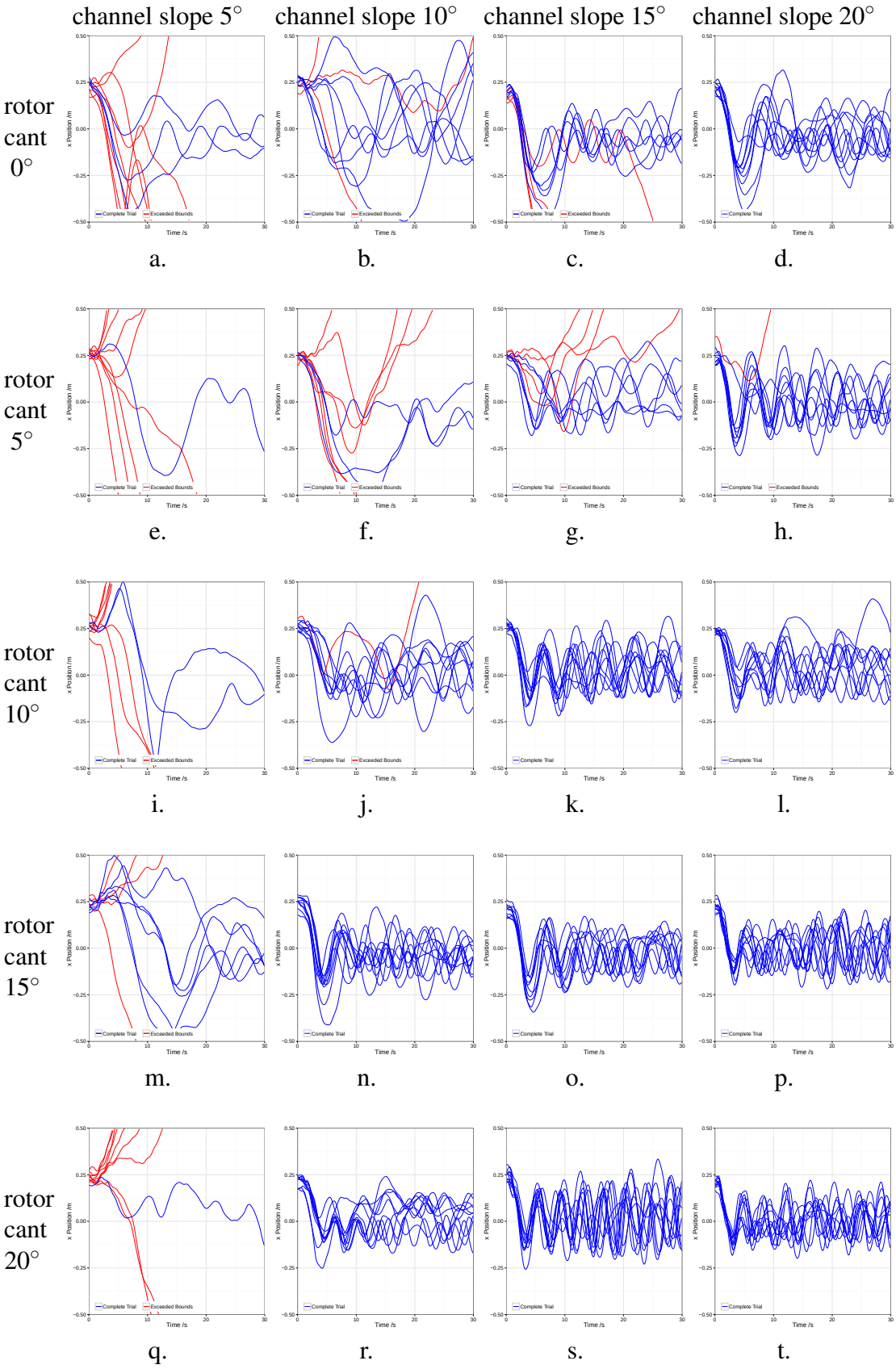

Figure 4.14: Array of experimental results showing lateral position response arranged by rotor cant angle vs channel slope angle

There is a strong correlation with the simulation result, which suggests that the model captures the principal system dynamics (see figure 4.9). Canting the rotors to 15° will result in a 3 per cent decrease in system efficiency when compared to flat rotors.

While it was expected that the 0° rotor cant configurations should be unstable, two of the configurations with high channel slopes demonstrated some stability (see figures 4.14-c and 4.14-d). It is believed that this is due to the influence of vertical-horizontal translation cross-coupling not accounted for in this analysis.

In some experiments, most notably figures 4.14-h and 4.14-j, the quadrotor was observed to slowly move up the side of the ground channel, in apparent opposition to the expected restoring force. While this effect has not been extensively studied it is believed that it is due to a cross coupling from pitch and z oscillations. The combination creates a "walking effect" causing the quadrotor to move up the side as it oscillates backward and forward.

The results in figure 4.11 comparing flat rotors to canted rotors over flat ground show that, although the system is expected to be dynamically neutral in position but stable in velocity, system bias and environmental disturbances mean that the system will not remain stationary even with canted rotors (see figure 4.11).

Use of passive position stability for controlling a quadrotor to a landing platform has been demonstrated in figure 4.13. This system was capable of guiding the craft from an initial position 1 m away and landing within 20 cm of the desired location. Extending the channel should allow for passive guidance from a more distant initial position.

4.6 Other Lateral Rotor Interaction Phenomena

Informal observations by numerous researchers have indicated that quadrotors tend to be attracted or repelled by walls depending on size, orientation and distance from the wall, ground or both. These effects are often counter-intuitive with repulsive effects transitioning to attractive effects without warning. By understanding these effects it is hoped that analytical models which capture the principal components can be developed. These effects could then be exploited to provide passive obstacle avoidance and trajectory following.

To examine the surface effects experimentally a single rotor was placed on a boom with pieces of cotton dangling below it as shown in figure 4.15. During the experiments the rotor

was moved closer and further away from the wall and ground in order to observe the changing airflow trajectories.

In the experiments, figure 4.15, it is difficult to see an effect from the wall alone. However there does appear to be some tapering inwards, likely due to the vena contrata — contraction of the flow after exiting the rotor.

With the introduction of a ground surface it is clear that there is increased recirculation around the tip of the rotor as the strings closest to the corner flick upwards. It is theorised that this recirculation has the effect of reducing the effective thrust that can be generated, as the preaccelerated air locally decreases the observed angle of attack. Decreased thrust on the side of the rotor nearest the wall causes the rotor to tilt towards the wall and, on a quadrotor, the whole aircraft to dip towards the wall. This is a positive feedback system that results in the aircraft rapidly contacting the wall.

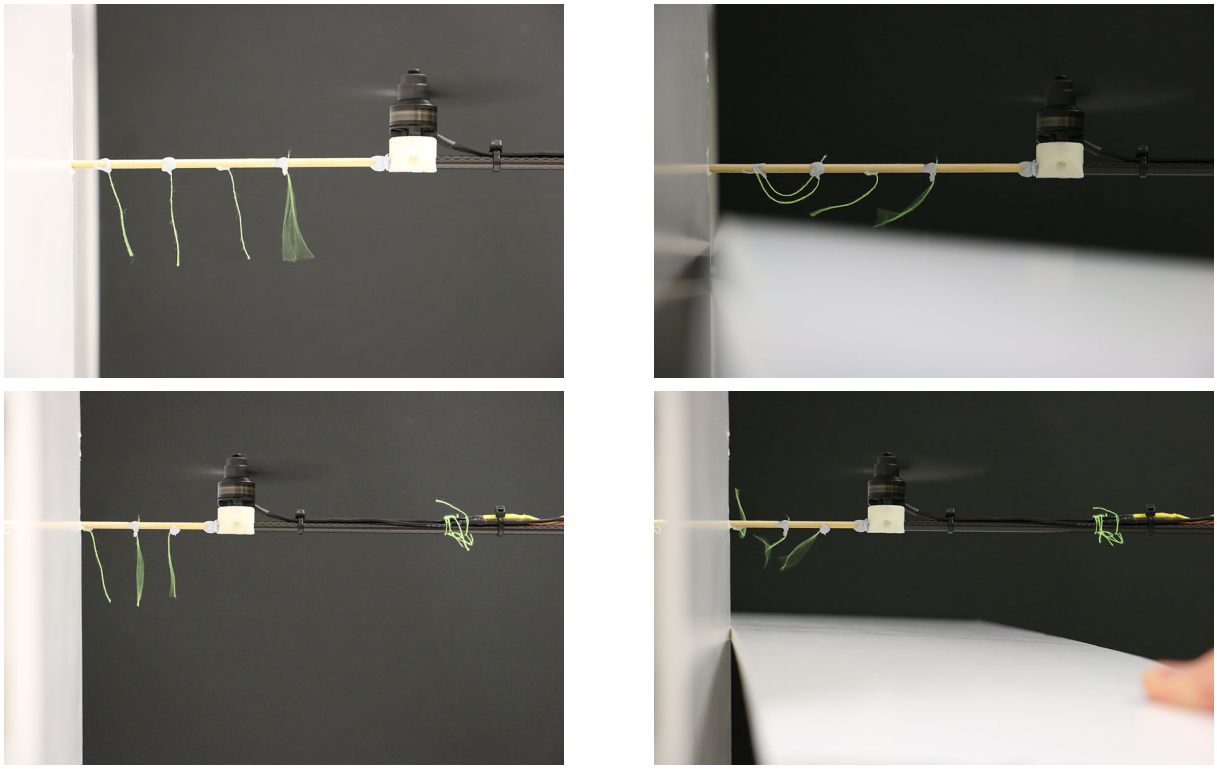

Figure 4.15: Wall and corner circulation effects shown without and then with a ground surface. Rotor tip is 1 (top) and 0.5 (bottom) rotor diameter from wall, without (left) and with (right) a ground surface.

Looking at the way the air moves through two isolated adjacent rotors on a quadrotor, we see that it acts much like batter moving through an eggbeater. That is, observed from above,

a lateral component of the air is sucked in between the rotors and ejected on the other side. Depending on their orientation on the quadrotor, this will serve to attract or repel the quadrotor from surfaces. To describe this phenomena we have coined the term “eggbeater effect”.

Combining the eggbeater effect with the recirculation effect leads to complex behaviour. At close proximity to the wall the recirculation effect seems to dominate. Moving further away, the eggbeater effect has stronger influence. This means in orientations where the eggbeater effect is ejecting air, the quadrotor will first be repelled from the wall and then if is moved closer it will be attracted to the wall, as our initial observations described.

Based on these investigations it seems that the effect is much more complicated than initially thought. Measuring rotor force accurately is a key stepping stone to understanding lateral rotor interactions. Therefore rotor instrumentation was pursued in the next phase of this work. However the strong results of the sensors developed, when used for velocity measurement, meant that this topic was not revisited in the duration of this thesis. It remains a topic for future work.

Chapter 5

Aerodynamic Force Measurements

Precision flight control of miniature robot aircraft requires an accurate model of vehicle dynamics and the forces acting upon it [Mellinger *et al*, 2012]. However, the principle source of force applied to a multirotor aircraft — its rotor — provides a variable amount of force depending upon the local aerodynamic conditions, proximity of objects and the manoeuvres of the aircraft. As a consequence, typical control approaches rely on very accurate and high-speed sensing of trajectory, using onboard MEMS IMUs and motion capture systems such as Vicon, to detect and correct for deviation induced by disturbances or by errors in the rotor actuation model. Unfortunately, low-cost accelerometers are not accurate enough for precision dead-reckoning and precision IR tracking tools are not effective outdoors due to insolation.

Other sensors are not able to fill the gap: GPS is slow and noisy, optical flow sensors do not function far from ground, and pitot tubes do not function well at low speeds. While barometers are generally effective for altitude measurement within ± 100 mm, there is currently no effective lateral velocity sensor.

An alternative approach is to focus on improving the dynamic model of the aircraft and estimate the internal states of the rotor, so as to improve trajectory tracking in the framework of less capable sensors. Bangura and Mahony use a sophisticated rotor model, combined with a motor power sensor and estimator to estimate the rotor force and lateral velocity [Bangura and Mahony, 2012] [Bangura and Mahony, 2014] [Bangura *et al*, 2015]. However, this requires access to the electronic speed controller internals, and high-speed processing.

My approach is to instead directly sense the force and transverse torques generated at the rotor, to feed into the dynamic model of the aircraft. In this way, irrespective of the local unsteady aerodynamic conditions of the rotor, the correct desired thrust may always be applied through a tight feedback control loop. By exploiting the known coupled mechanics between

Figure 5.1: Assembled force sensor front (left) and back (right).

rotorcraft translation and pitch velocity through induced drag and flapping, I construct a direct measurement of the thrust and speed of the aircraft.

5.1 Motor-Rotor Force Sensor

I developed a lightweight and low-cost motor force sensor capable of measuring rotor lift force and transverse rotor torques of a small Brushless DC (BLDC) rotor system. The design leverages the technique developed at Harvard for using low-cost MEMS barometers as tactile force sensors by encasing them in polyurethane rubber [Tenzer *et al*, 2014]. The Harvard, and later Right Hand Robotics "Takktile", sensors use Freescale MPL115A2 MEMS barometers which feature an opening in the case directly above the silicon sensing element which allows the strain field imparted by surface contacts to be partly transmitted to the MEMS sensing element. These sensor arrays can measure tactile contact forces with a sensitivity of 1 g. I build upon this technique by improving on the individual sensor element sensitivity and by using a small planar array of potted sensors as the elements of a miniature load cell with sufficient sensitivity to measure dynamic aerodynamic forces.

5.1.1 Construction

The force sensor is comprised of four sensors, a microcontroller and a data connector assembled on a Printed Circuit Board (PCB). Four threaded stand-offs are soldered to the PCB for securing the sensor to the quadrotor. An acrylic load plate is bonded to the top of the polyurethane

Table 5.1: Force Sensor Bill of Materials

Component	Quantity	Unit Cost	Total (AUD)
microcontroller, STM32F042G6U6	1	2.93	2.93
micro USB connector	1	0.63	0.63
PCB	1	5.30	5.30
resistors and capacitors	9	0.05	0.45
LED	1	0.12	0.12
pressure sensor, MS5611-01-BA03	4	7.71	30.84
3.3 V regulator, MIC55504-3.3YMT-TZ	1	0.21	0.21
stand offs, M2	4	1.01	4.04
rubber encapsulant, Vytaflex 20	3 mL	48.58/L	0.15
screws, M2x4	4	0.38	1.52
acrylic, 3mm	324mm^2	45.82/m^2	0.01
Grand Total			46.20

encased pressure sensors, retaining four captive screws for attaching the motor. The complete sensor is shown in figure 5.1. The completed sensor mass is 3 g.

It was found that the MPL115A2 sensors did not offer sufficient resolution for accurately measuring the small lateral forces imparted by the rotors during flight. Instead I use the Measurement Specialties MS5611, which offers two orders of magnitude improvement in resolution and nearly triple the maximum sampling frequency at up to 1.8 kHz.

During operation it was found that the sensors heat up, causing individual sensors to rapidly saturate. This was determined to be due to thermal expansion of the polyurethane rubber within the constrained volume of the stainless steel cap above the sensor element. To improve sensitivity the MS5611 sensors were decapped by mechanically removing the stainless steel case from the sensor substrate to directly expose the MEMS sensor die. It was also found that the strain field imparted by loading the rubber transducers under tension produced less motor vibration noise in sensor readings than compressive loading.

Total bill of materials (BOM) cost per sensor is approximately $50 in quantities of 10. The complete BOM is shown in table 5.1.

5.1.2 Casting Procedure

An effective method for moulding the Smooth-on Vytaflex 20 polyurethane over the sensors is to use a mould that was laser cut out of acrylic and screwed to PCB through the threaded stand-offs. A second piece of acrylic was used as a lid to cover the top of the sensor moulds

and pressed down to displace the excess polyurethane and produce moulded parts of uniform thickness with a smooth glass like top surface. A thin smear of petroleum jelly was applied to the acrylic mould parts to act as a release agent. This process is illustrated in figure 5.2.

5.1.3 Force Model

An arrangement of four pressure sensors in a square allows for independent measurement of the torques along each diagonal by taking the difference of two opposite sensor readings. The thrust produced by the motor can be computed by taking the sum of all four scaled sensor readings.

The force F_n on each sensor element approximated as a simple spring is given by:

$$F_n = k\bar{p}_n \tag{5.1}$$

where k is the sensor coefficient and $\bar{p}_n$ is the tared sensor reading under gauge load given by $\bar{p}_n = p_n - p_{n0}$.

The total vertical force F_z measured by the die sensor array is given by:

$$F_z = \sum F_n \tag{5.2}$$

$$F_z = k(\bar{p}_1 + \bar{p}_2 + \bar{p}_3 + \bar{p}_4) \tag{5.3}$$

The torques τ_x and τ_y measured by the motor force sensor are given by:

$$\tau_x = kd(\bar{p}_1 - \bar{p}_3) \tag{5.4}$$

$$\tau_y = kd(\bar{p}_2 - \bar{p}_4) \tag{5.5}$$

where d is the horizontal distance of the sensing elements from the central of the motor force sensor.

The sensor coefficient was determined by loading the sensor with a series of known masses and observing the resultant measurement. It was found to be $k = 3058$ units/N.

1. Assemble laser cut mould and apply release agent

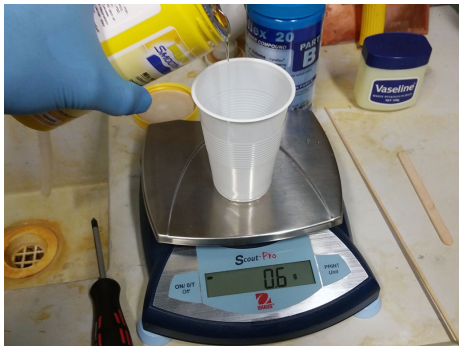

2. Mix 3 g of Vytaflex 20

3. De-gas in a vacuum chamber until bubbles stop

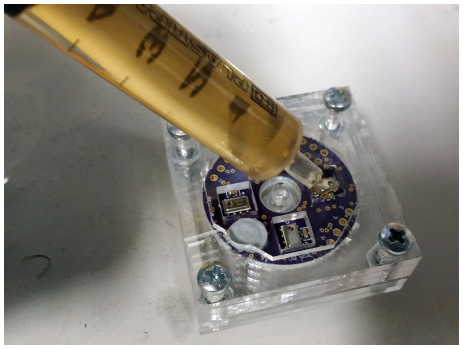

4. Fill sensor pockets

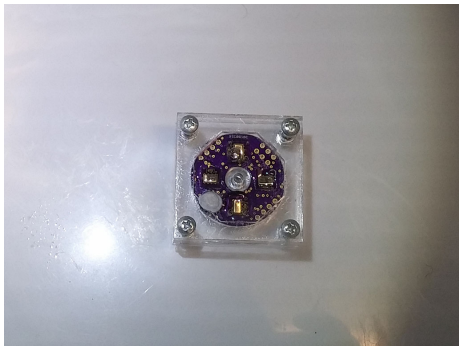

5. De-gas to evacuate air from sensors

6. Apply mixture to lid

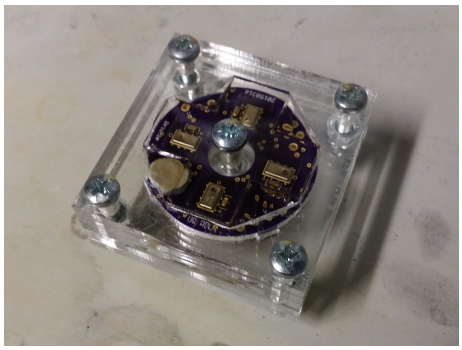

7. Slowly lower lid, avoid bubbles, replace if necessary

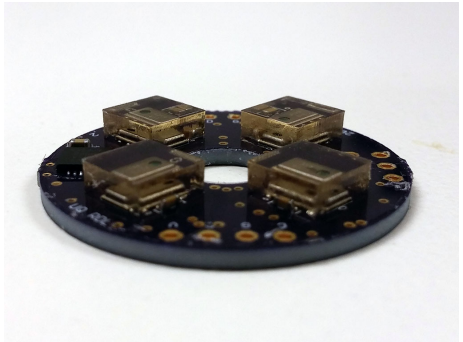

8. De-mould after 16 hours

Figure 5.2: Pressure sensor casting procedure

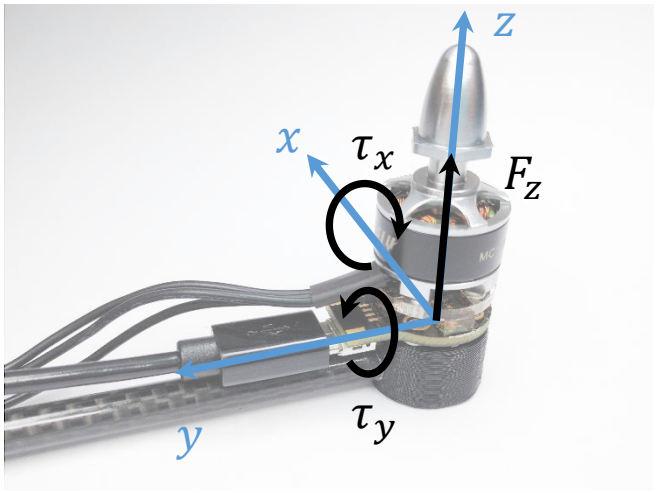

Figure 5.3: Mounted sensor with reference frame and vectors.

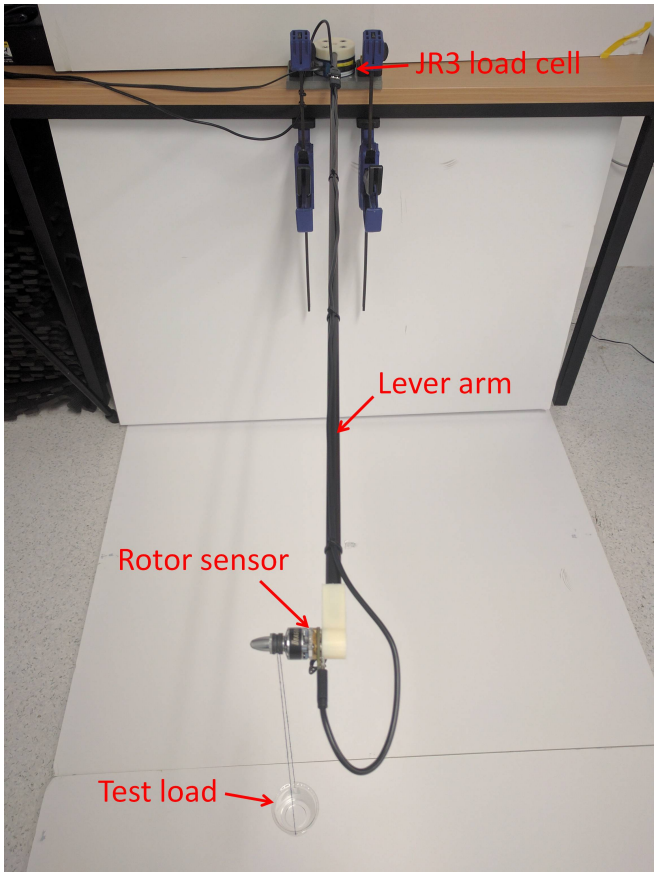

Figure 5.4: Static force sensor and JR3 load cell apparatus for torque comparison test.

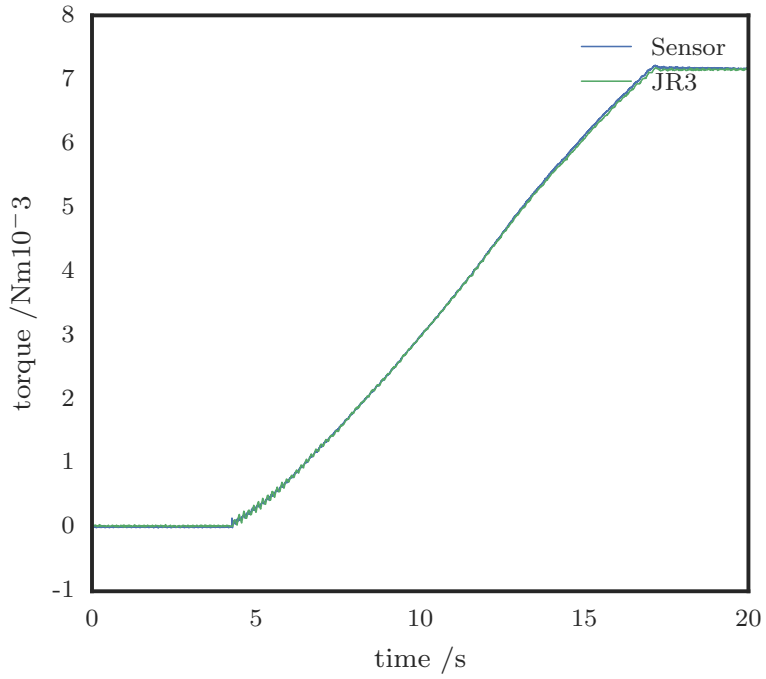

Figure 5.5: Unfiltered force sensor comparison with JR3 load cell.

5.1.4 Performance Comparison

To test the performance of the motor force sensor it was attached to a test rig as shown in figure 5.4 along with a $5000 JR3 force torque sensor for comparison. The JR3 6-DOF force torque sensor is attached the bench. Because the JR3 sensor is designed to measure much larger forces and has a lower resolution a force multiplying arm was used to improve sensitivity. The motor and sensor were attached to the end of this arm. In place of a rotor a pulley and suspended cup were attached to the motor shaft. A single point calibration of both the JR3 and motor force sensor were performed using a known mass and measuring the offsets from sensor centres. After taring the sensor readings a water bottle was used to gradually fill the cup while time stamped sensor measurements were recorded at 190 Hz for the JR3 and 1000 Hz for the force sensor. For comparison purposes the JR3 readings were scaled by the ratio of the lever arms, $1.01\ m/0.022\ m = 49.5$. The JR3 force torque sensor was filtered using a built-in 125 Hz low-pass filter. No filtering was applied to the motor force sensor. The comparison results are shown in figure 5.5.

The result show that the motor force sensor accurately tracks the torque as measured by the substantially more expensive JR3. There are some oscillations in the JR3 readings which are likely due to the experimental setup. As the cup is filled it begins to bounce around on the end

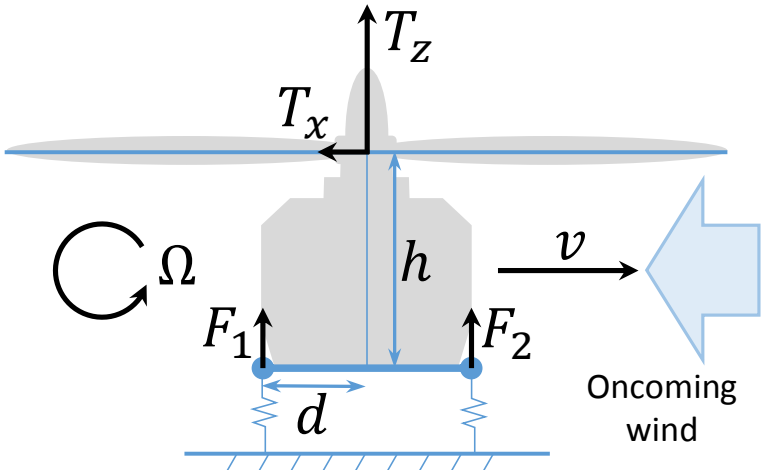

Figure 5.6: System free body diagram.

of the lever arm which bends and transmits the motion into the JR3 sensor at the base, the motor force sensor moves with the cup.

To test the capability of the sensor in its target application — measuring aerodynamic forces — I investigated using the sensor to measure the lateral velocity of a rotor. This serves as an ideal proof of concept as the signals generated by the aerodynamic effects are expected to be significant, the experiments are relatively straightforward to devise and it is easy to obtain velocity ground truth data for validation.

5.2 Velocity Torque Model

When a horizontal rotor translates sideways with some velocity, induced drag and blade flapping cause the rotor to apply a component of force against the direction of travel [Martin and Salaün, 2010] [Pounds *et al*, 2010]. The horizontal force subtends a torque about the vertical offset between the rotor plane and load plate which can be measured by the load cell.

The free body diagram of a simplified planar model comprised of two sensing elements is considered as shown in figure 5.6. The force sensors are compressible and allow small deflections under load.

We treat the action of blade flapping and induced drag as a lumped parameter effective force vector deflection given by [Pounds *et al*, 2010]:

$$T_x = T(q_1\dot{x} - q_2\dot{\theta}) \tag{5.6}$$

where q_1 and q_2 are the lumped translational and pitch velocity coefficients, $\dot{x}$ is the longitudinal velocity of the rotor and $\dot{\theta}$ is the pitch velocity.

In dynamic maneuvers, this value may be measured by a precision gyro and cancelled; in quasi static hovering flight, $\dot{\theta} \approx 0$. The component of thrust directed into the horizontal by induced drag and blade flapping is therefore given by:

$$T_x = (F_1 + F_2) q_1 \dot{x} \tag{5.7}$$

Under load the motor rotor system will tilt to some static equilibrium in which the torques around the centre of rotation will be equal:

$$T q_1 \dot{x} h = d \Delta F \tag{5.8}$$

$$\dot{x} = \frac{d}{q_1 h} \frac{\Delta F}{T} \tag{5.9}$$

$$\dot{x} = \frac{d}{q_1 h} \frac{F_1 - F_2}{F_1 + F_2} \tag{5.10}$$

where h is the height of the rotor aerodynamic centre above the elastic centre of rotation, d is the horizontal distance of the sensor element from the centre of rotation, ΔF is the sensor element force differential, F_1 and F_2 are the individual sensor element forces.

Using this relation, the sensor measurements may be used to compute an estimate of $\dot{x}$. Parameters for a prototype sensor rotor–motor testbed are given in Table 5.2.

5.3 Single Rotor Lateral Velocity Sensing

A series of experiments were carried out to characterise the rotor-motor-sensor system and determine the effectiveness of the force sensor in measuring the lateral velocity of a rotor. Basic testing to demonstrate the function of the force measurement elements was trivial, and is not included here.

Table 5.2: Sensor, Motor and Rotor Parameters.

d	sensor offset	0.0045	m
h	rotor height offset	0.02	m
k	sensor coefficient	3058	units/N
q_1	rotor coefficient	0.138	

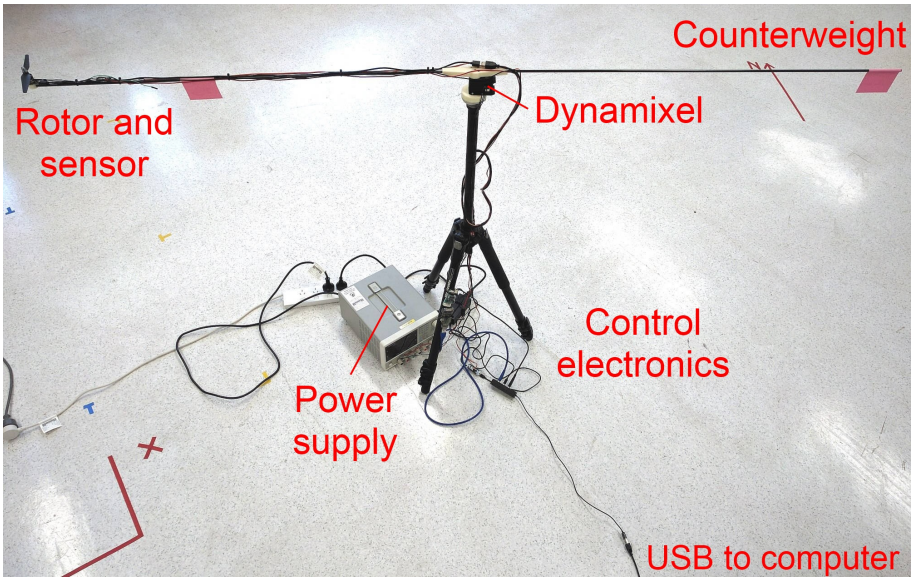

Figure 5.7: Swing-arm apparatus.

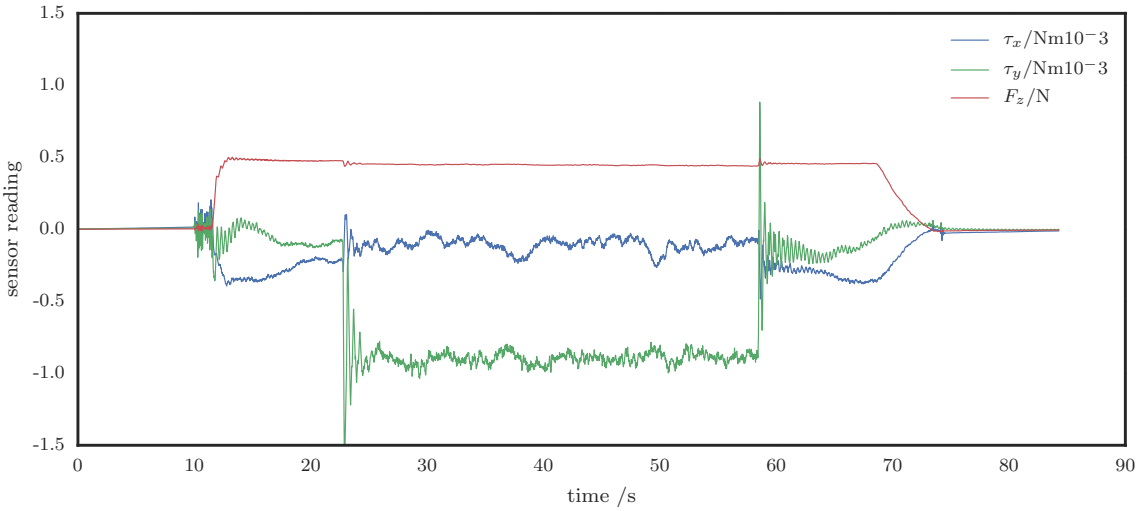

Figure 5.8: Exemplar sensor measurement, $\dot{x} = -0.53$ ms^{-1}.

The validation of the lateral sensing function required accurate replication of steady, constant-velocity motion. We constructed a long swing-arm mechanism to move a rotor through a circular arc, approximating linear motion. The arm is a 1 m long, 6 mm diameter woven carbon fibre tube, attached to a Dynamixel MX64 motor mounted to a tripod. The motor is a Dragonfly MC1306 3100 KV motor, with a T-Motor 6.5x3.5" rotor, driven by a Dys XM10A ESC powered by a 8.4 V bench supply. The motor is secured to the tube with a 3D printed mount.

The force sensor, ESC and Dynamixel were connected to a computer via USB for control and data capture. The complete experimental apparatus is shown in figure 5.7.

During each experiment, the sensor force and torque data was recorded at 1000 Hz starting with 10 s when the rotor and platform were stationary. The applied motor voltage was then gradually increased to 30 per cent, approximately hover thrust for a 200 g quadrotor. After 10 s of settling time, the platform started to rotate at the specified rate until it completed three revolutions, whereupon it halted. A further 10 s of data was captured with the platform stationary and the rotor still spinning before the rotor was brought to a stop. A final 10 s of sensor data was recorded before the experiment was concluded.

An exemplar test of the sensor moving with a tangential velocity of -0.53 ms^{-1} is shown in figure 5.8.

Four translation sensing experiments were undertaken: a control test with the rotor stationary, rotation of the swing-arm clockwise and counter-clockwise, operation of the sensor with and without air conditioning active, and a set of tests to establish the linearity of the sensor.

5.3.1 Sensing with Clockwise and Counter-Clockwise Arm Rotation

To determine the effect of platform rotation direction on the sensor measurements, two tests were conducted with the swing-arm rotating first counter-clockwise and then clockwise — see figures 5.9a and 5.9b. When rotating counter-clockwise, the torque τ_y was positive; when rotating clockwise at the same speed it was of similar magnitude and negative, as expected. The tangential velocity of the rotor during each test was -0.66 ms^{-1} and 0.66 ms^{-1} for counter-clockwise and clockwise swings, respectively.

Contrary to expectations, F_z was observed to increase slightly during counter-clockwise swing-arm rotation, but decrease in clockwise rotation — a total change of less than 5 per cent. A 10 Hz filter was applied to the sensor data to make this offset more apparent. The differences

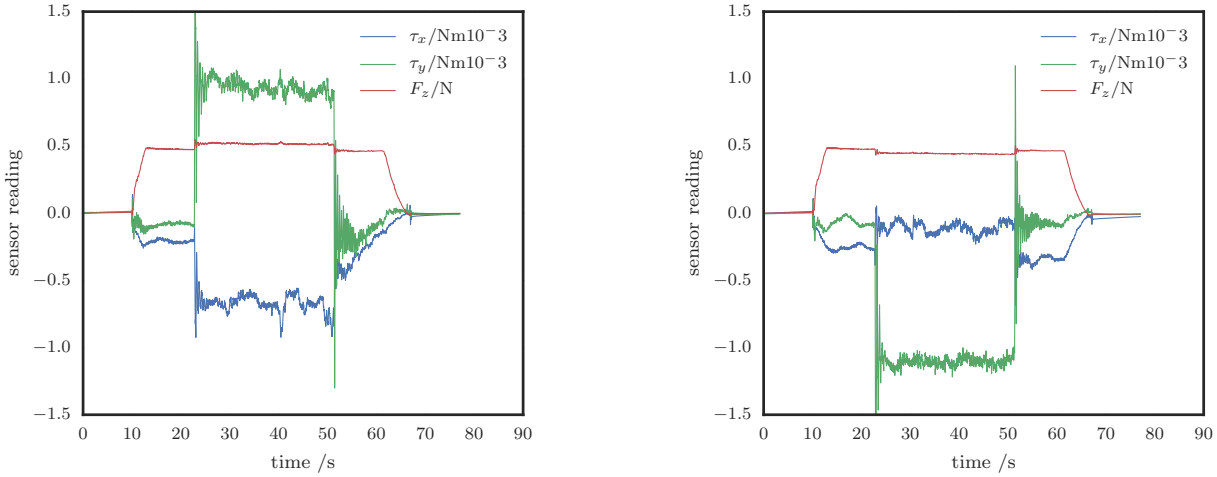

Figure 5.9: Thrust and moment forces for motion in both rotation directions of the platform, CCW (left) and CW (right), $\dot{x} = \pm 0.66$ ms^{-1} with a 10 Hz low pass filter applied.

are likely caused by the rotor disc moving along an arc, the inner most region of the rotor disc moves more slowly through the air than the outer most region. In the CCW case the outer most region is proceeding this results in a net thrust increase. In the CW case with the outermost region receding there will be a net thrust decrease.

The source of this difference could be verified by conducting additional experiments with the rotor spinning in the opposite direction and again observing the thrust change for clockwise and counter-clockwise swing-arm rotation.

5.3.2 Sensor with Rotor Stationary

To determine the influence of the platform motion on the force sensor readings, an experiment was conducted without the rotor spinning. This removes the influence of aerodynamic effects, leaving only forces induced by the apparatus, as shown in figure 5.10. The tangential velocity of the rotor was -0.66 ms^{-1}.

This shows the coupling of the platform arm movement into the sensor readings — in particular the high-frequency transients at the beginning and end of motion. This is believed to be due to torsional oscillation of the high-mounted motor weight about the axis of the tube, excited by the step change in Dynamixel velocity.

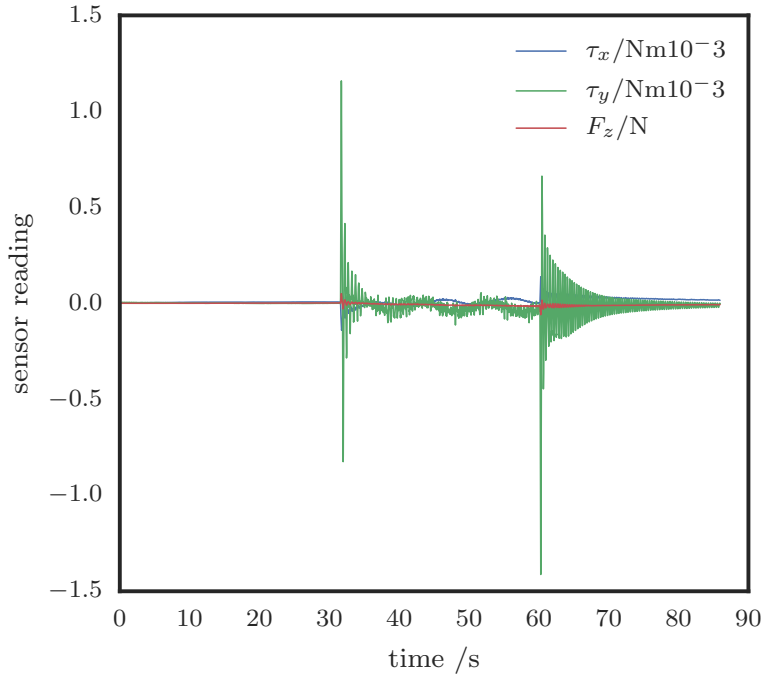

Figure 5.10: Sensor measurements during an experiment without the rotor spinning, $\dot{x} = -0.66$ ms^{-1}.

5.3.3 Effect of Ambient Air Disturbances on Sensor

During initial function testing of the sensor, it was noticed that the measured rotor forces were substantially more variable and noisy than expected. I realised that the sensor is sufficiently sensitive to detect the transient aerodynamic disturbance patterns in the room induced by the laboratory air conditioning.

Experiments were conducted with and without air conditioning on (see figure 5.11). The tangential velocity of the rotor during each arm swing was -0.53 ms^{-1}. It was found that air conditioning increased the cyclic measurement deviation in tests by a factor of $\sim$5 — the three oscillations in the torque measurements roughly correspond to the three revolutions of the swing-arm, and indicate that the observed variation is linked to a global ambient flow field.

To reduce the effect of these disturbances during characterisation experiments, the air conditioning was turned off for all other tests.

5.3.4 Velocity Sensor Linearity

To determine the linearity of the sensor for velocity estimation, an array of trials were conducted with the swing-arm set with incrementally increasing speed. This was achieved by varying the

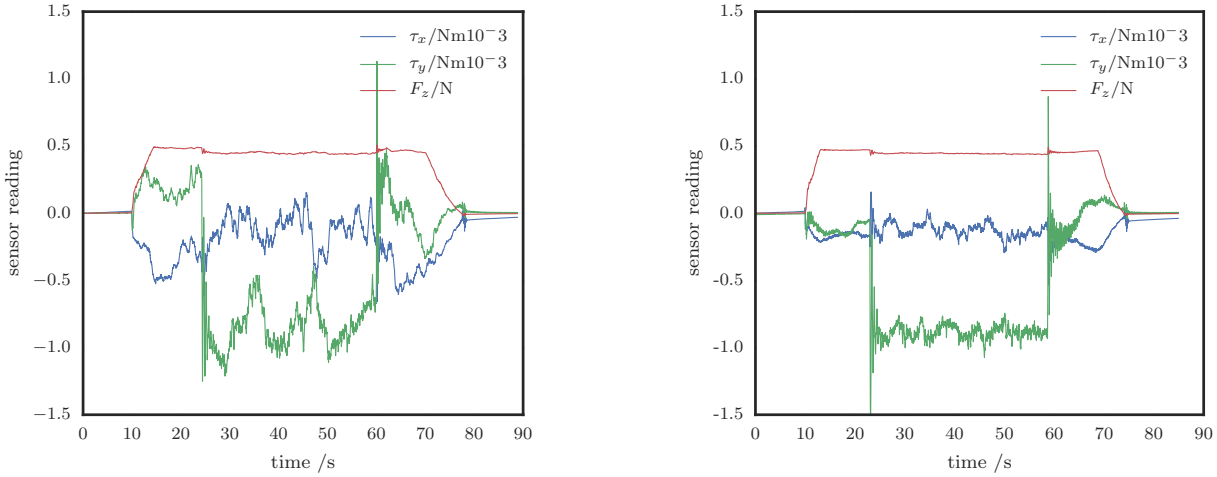

Figure 5.11: Thrust and moment forces with (left) and without (right) the AC turned on, both with $\dot{x} = -0.53$ ms^{-1}.

Dynamixel "moving speed" parameter from 20 to 60 units in increments of 5 units. The rotor was spinning at a constant speed near hover thrust for a 200 g micro quadrotor, providing 50 g of force. The torque measured around the radius of the platform arm, τ_y, was averaged during the middle revolution of platform and plotted against the tangential velocity of the platform in figure 5.12. The plot shows a strong linear trend for the range of velocities tested (R = 0.995), and demonstrates the effectiveness of the force sensor in measuring the lateral velocity of a rotor.

5.3.5 Observations

The sensor performed well during testing, demonstrating sufficient sensitivity to capture unintended phenomena, such as the swing-arm resonance and ambient AC flow fields. Compensating for these effects will form some of the future work of the project.

The mechanical coupling of the motor and flexible swing-arm tubes is not expected to pose a problem for applications on a micro UAV. The arms of a typical quadrotor are substantially shorter and stiffer than the shaft used. Furthermore, these types of coupled motions, and those due to pitch and roll motions in particular, can be compensated for when the sensor is combined with angular velocity measurements from the IMU.

It is observed that the projected intercept of the graph is not precisely zero. This is thought to be due to small offsets in the torque values that arise once the rotor is spinning. This is likely due to the sensor construction and slight rotor-sensor axial misalignment. A second calibration

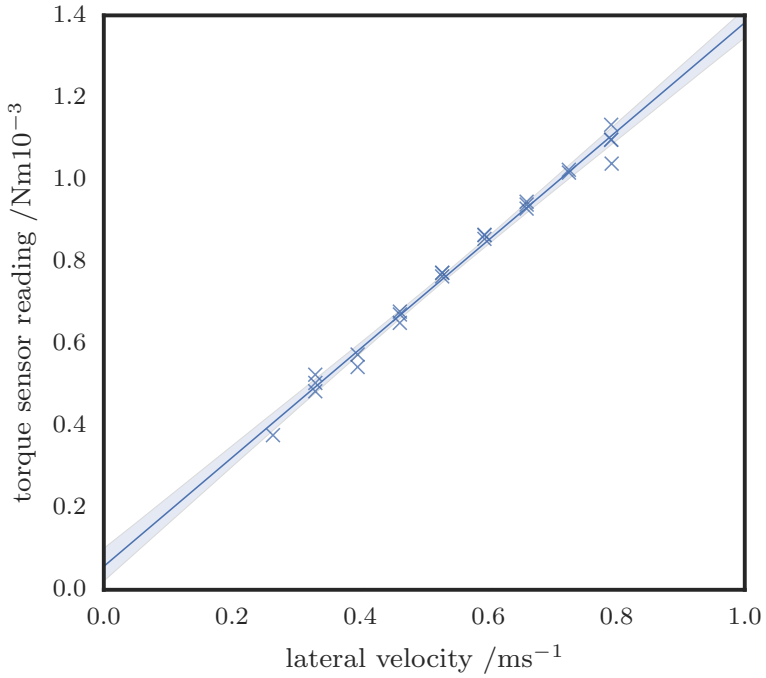

Figure 5.12: Torque sensor reading for varying lateral velocity of the rotor.

phase with a spinning rotor should be able to compensate for this.

5.4 Quadrotor Translation Velocity Sensing

Expanding on the results obtained for lateral velocity estimation on the single rotor testbed we consider the case of a quadrotor with force sensors on each rotor and expand the planar model into a 6-DoF model of the system.

The forces and velocities of a quadrotor measured onboard will naturally be expressed in the body-fixed frame, $\mathcal{A} = \{\mathbf{e}_1, \mathbf{e}_2, \mathbf{e}_3\}$ where $\mathbf{e}_1$ is aligned with the front of the craft. Vector $\mathbf{v}$ is the translational velocity of frame $\mathcal{A}$ and Ω is angular velocity of frame $\mathcal{A}$, relative to the inertial frame, expressed in $\mathcal{A}$.

5.4.1 Single Rotor Forces and Torques

When a rotor translates perpendicular to its axis of rotation, unbalanced aerodynamic forces due to blade flapping and induced drag give rise to horizontal components of thrust opposing the direction of motion [Pounds *et al*, 2010, Martin and Salaün, 2010]. When a quadrotor pitches or rolls, the instantaneous gyroscopic stability of its rotors causes them to lag behind the motion

of the airframe. This produces effective blade flapping that results in a local transverse thrust component in the body-fixed frame.

Combining these effects produces a 6-DOF single rotor force model for multirotors [Pounds and Dollar, 2014]:

$$\mathbf{T} = -k\omega^2\Big(I - (Q_1\mathbf{v}_\times\mathbf{e}_3)_\times - (Q_2\Omega)_\times\Big)\mathbf{e}_3 \tag{5.11}$$

where $\mathbf{T}$ is the rotor force, k is a rotor thrust constant, ω is the rotor velocity, I is the 3×3 identity matrix, $\mathbf{v}$ and Ω are the aircraft body-fixed translational and rotational velocities respectively. Matrices Q_1 and Q_2 are:

$$Q_1 = q_1(\mathbf{e}_1 \;\; \mathbf{e}_2 \;\; 0) \tag{5.12}$$

$$Q_2 = q_2(\mathbf{e}_1 \;\; \mathbf{e}_2 \;\; 0) + \frac{1}{\omega}(\mathbf{e}_2 \;\; \mathbf{e}_1 \;\; 0) \tag{5.13}$$

for q_1 and q_2, constant translation and rotation lateral force parameters of the rotor, respectively. Here $\times$ is the skew-symmetric matrix operator.

Conversely, when a rotor translates axially, the changing local angle of attack of air passing over the rotor blades results in an increase or decrease in thrust, opposing the direction of motion (known as rotor inflow damping) [Pounds *et al*, 2010]:

$$\mathbf{T}\cdot\mathbf{e}_3 = -k\omega^2(1 - c_z\mathbf{v}\cdot\mathbf{e}_3) \tag{5.14}$$

where c_z is a damping constant given by:

$$c_z = \frac{1}{\alpha\omega R} \tag{5.15}$$

where α is the geometric rotor angle of attack and R is the rotor radius.

Thus, the 3-DOF translational velocities and roll and pitch rotational velocities produce forces measurable at the rotor head. For a single rotor, pitch- and roll-induced forces are indistinguishable from translation-induced forces.

5.4.2 Collective Rotor Motion

The multiple rotors of a quadrotor provide additional mechanics that can be used for velocity estimation. The displacement between a quadrotor's rotors and its centre of mass result in coupled translations of the rotors due to roll, pitch and yaw velocities. Equation (5.11) can be expanded to give the change in measured thrust due to motion:

$$\Delta \mathbf{T}_i = -k\omega^2 \left[-K_1 \mathbf{v} - K_{2i}\Omega\right] \tag{5.16}$$

where $\mathbf{T}_i$ is the thrust of the ith rotor, and K_1 and K_{2i} are augmented coupling matrices for the ith rotor:

$$K_1 = Q_1 + \begin{pmatrix} \mathbf{0} & \mathbf{0} & c_z \mathbf{e}_3 \end{pmatrix} \tag{5.17}$$

$$K_{2i} = (K_1 \mathbf{d}_{i\times} - Q_2) \tag{5.18}$$

where $\mathbf{d}_i$ is the rotor offset from the centre of mass.

The mapping between motions and thrust outputs can thus be written for the whole aircraft:

$$\begin{bmatrix} \Delta \mathbf{T}_1 \\ \Delta \mathbf{T}_2 \\ \Delta \mathbf{T}_3 \\ \Delta \mathbf{T}_4 \end{bmatrix} = \begin{bmatrix} K_1 & K_{21} \\ K_1 & K_{22} \\ K_1 & K_{23} \\ K_1 & K_{24} \end{bmatrix} \begin{bmatrix} \mathbf{v} \\ \Omega \end{bmatrix} \tag{5.19}$$

where the combined 12×6 coupling mapping matrix is denoted P. By exploiting this coupling, the full 6-DOF velocity vector of the aircraft may be recovered. For a conventional '+'-shaped quadrotor with four rotors of approximately equal rotor speed, spaced equal distance d from and h above the centre of mass, P is:

$$P = \begin{bmatrix} q_1 & 0 & 0 & -q_2 & q_1h - 1/\omega & 0 \\ 0 & q_1 & 0 & -q_1h - 1/\omega & -q_1 & q_1d \\ 0 & 0 & c_z & 0 & -c_zd & 0 \\ q_1 & 0 & 0 & -q_2 & q_1h - 1/\omega & -q_1d \\ 0 & q_1 & 0 & -q_1h - 1/\omega & -q_1 & 0 \\ 0 & 0 & c_z & c_zd & 0 & 0 \\ q_1 & 0 & 0 & -q_2 & q_1h - 1/\omega & 0 \\ 0 & q_1 & 0 & -q_1h - 1/\omega & -q_1 & -q_1d \\ 0 & 0 & c_z & 0 & c_zd & 0 \\ q_1 & 0 & 0 & -q_2 & q_1h - 1/\omega & q_1d \\ 0 & q_1 & 0 & -q_1h - 1/\omega & -q_1 & 0 \\ 0 & 0 & c_z & -c_zd & 0 & 0 \end{bmatrix} \tag{5.20}$$

For non-zero values of d and ω, P is rank 6, and its left inverse may be readily computed such that:

$$\begin{bmatrix} \mathbf{v} \\ \Omega \end{bmatrix} = (P)^{-1} \begin{bmatrix} \Delta\mathbf{T}_1 \\ \Delta\mathbf{T}_2 \\ \Delta\mathbf{T}_3 \\ \Delta\mathbf{T}_4 \end{bmatrix} \tag{5.21}$$

where the inverse mapping of the rotor velocity-induced forces is given by:

$$\begin{bmatrix} \frac{1}{4q_1} & 0 & -\frac{1}{2c_zdq_1\omega} & \frac{1}{4q_1} & 0 & \frac{q_2}{2c_zdq_1} & \frac{1}{4q_1} & 0 & \frac{1}{2c_zdq_1\omega} & \frac{1}{4q_1} & 0 & -\frac{q_2}{2c_zdq_1} \\ 0 & \frac{1}{4q_1} & -\frac{1}{2c_zd} & 0 & \frac{1}{4q_1} & \frac{1}{2c_zdq_1\omega} & 0 & \frac{1}{4q_1} & \frac{1}{2c_zd} & 0 & \frac{1}{4q_1} & -\frac{1}{2c_zdq_1\omega} \\ 0 & 0 & \frac{1}{2c_zdq_1\omega} & 0 & 0 & \frac{1}{2c_zdq_1\omega} & 0 & 0 & \frac{1}{2c_zdq_1\omega} & 0 & 0 & \frac{1}{2c_zdq_1\omega} \\ 0 & 0 & 0 & 0 & 0 & \frac{1}{2c_zd} & 0 & 0 & 0 & 0 & 0 & -\frac{1}{2c_zd} \\ 0 & 0 & -\frac{1}{2c_zd} & 0 & 0 & 0 & 0 & 0 & \frac{1}{2c_zd} & 0 & 0 & 0 \\ 0 & \frac{1}{4dq_1} & 0 & -\frac{1}{4dq_1} & 0 & 0 & 0 & -\frac{1}{4dq_1} & 0 & \frac{1}{4dq_1} & 0 & 0 \end{bmatrix} \tag{5.22}$$

Note that the lateral velocity components are effectively the mean lateral force, scaled by $1/q_1$, as the other contributing components are very small. As a consequence, however, the vertical velocity and rotational velocities sensitivities are also expected be small, which results in less sensitive tracking. As the IMU gyros of the aircraft also provide useful estimates of

velocities, so these could additionally be fused with the force-derived estimates to augment the measurement.

Due to the symmetric nature of the quadrotor, forces measured by opposing rotors due to rotational velocities tend to cancel out while forces due to lateral velocities add.

5.4.3 Flight Experiments

A series of experiments were carried out to evaluate the performance of the sensors in estimating velocity in x, y and z. In each experiment, the aircraft was trimmed then commanded to follow a pre-generated waypoint trajectory with a position controller running at 240 Hz. A final stationary hover was carried out before landing and shutting off the motors.

The trajectories flown were:

- Stationary hover (figures B.1–B.4)
- Y-axis velocity step (figures B.5–B.8)
- Y-axis sinusoidal velocity (figures B.9–B.12)
- Z-axis sinusoidal velocity (figures B.13–B.16)
- Square in XY (figures B.17–B.20)
- Circle in XY (figures B.21–B.24)
- Double circle in XY (figures B.25–B.28)

During each experiment, aircraft pose was logged at 240 Hz using an Optitrack system and differentiated to obtain velocity ground truth. The readings from each of the four sensors were logged at 1 kHz, and a 10 Hz cut-off filter was applied to the sensor readings. A 10 Hz cut-off frequency was chosen as it is on the same order of magnitude as the velocity dynamics of the aircraft. The resultant velocity estimates were then calculated.

The first 10 s of each experiment is the takeoff maneuver and the final 5 s is the landing. Sudden contact with the ground results in a large spike in the velocities followed by high frequency oscillations which damp out until the aircraft comes to rest. Fixed sensor calibration offsets and linear scaling factors were determined from the circular trajectory, figures 5.13–5.15, and applied to all other results. Every tenth measured y reference velocities and their

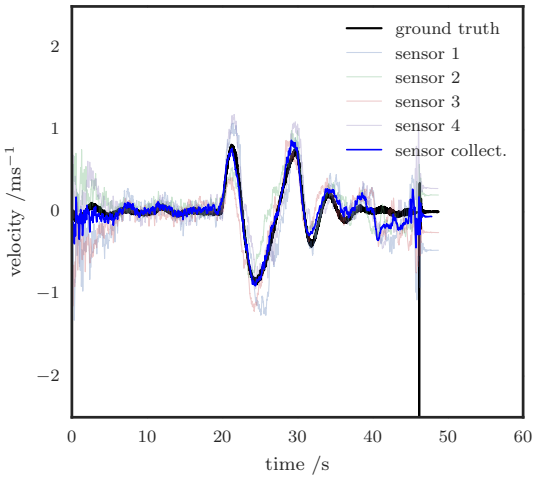

Figure 5.13: Circular path *dx* measurements.

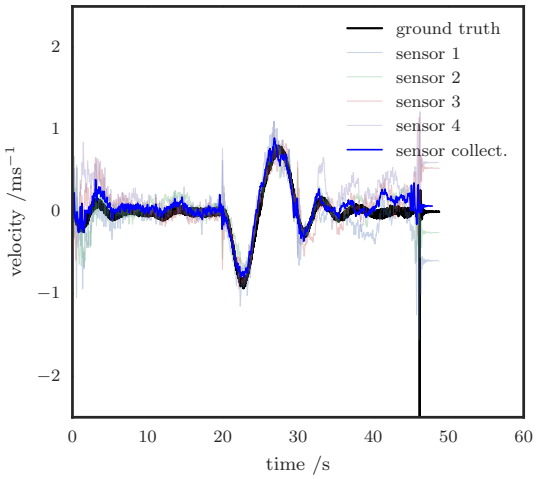

Figure 5.14: Circular path *dy* measurements.

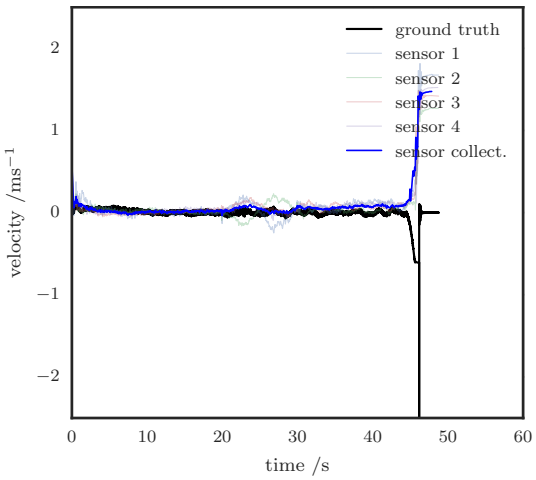

Figure 5.15: Circular path *dz* measurements.

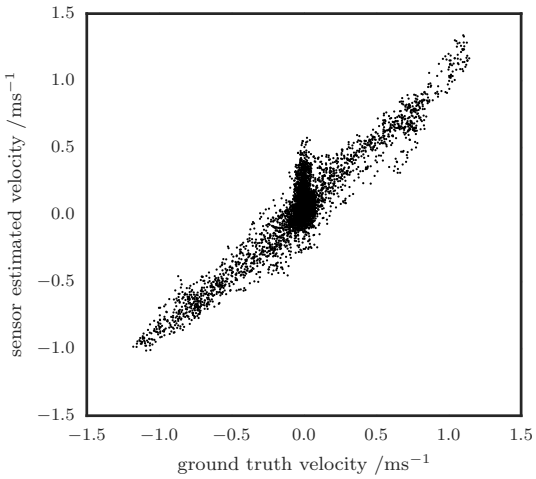

Figure 5.16: *dy* linearity plot — estimated vs reference velocities for every tenth point from all experiments.

respective estimated values are given in figure 5.16, showing the linearity of the sensors over all experiments. A y velocity linearity plot was also computed for each trajectory.

The results show a strong relation between the estimated lateral translation and the ground-truth optical tracking measurement. The aggregate estimates from the force sensors under each rotor (numbered 1 to 4) tracked the motions of the aircraft with good stability, and performed best when there was a substantial velocity signal. The linearity of the sensors is strong, although the sensors were less effective at very low velocities, such as around hover. The error was approximately zero mean over the course of the experiments.

From the velocity during stationary hover, it can be seen that immediately after hover the estimated velocity is close to the ground truth. After 25 s the estimate correlation degrades, moving as much as 0.5 ms^{-1} away from the ground truth. We expect that this behaviour is due to the aircraft taking off into neutral air recirculation conditions. As the hover progresses recirculation leads to the formation of cells around the aircraft. This is a well understood phenomena in the study of helicopter aerodynamics. The interactions of these cells with the aircraft leads to actual forces on the rotors which are detected by the force sensors. While they cause a degraded velocity estimate the measurement of these forces could be used to improve disturbance rejection, leading to more stable flight.

In contrast, the vertical velocity estimate did not exhibit any noticeable signal. While we anticipated a lower sensitivity in this axis, the lack of signal was surprising. This might be due to the rotors employed on the aircraft having relatively small (and thus high-disc loading) rotors which would produce a very low c_z value, such that the amount of inflow damping experienced by the aircraft is minimal. Redesigning the aircraft to have larger rotors with a slower wake velocity would increase the proportional influence of inflow damping and provide more signal.

It should be noted that the sensor calibration scalings were set only once at the beginning of the experiments, and no adaptive filtering has been employed. With additional filtering and bias correction from extrinsic sensors, we believe that these sensors will offer even greater performance over their current capabilities.

The introduction of slight compliance through the rubber composition of the rotor force sensor presents the possibility of the system acting as a damper. The combination of rubber used and motor mass leads to a natural frequency of 51.6 Hz. This is ideal as it is below the rotational speed of the rotor yet above the frequency of typical maneuvers carried out by the

quadrotor, resulting in a filtered signal without resonance.

The noise in the lateral velocity estimate is approximately ± 0.1 ms^{-1}. In comparison a state of the art IMU based lateral velocity estimate has a noise of approximately ± 0.5 ms^{-1}, however this is without a 10 Hz cut-off filter [Allibert *et al*, 2016]. When combined with the non linear observer proposed by Allibert *et al* they were able to achieve velocity estimates with much lower noise, however they still varied from ground truth by up to 0.5 ms^{-1} in parts especially during large changes in velocity [Allibert *et al*, 2016]. This is in contrast to our velocity estimate which performs best when there are changes in velocity and the quadrotor is not stationary. This difference could allow the two estimates to be combined to achieve an improved velocity estimate during both stationary hover and lateral motion.

5.4.4 Control Experiments

I carried out experiments to verify that the sensors functioned correctly under feedback control for a variety of representative trajectories. During each experiment, aircraft pose was logged at 240 Hz using an Optitrack system and differentiated to obtain velocity ground truth. The values of each of the four sensors were polled at 1 kHz, and a Savitzky-Golay filter was applied to the readings. The resultant velocity estimates were then calculated and passed on to the flight controller. The proportional velocity feedback controller had unity gain for all tests. For each test, fixed sensor offsets and linear scaling factors were determined from a calibration flight, and applied to all results.

The first 2.5 s of each experiment is the takeoff maneuver, carried out under PID position control using Optitrack measurements. The middle section consists of a velocity trajectory following test during which the X and Z axes are controlled using the Optitrack position control, while the Y uses only the velocity sensor measurements for control. The last 2.5 s is a transition back to Optitrack position control for landing; this induces transients due to the change in control schema. The tests were then repeated using the Optitrack as the input to the velocity feedback controller, allowing comparison between control using the velocity sensor and ideal measurements.

The tests carried out were:

- Static drift compensation test (reference $dY = 0$), measuring both drift velocity and posi-

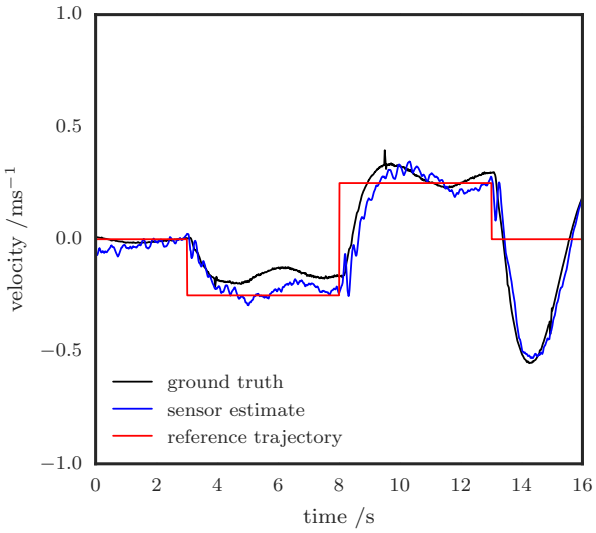

Figure 5.17: Velocity small step response using sensor.

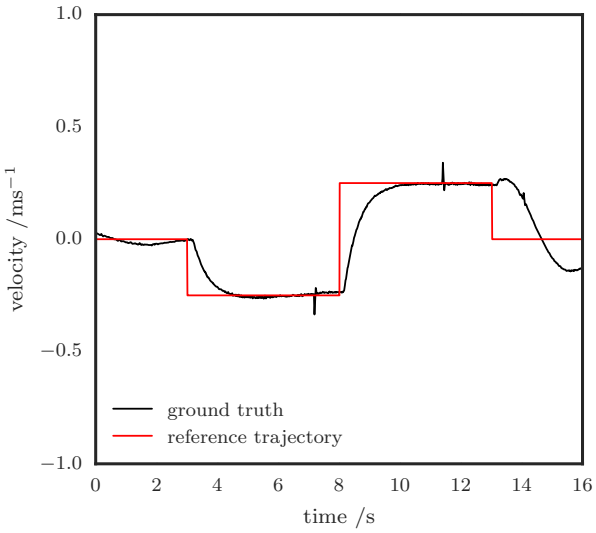

Figure 5.18: Velocity small step response using Optitrack.

tion over time (figures C.1–C.2 and C.3–C.4)

- Step functions of $dY = \pm 0.25$ ms^{-1} to assess low velocity step response (figures C.5–C.6)

- Step functions of $dY = \pm 0.5$ ms^{-1} to assess higher velocity step response (figures C.7–C.8)
- Repeating step function 'tick tocks' of $dY = \pm 0.5$ ms^{-1} for assessing long-term stability (figures C.9–C.10)
- Sinusoidal function of $dY = -0.75\sin(t)$ ms^{-1} to assess the smoothness of the output trajectory (figures C.11–C.12)

The small step response plots are included here as figures 5.17–5.18 for the other figures refer to Appendix C.

It was found that the sensors were able to sense and control velocity reliably; the flight control faithfully regulated velocity according to the estimated measurement. The velocity estimate was well correlated with the ground truth measurement, especially at higher velocities. At lower velocities, the quality of trajectory tracking was degraded, albeit still within a useful range of accuracy for flight control.

The estimates also exhibited non-negligible bias error relative to ground truth, most noticeably in the drift compensation test. This is expected, given that the sensor is aerodynamic

and receives very little signal around stationary hover. This would indicate that these sensors are promising, but will require further improvement before they are suitable for unaided drift compensation.

One phenomena noticed during the experiments is the lag between the measured ground truth velocity data and the sensor estimate. It is thought that this is due to the processing and filtering, and that this might have some influence on the relative performance of the flight control. It would be interesting to explore flying the aircraft using raw measurements, without this filtering enabled.

Chapter 6

Conclusion

This work sought to understand fundamental aerodynamic phenomena of quadrotor flight and exploit them for control. It covered the development of an experimental quadrotor platform specially designed for repeatable flight and a new type of high performance force sensor capable of measuring rotor forces in flight. Together, these technologies were able to further our understanding of ground effect; allow exploration of passive position control; and develop a new method for lateral velocity measurement and control.

6.1 Achievements

Consistent quadrotor performance is critical to observing the often subtle effects of aerodynamic phenomena and correlating results from multiple experiments. One of the biggest factors in consistent performance is the decreasing supply voltage as the flight battery is discharged, which leads to variability in the response of the aircraft. This was overcome through the addition of a regulator to maintain constant voltage delivered to the drive system, irrespective of battery voltage. As a result trajectory tracking consistency was improved. It was also found that sacrificing vertical trajectory tracking accuracy led to increased lateral tracking accuracy.

Previously it was common to model the effect of the ground on the rotors of a quadrotor based on the well-regarded model for helicopters developed by Cheeseman and Bennett [Cheeseman and Bennett, 1955]. However, this model does not take into account the interaction of airflow from multiple rotors operating in proximity to one another, as with a quadrotor. By conducting experiments with a regulated quadrotor flying within ground effect it was possible for the first time to obtain precise measurements of this effect. It was observed that the effect extended beyond the distances predicted by model. To compensate for this, the model was extended to include a rotor scaling parameter which is 1 on a conventional helicopter

and 1.4 for a quadrotor. For the test aircraft this corresponds to the distance from the geometric centre to the furthest rotor tip, suggesting that the four rotors entrain a column similarly to a single large rotor. With this modification the model was found to accurately describe ground effect acting on a quadrotor.

The repulsive nature of the ground effect is often exploited to achieve soft landing of VTOL aircraft. By supplying a constant power to the rotors of a quadrotor that is below the power required for free air hover, a quadrotor was made to passively regulate its height above the ground. The ground effect mechanic was employed as a passive control device: ground effect provides the restoring force while rotor inflow damping provides a force which resists motion. These effects were further exploited by canting the rotors and flying above a v-shaped ground channel. In this way, the mechanics of ground effect act to provide a passive restoring force, to achieve passive lateral position keeping.

Quadrotors translate by generating forces at the rotors through interaction with the air. Knowledge of these forces is fundamental to understanding how a quadrotor will behave during flight, and to achieving high-performance control. Previously, forces were generally estimated by observing the position response of the quadrotor or through sophisticated rotor models. We instead developed a micro rotor force sensor capable of measuring the axial and lateral forces acting on the rotors of a quadrotor during flight. The sensor costs less than $50 in parts, weighs 3 g and is capable of measuring sub mN forces and sub mN.m torques at 1000 Hz.

Accurate measurement of vehicle velocity is critical to achieving precision trajectory tracking and control. Rotor blade flapping and induced drag are aerodynamic effects which occur during the lateral motion of a rotor. The influence of these effects was measured directly with the motor force sensor — when combined with a theoretical description of these effects the lateral velocity of rotor could be computed directly. The lateral velocity measurements from each rotor on a quadrotor were combined to obtain vehicle velocity and cancel out effects due to rotational velocity of the vehicle. Measurement of lateral velocities of up to 1 ms^{-1} with a precision of $\pm 0.1 ms^{-1}$ was achieved and subsequently used for closed loop velocity control on a quadrotor.

6.2 Future Work

The goal of this thesis was "to enable a hovering robot to robustly travel through a corridor, passageway or duct without any additional onboard sensing". We have established several new technologies in pursuit of this goal. Some work in combing technologies developed still remains. The passive position control for horizontal positioning in a v-shaped channel will be combined with the closed loop velocity control using the rotor force sensors to travel down a constructed corridor at a constant speed. While this does require additional sensing in the form of the rotor force sensor it is a sensor which uses the intrinsic body forces of the quadrotor, works both indoors and outdoors and does not require or rely upon special features of the environment. The sensor can operate in all conditions in which the quadrotor can fly. A successful cumulative demonstration of this technology working together is expected shortly.

While the effect of walls in proximity to rotors was briefly touched on in this thesis, there is still significant opportunity for exploration. The rotor force sensors offer a new method to observe wall effect which could eventually lead to a method to sense and avoid walls based on the aerodynamic interactions. This would be another step toward collision free flight indoors without extrinsic sensing.

Airspeed measurement on a quadrotor is still a largely unexplored problem. However, the use of rotor force sensors in estimating vehicle velocity has shown significant promise and is currently the highest precision sensor available to quadrotors, that works in all conditions. This should be explored further with flights at larger velocities and in the presence of aerodynamic disturbances. This could potentially be used to improve trajectory tracking and position hold by detecting and rejecting disturbances instantaneously. It will be especially useful in wind gust disturbance rejection. Furthermore by combining these lateral force measurements with the IMU or other sensors velocity estimation could be improved especially at low speeds where the rotor force sensors are less accurate. This will form the basis of a new research project starting in 2017.

References

[3D Robotics Inc., 2017] 3D Robotics Inc. (2017). Pixhawk. https://store.3dr.com/t/pixhawk.

[Achtelik *et al*, 2009] Achtelik, M., Bachrach, A., He, R., Prentice, S., and Roy, N. (2009). Autonomous navigation and exploration of a quadrotor helicopter in gps-denied indoor environments. In *First Symposium on Indoor Flight*.

[Alciatore and Histand, 2012] Alciatore, D. G. and Histand, M. B. (2012). *Introduction to mechatronics and measurement systems*. McGraw-Hill, fourth edition.

[Allibert *et al*, 2016] Allibert, G., Mahony, R., and Bangura, M. (2016). Velocity aided attitude estimation for aerial robotic vehicles using latent rotation scaling. In *Robotics and Automation, 2016 IEEE International Conference on*, pages 1538–1543.

[Altuğ *et al*, 2002] Altuğ, E., Ostrowski, J. P., and Mahony, R. (2002). Control of a quadrotor helicopter using visual feedback. In *Robotics and Automation, 2002. Proceedings. ICRA'02. IEEE International Conference on*, volume 1, pages 72–77. IEEE.

[ArduPilot Dev Team, 2016] ArduPilot Dev Team (2016). Ardupilot open source autopilot. http://ardupilot.org/.

[Armattan Quads, 2017] Armattan Quads (2017). Armattan mrp 130 fpv. http://www.armattanquads.com/mrp-130/.

[Ascending Technologies, 2017] Ascending Technologies (2017). Leading UAS drone technology, autopilot & multirotor UAV solutions : Ascending technologies. http://www.asctec.de/en/.

[ATI Industrial Automation, 2017] ATI Industrial Automation (2017). Multi-axis force / torque sensors. http://www.ati-ia.com/products/ft/sensors.aspx.

[Bakke, 2011] Bakke, R. (2011). Build kapteinkuks simple and low part count quad, hex and tricopter flight controller. https://www.rcgroups.com/forums/showthread.php?1143569.

[Bangura *et al*, 2015] Bangura, M., Kuipers, F., Allibert, G., and Mahony, R. (2015). Non-linear velocity aided attitude estimation and velocity control for quadrotors. In *Australasian Conference on Robotics and Automation*.

[Bangura *et al*, 2014] Bangura, M., Lim, H., Kim, H. J., and Mahony, R. (2014). Aerodynamic power control for multirotor aerial vehicles. In *Robotics and Automation, 2014 IEEE International Conference on*, pages 529–536.

[Bangura and Mahony, 2012] Bangura, M. and Mahony, R. (2012). Nonlinear dynamic modeling for high performance control of a quadrotor. In *Australasian Conference on Robotics and Automation*, pages 1–10.

[Bangura and Mahony, 2014] Bangura, M. and Mahony, R. (2014). Real-time model predictive control for quadrotors. *IFAC Proceedings Volumes*, 47(3):11773–11780. 19th {IFAC} World Congress.

[Baseflight Team, 2017] Baseflight Team (2017). Baseflight: 32 bit fork of the multiwii rc flight controller firmware. https://github.com/multiwii/baseflight.

[Berry *et al*, 2012] Berry, B., Bowen-Davies, G., Gluesenkamp, K., Kaler, Z., Schmaus, J., Staruk, W., Weiner, E., Woods, B. K., *et al* (2012). Design optimization of gamera ii: a human powered helicopter. In *Proceedings of the 68th American Helicopter Society Annual Forum*, pages 1–19. American Helicopter Soc. Alexandria, VA.

[Betaflight Team, 2017] Betaflight Team (2017). Betaflight. https://github.com/betaflight/betaflight.

[Blösch *et al*, 2010] Blösch, M., Weiss, S., Scaramuzza, D., and Siegwart, R. (2010). Vision based mav navigation in unknown and unstructured environments. In *Robotics and automation (ICRA), 2010 IEEE international conference on*, pages 21–28. IEEE.

[Bouabdallah *et al*, 2004] Bouabdallah, S., Noth, A., and Siegwart, R. (2004). Pid vs lq control techniques applied to an indoor micro quadrotor. In *Intelligent Robots and Systems, 2004.(IROS 2004). Proceedings. 2004 IEEE/RSJ International Conference on*, volume 3, pages 2451–2456. IEEE.

[Bouabdallah and Siegwart, 2005] Bouabdallah, S. and Siegwart, R. (2005). Backstepping and sliding-mode techniques applied to an indoor micro quadrotor. In *Robotics and Automation, 2005. ICRA 2005. Proceedings of the 2005 IEEE International Conference on*, pages 2247–2252. IEEE.

[Bouffard *et al*, 2012] Bouffard, P., Aswani, A., and Tomlin, C. (2012). Learning-based model predictive control on a quadrotor: Onboard implementation and experimental results. In *Robotics and Automation (ICRA), 2012 IEEE International Conference on*, pages 279–284. IEEE.

[Burri *et al*, 2012] Burri, M., Nikolic, J., Hürzeler, C., Caprari, G., and Siegwart, R. (2012). Aerial service robots for visual inspection of thermal power plant boiler systems. In *Applied Robotics for the Power Industry (CARPI), 2012 2nd International Conference on*, pages 70–75. IEEE.

[Carpenter and Fridovitch, 1953] Carpenter, P. and Fridovitch, B. (1953). Effect of rapid blade pitch increase on the thrust and induced velocity response of a full scale helicopter rotor. Technical report, National Advisory Committee for Aeronautics. TN-3044.

[Cheerson, 2017] Cheerson (2017). Experience the dream of flying from chengxin sail. `http://www.cheersonhobby.com/en-US`.

[Cheeseman and Bennett, 1955] Cheeseman, I. C. and Bennett, W. E. (1955). The effect of the ground on a helicopter rotor in forward flight. Technical report, Aeronautical Research Council.

[Cleanflight Team, 2017] Cleanflight Team (2017). Cleanflight: Open-source flight controller software for modern flight boards. `http://cleanflight.com/`.

[Cook, 2012] Cook, M. V. (2012). *Flight dynamics principles: a linear systems approach to aircraft stability and control*. Butterworth-Heinemann.

[Davis *et al*, 2013] Davis, E., Nizette, B. E., and Yu, C. (2013). Development of a low cost quadrotor platform for swarm experiments. In *Control Conference, 2013 Chinese*, pages 7072–7077.

[Dillow, 2014] Dillow, C. (2014). Get ready for drone nation. `http://fortune.com/2014/10/08/drone-nation-air-droid/`.

[DIY Drones Community, 2017] DIY Drones Community (2017). Diy drones — the leading community for personal uavs. `http://diydrones.com/`.

[DJI Technology, 2017] DJI Technology (2017). Dji — the world leader in camera drones/quadcopters for aerial photography. `http://www.dji.com/products/drones`.

[Draganfly Innovations, 2016] Draganfly Innovations (2016). The story behind draganfly innovations. `http://www.draganfly.com/story`.

[Driessens and Pounds, 2015] Driessens, S. and Pounds, P. (2015). The triangular quadrotor: a more efficient quadrotor configuration. *IEEE Transactions on Robotics*, 31(6):1517–1526.

[Efe, 2012] Efe, M. O. (2012). Battery power loss compensated fractional order sliding mode control of a quadrotor uav. *Asian Journal of Control*, pages 413–425.

[Ehang Inc., 2017] Ehang Inc. (2017). Ehang184 autonomous aerial vehicle. `http://www.ehang.com/ehang184/`.

[Fields *et al*, 2015] Fields, T. D., Ellis, L. M., and King, G. W. (2015). Quadrotor 6-dof hil simulation and verification using a 6-axis load cell. In *AIAA Atmospheric Flight Mechanics Conference*, page 1479.

[Fontana *et al*, 2012] Fontana, M., Marcheschi, S., Salsedo, F., and Bergamasco, M. (2012). A three-axis force sensor for dual finger haptic interfaces. *Sensors*, 12(10):13598–13616.

[Franklin *et al*, 2009] Franklin, G. F., Powell, J. D., and Emami-Naeini, A. (2009). *Feedback Conreol of Dynamic Systems*. Pearson Higher Education, sixth edition.

[Gebhardt *et al*, 2016] Gebhardt, C., Hepp, B., Nägeli, T., Stevšić, S., and Hilliges, O. (2016). Airways: Optimization-based planning of quadrotor trajectories according to high-level user goals. In *Proceedings of the 2016 CHI Conference on Human Factors in Computing Systems*, pages 2508–2519. ACM.

[Gioioso *et al*, 2014] Gioioso, G., Ryll, M., Prattichizzo, D., Bülthoff, H. H., and Franchi, A. (2014). Turning a near-hovering controlled quadrotor into a 3d force effector. In *Robotics and Automation (ICRA), 2014 IEEE International Conference on*, pages 6278–6284. IEEE.

[GoPro Inc., 2017] GoPro Inc. (2017). Gopro — karma. `https://shop.gopro.com/APAC/karma`.

[Hehn and D'Andrea, 2011] Hehn, M. and D'Andrea, R. (2011). A flying inverted pendulum. In *Robotics and Automation (ICRA), 2011 IEEE International Conference on*, pages 763–770. IEEE.

[Heyson, 1973] Heyson, H. H. (1973). Theoretical and experimental investigation of the performance of a fan-in-wing vtol configuration. Technical report, NASA.

[Heyson, 1974] Heyson, H. H. (1974). The effect of wind-tunnel wall interference on the performance of a fan-in-wing vtol model. Technical report, NASA.

[Heyson, 1977] Heyson, H. H. (1977). Theoretical study of the effect of ground proximity on the induced efficiency of helicopter rotors. Technical report, NASA.

[HobbyKing, 2017] HobbyKing (2017). Hobbyking kk2.1 multi-rotor lcd flight control board with 6050mpu and atmel 644pa. `https://hobbyking.com/en_us/catalogsearch/result/?q=9171000334-0`.

[Hoffmann *et al*, 2004] Hoffmann, G., Rajnarayan, D. G., Waslander, S. L., Dostal, D., Jang, J. S., and Tomlin, C. J. (2004). The stanford testbed of autonomous rotorcraft for multi agent control (starmac). In *Digital Avionics Systems Conference, 2004. DASC 04. The 23rd*, volume 2, pages 12–E. IEEE.

[Hoffmann *et al*, 2007] Hoffmann, G. M., Huang, H., Waslander, S. L., and Tomlin, C. J. (2007). Quadrotor helicopter flight dynamics and control: Theory and experiment. In *AIAA Guidance, Navigation and Control Conference and Exhibit*.

[Hou and Mahony, 2013] Hou, X. and Mahony, R. (2013). Dynamic kinesthetic boundary for haptic teleoperation of aerial robotic vehicles. In *Intelligent Robots and Systems (IROS), 2013 IEEE/RSJ International Conference on*, pages 4549–4950. IEEE.

[Huang *et al*, 2009] Huang, H., Hoffmann, G. M., Waslander, S. L., and Tomlin, C. J. (2009). Aerodynamics and control of autonomous quadrotor helicopters in aggressive maneuvering. In *Robotics and Automation, 2009. ICRA'09. IEEE International Conference on*, pages 3277–3282. IEEE.

[Iizuka *et al*, 1985] Iizuka, K., Uzuhashi, H., Kano, M., Endo, T., and Mohri, K. (1985). Microcomputer control for sensorless brushless motor. *IEEE Transactions on Industry Applications*, (3):595–601.

[Intaratep *et al*, 2016] Intaratep, N., Alexander, W. N., Devenport, W. J., Grace, S. M., and Dropkin, A. (2016). Experimental study of quadcopter acoustics and performance at static thrust conditions. In *22nd AIAA/CEAS Aeroacoustics Conference*, page 2873.

[JR3 Inc., 2017] JR3 Inc. (2017). Multi-axis load cell technologies. `http://www.jr3.com/products.html`.

[KDE Direct, 2017] KDE Direct (2017). Kde direct – make it yours. `https://www.kdedirect.com/`.

[Kirby, 2017] Kirby, S. (2017). Open source firmware for atmega-based brushless escs. `https://github.com/sim-/tgy`.

[Kushleyev *et al*, 2013] Kushleyev, A., Mellinger, D., Powers, C., and Kumar, V. (2013). Towards a swarm of agile micro quadrotors. *Autonomous Robots*, pages 287–300.

[Lee *et al*, 2015] Lee, D., Awan, A., Kim, S., and Kim, H. J. (2015). Adaptive control for a vtol uav operating near a wall. In *AIAA Guidance, Navigation, and Control Conference*.

[Leishman, 2002] Leishman, J. G. (2002). *Principles of Helicopter Aerodynamics*. Cambridge University Press.

[LibrePilot, 2016] LibrePilot (2016). LibrePilot – open – collaborative – free. `https://www.librepilot.org/site/index.html`.

[Low *et al*, 1991] Low, R. B., Dunne, M. J., Blumen, I. J., and Tagney, G. (1991). Factors associated with the safety of ems helicopters. *The American journal of emergency medicine*, 9(2):103–106.

[Lozano *et al*, 2007] Lozano, R., Brogliato, B., Egeland, O., and Maschke, B. (2007). *Dissipative systems analysis and control: theory and applications*.

[Mahony *et al*, 2005] Mahony, R., Hamel, T., and Pflimlin, J.-M. (2005). Complementary filter design on the special orthogonal group so (3). In *Decision and Control, 2005 and 2005 European Control Conference. CDC-ECC'05. 44th IEEE Conference on*, pages 1477–1484. IEEE.

[Mahony *et al*, 2012] Mahony, R., Kumar, V., and Corke, P. (2012). Multirotor aerial vehicles: Modeling, estimation, and control of quadrotor. *IEEE Robotics Automation Magazine*, 19(3):20–32.

[Martin and Salaün, 2010] Martin, P. and Salaün, E. (2010). The true role of accelerometer feedback in quadrotor control. In *Robotics and Automation, 2010 IEEE International Conference on*, pages 1623–1629. IEEE.

[Mellinger *et al*, 2012] Mellinger, D., Michael, N., and Kumar, V. (2012). Trajectory generation and control for precise aggressive maneuvers with quadrotors. *The International Journal of Robotics Research*.

[Mellinger *et al*, 2013] Mellinger, D., Shomin, M., Michael, N., and Kumar, V. (2013). Cooperative grasping and transport using multiple quadrotors. In *Distributed autonomous robotic systems*, pages 545–558. Springer.

[Michael *et al*, 2010] Michael, N., Mellinger, D., Lindsey, Q., and Kumar, V. (2010). The grasp multiple micro-uav testbed. *IEEE Robotics & Automation Magazine*, 17(3):56–65.

[Microdrones, 2017] Microdrones (2017). Unmanned aerial vehicles / quadrocopters and drone-software. `https://www.microdrones.com/en/mdaircraft/`.

[MikroKopter, 2017] MikroKopter (2017). Mikrokopter. `http://www.mikrokopter.de/en/home`.

[Mueller and D'Andrea, 2014] Mueller, M. W. and D'Andrea, R. (2014). Stability and control of a quadrocopter despite the complete loss of one, two, or three propellers. In *Robotics and Automation (ICRA), 2014 IEEE International Conference on*, pages 45–52. IEEE.

[Müller *et al*, 2011] Müller, M., Lupashin, S., and D'Andrea, R. (2011). Quadrocopter ball juggling. In *Intelligent Robots and Systems (IROS), 2011 IEEE/RSJ International Conference on*, pages 5113–5120. IEEE.

[MultiWiiCopter, 2017] MultiWiiCopter (2017). Wiki archive for superceded products. `http://www.multiwiicopter.com/wiki/archive/`.

[Olaeris Inc., 2017] Olaeris Inc. (2017). Olaeris — aeva — the 21st century helicopter. `http://www.olaeris.com/`.

[OpenPilot Team, 2017] OpenPilot Team (2017). OpenPilot. `https://github.com/openpilot/OpenPilot`.

[OptoForce Kft., 2016] OptoForce Kft. (2016). Senses for automation. `https://optoforce.com/`.

[Orsag *et al*, 2013] Orsag, M., Korpela, C., and Oh, P. (2013). Modeling and control of mm-uav: Mobile manipulating unmanned aerial vehicle. *Journal of Intelligent & Robotic Systems*.

[Ower and Pankhurst, 2014] Ower, E. and Pankhurst, R. C. (2014). *The measurement of air flow*. Elsevier.

[Parrot Inc., 2016] Parrot Inc. (2016). Drones, parrot store official. `https://www.parrot.com/us/DroNes`.

[Piccoli and Yim, 2015] Piccoli, M. and Yim, M. (2015). Passive stability of vehicles without angular momentum including quadrotors and ornithopters. In *Robotics and Automation (ICRA), 2015 IEEE International Conference on*, pages 1716–1721.

[Pixhawk Team, 2017] Pixhawk Team (2017). Pixhawk flight controller hardware project. `https://pixhawk.org/`.

[Podhradsky *et al*, 2013] Podhradsky, M., Bone, J., Coopmans, C., and Jensen, A. (2013). Battery model-based thrust controller for a small, low cost multirotor unmanned aerial vehicles. In *Unmanned Aircraft Systems, 2013 International Conference on*, pages 105–113.

[Pounds and Dollar, 2014] Pounds, P. and Dollar, A. (2014). Stability of helicopters in compliant contact under pd-pid control. *Transactions on Robotics*, 30(6):1472–1486.

[Pounds and Mahony, 2009] Pounds, P. and Mahony, R. (2009). Design principles of large quadrotors for practical applications. In *Robotics and Automation, 2009. ICRA'09. IEEE International Conference on*, pages 3265–3270. IEEE.

[Pounds *et al*, 2006] Pounds, P., Mahony, R., and Corke, P. (2006). Modelling and control of a quad-rotor robot. In *Proceedings Australasian Conference on Robotics and Automation 2006*. Australian Robotics and Automation Association Inc.

[Pounds *et al*, 2010] Pounds, P., Mahony, R., and Corke, P. (2010). Modelling and control of a large quadrotor robot. *Control Engineering Practice*, 18(7):691–699.

[Pounds *et al*, 2004] Pounds, P., Mahony, R., Gresham, J., Corke, P., and Roberts, J. M. (2004). Towards dynamically-favourable quad-rotor aerial robots. In *Proceedings of the 2004 Australasian Conference on Robotics & Automation*. Australian Robotics & Automation Association.

[Pounds *et al*, 2002] Pounds, P., Mahony, R., Hynes, P., and Roberts, J. M. (2002). Design of a four-rotor aerial robot. In *Proceedings of the 2002 Australasian Conference on Robotics and Automation (ACRA 2002)*, pages 145–150. Australian Robotics & Automation Association.

[Pounds, 2007] Pounds, P. E. I. (2007). *Design, construction and control of a large quadrotor micro air vehicle*. Australian National University.

[Pounds and Dollar, 2010] Pounds, P. E. I. and Dollar, A. (2010). Hovering stability of helicopters with elastic constraints. In *ASME 2010 Dynamic Systems and Control Conference*, pages 781–788. American Society of Mechanical Engineers.

[Pounds *et al*, 2009] Pounds, P. E. I., Mahony, R. E., and Corke, P. I. (2009). Design of a static thruster for microair vehicle rotorcraft. *Journal of Aerospace Engineering*, pages 85–94.

[Powers *et al*, 2013] Powers, C., Mellinger, D., Kushleyev, A., Kothmann, B., and Kumar, V. (2013). Influence of aerodynamics and proximity effects in quadrotor flight. In *Experimental Robotics*, pages 289–302. Springer.

[Prouty, 1995] Prouty, R. W. (1995). *Helicopter performance, stability, and control*. Krieger Publishing Company.

[PX4 Dev Team, 2017] PX4 Dev Team (2017). Open source for drones – PX4 pro open source autopilot. `http://px4.io/`.

[Rai-Choudhury, 2000] Rai-Choudhury, P. (2000). *MEMS and MOEMS Technology and Applications*, volume 85. Spie Press.

[Richtek Technology Corporation, 2014] Richtek Technology Corporation (2014). Understanding the characteristics of li-ion batteries and richtek power management solutions. Technical report. AN023.

[RightHand Robotics Inc., 2017] RightHand Robotics Inc. (2017). Righthand labs — takkstrip. `https://www.labs.righthandrobotics.com/takkstrip`.

[Robertson and Reichert, 2014] Robertson, C. D. and Reichert, T. M. (2014). Design and development of the atlas human-powered helicopter. *AIAA Journal*, 53(1):20–32.

[Robotiq, 2017] Robotiq (2017). Force torque sensors. `http://robotiq.com/products/robotics-force-torque-sensor/`.

[Schmaus *et al*, 2012] Schmaus, J., Berry, B., Gross, W., and Koliais, P. (2012). Experimental study of rotor performance in deep ground effect with application to a human-powered helicopter. In *68th Annual Forum of the American Helicopter Society, Fort Worth, Texas*.

[Schöllig *et al*, 2010] Schöllig, A., Augugliaro, F., Lupashin, S., and D'Andrea, R. (2010). Synchronizing the motion of a quadrocopter to music. In *Robotics and Automation (ICRA), 2010 IEEE International Conference on*, pages 3355–3360. IEEE.

[Sharf *et al*, 2014] Sharf, I., Nahon, M., Harmat, A., Khan, W., Michini, M., Speal, N., Trentini, M., Tsadok, T., and Wang, T. (2014). Ground effect experiments and model val-

idation with draganflyer x8 rotorcraft. In *Unmanned Aircraft Systems, 2014 International Conference on*, pages 1158–1166.

[Skaug, 2017] Skaug, S. (2017). Blheli for brushless esc firmware. `https://github.com/bitdump/BLHeli`.

[Sugahara *et al*, 2011] Sugahara, Y., Ikeuchi, Y., Suzuki, R., Hirata, Y., Kosuge, K., Noguchi, Y., Kikuchi, S., and Kohama, Y. P. (2011). Levitation control of experimental wing-in-ground effect vehicle along z axis and about roll and pitch axes. In *Robotics and Automation (ICRA), 2011 IEEE International Conference on*, pages 8–13. IEEE.

[Sugahara *et al*, 2012] Sugahara, Y., Minagawa, N., Kosuge, K., and Kohama, Y. P. (2012). Levitation control of experimental wing-in-ground effect vehicle along y and z axes and about three axes. In *2012 IEEE/RSJ International Conference on Intelligent Robots and Systems*, pages 488–494. IEEE.

[T-motor, 2017] T-motor (2017). T-motor – the safest propulsion system. `http://store-en.tmotor.com/`.

[Tarot RC Helicopters, 2017] Tarot RC Helicopters (2017). Tarot x690 quadcopter kit. `https://tarot-rc-heli.com/X690_Quadcopter_Kit`.

[Tau Labs, 2015] Tau Labs (2015). Tau labs. `http://taulabs.org/`.

[Tayebi and McGilvray, 2006] Tayebi, A. and McGilvray, S. (2006). Attitude stabilization of a vtol quadrotor aircraft. *IEEE Transactions on control systems technology*, 14(3):562–571.

[Tenzer *et al*, 2014] Tenzer, Y., Jentoft, L. P., and Howe, R. D. (2014). The feel of mems barometers: Inexpensive and easily customized tactile array sensors. *IEEE Robotics Automation Magazine*, 21(3):89–95.

[Troiani *et al*, 2015] Troiani, C., Martinelli, A., Laugier, C., and Scaramuzza, D. (2015). Low computational-complexity algorithms for vision-aided inertial navigation of micro aerial vehicles. *Robotics and Autonomous Systems*, 69:80–97.

[Tuta Navajas and Roa Prada, 2014] Tuta Navajas, G. H. and Roa Prada, S. (2014). Building your own quadrotor: A mechatronics system design case study. In *Engineering Mechatronics and Automation, 2014 3rd International Congress of*.

[Ure *et al*, 2015] Ure, N. K., Chowdhary, G., Toksoz, T., How, J. P., Vavrina, M. A., and Vian, J. (2015). An automated battery management system to enable persistent missions with multiple aerial vehicles. *IEEE/ASME Transactions on Mechatronics*, 20(1):275–286.

[Volocopter GmbH, 2017] Volocopter GmbH (2017). Volocopter – vc200 prototyp. `http://www.e-volo.com/index.php/en/volocopter-en/vc200-prototyp-en`.

[Weiss *et al*, 2011] Weiss, S., Scaramuzza, D., and Siegwart, R. (2011). Monocular-slam–based navigation for autonomous micro helicopters in gps-denied environments. *Journal of Field Robotics*, 28(6):854–874.

[Yuneec, 2017] Yuneec (2017). Flying cameras & drones. `http://us.yuneec.com/flying-cameras-and-drones`.

Passive Position Response Plots

This appendix contains enlarged versions of the passive lateral position response plots included in Chapter 4.

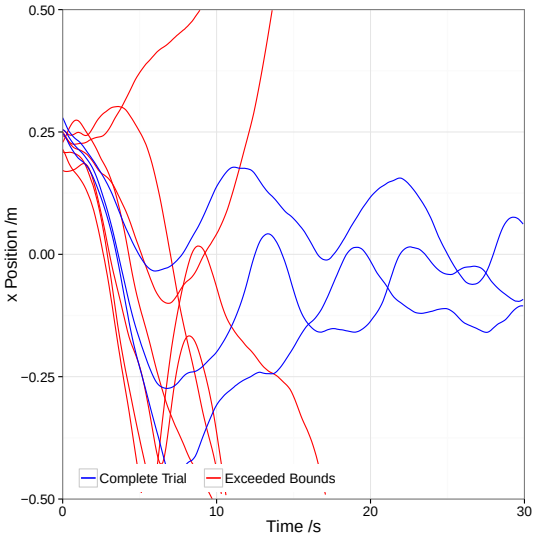

Figure A.1: passive lateral position response: rotor cant 0°; channel slope 5°

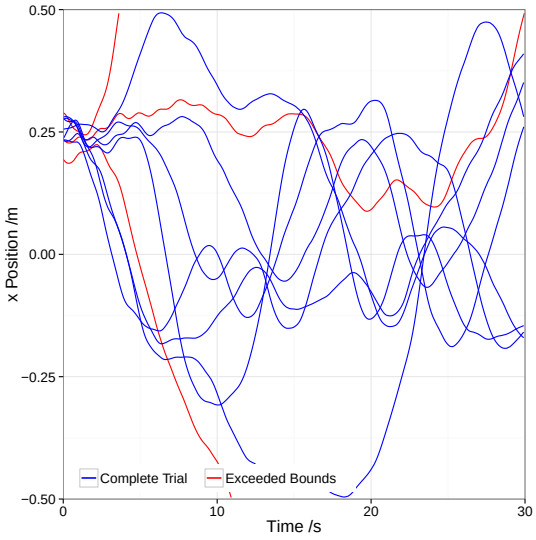

Figure A.2: passive lateral position response: rotor cant 0°; channel slope 10°

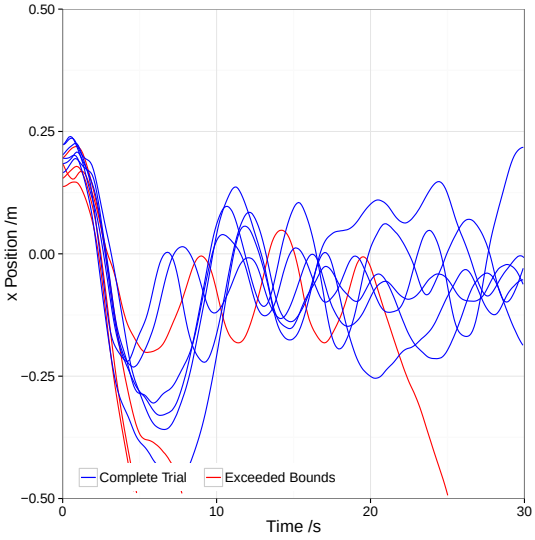

Figure A.3: passive lateral position response: rotor cant 0°; channel slope 15°

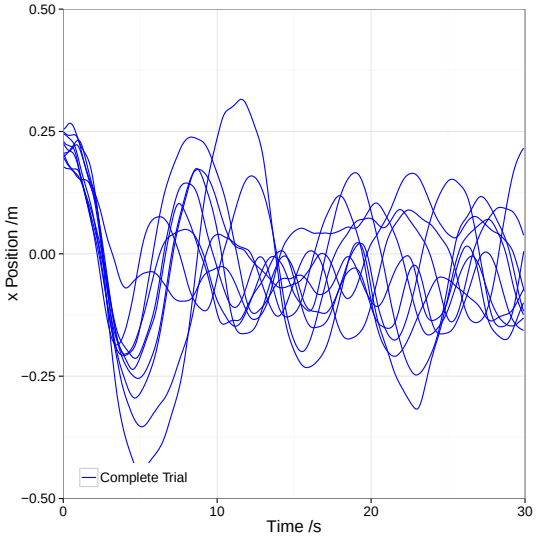

Figure A.4: passive lateral position response: rotor cant 0°; channel slope 20°

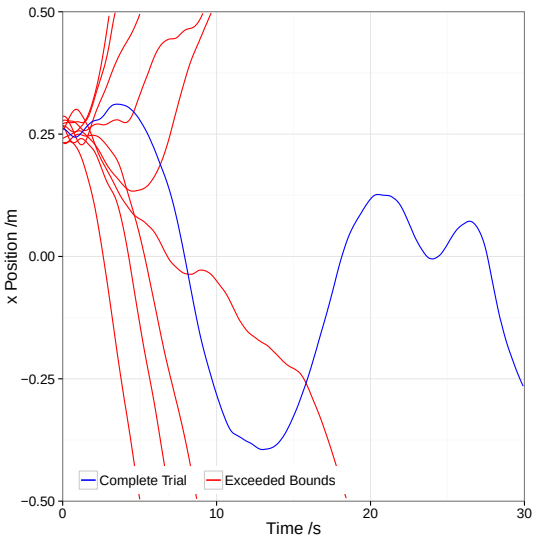

Figure A.5: passive lateral position response: rotor cant 5°; channel slope 5°

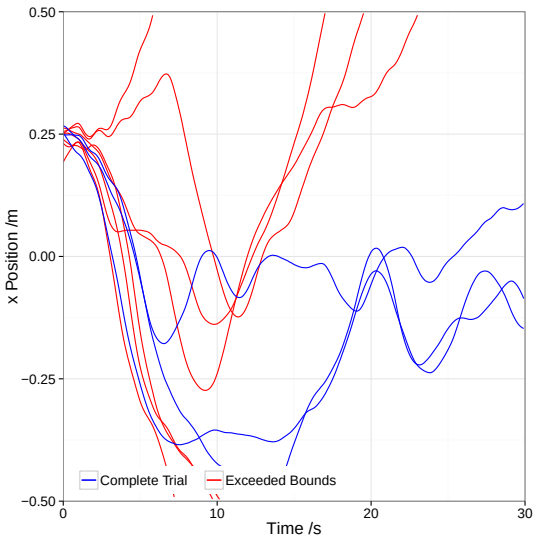

Figure A.6: passive lateral position response: rotor cant 5°; channel slope 10°

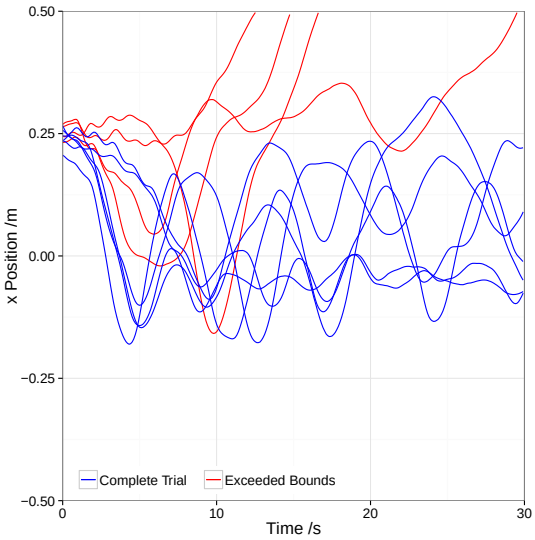

Figure A.7: passive lateral position response: rotor cant 5°; channel slope 15°

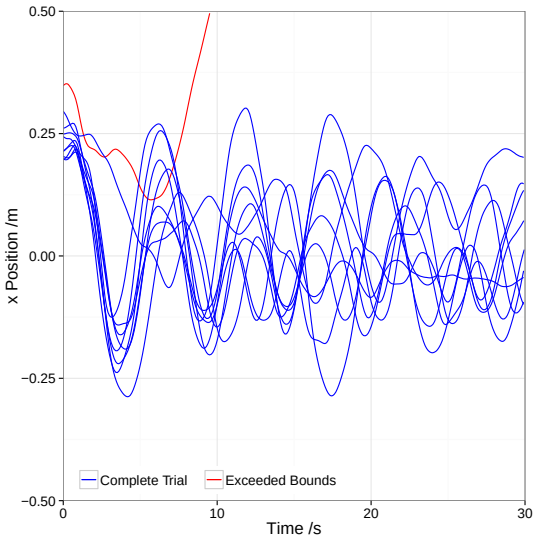

Figure A.8: passive lateral position response: rotor cant 5°; channel slope 20°

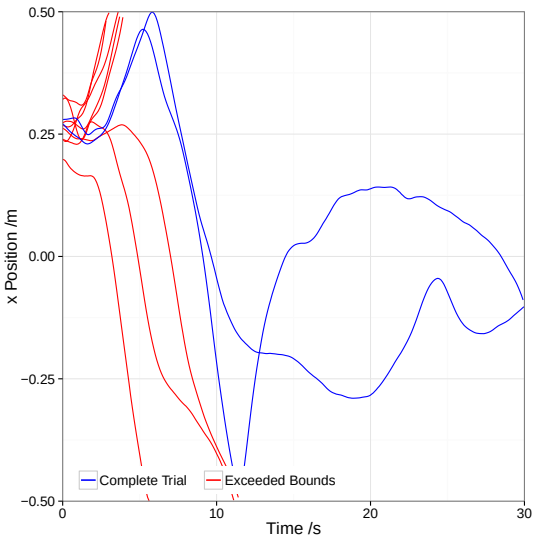

Figure A.9: passive lateral position response: rotor cant 10°; channel slope 5°

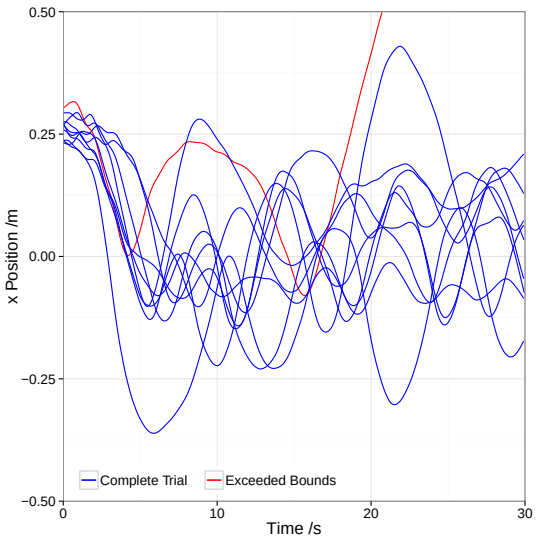

Figure A.10: passive lateral position response: rotor cant 10°; channel slope 10°

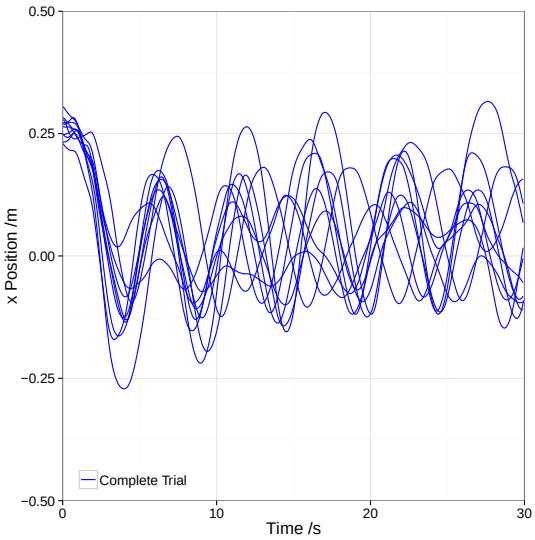

Figure A.11: passive lateral position response: rotor cant 10°; channel slope 15°

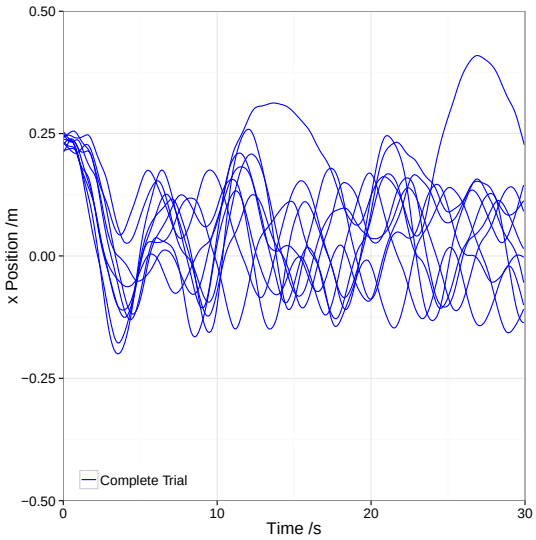

Figure A.12: passive lateral position response: rotor cant 10°; channel slope 20°

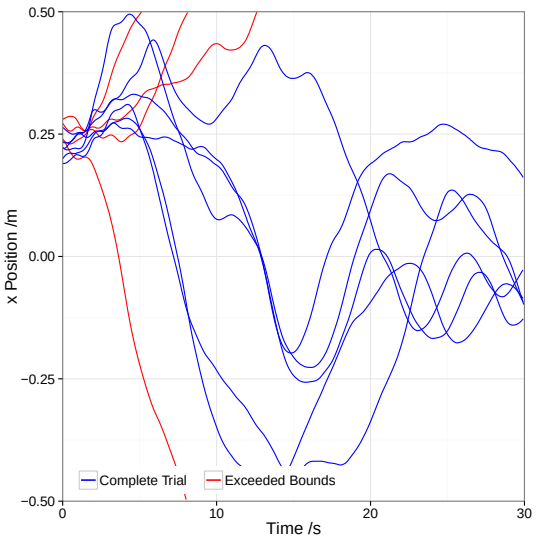

Figure A.13: passive lateral position response: rotor cant 15°; channel slope 5°

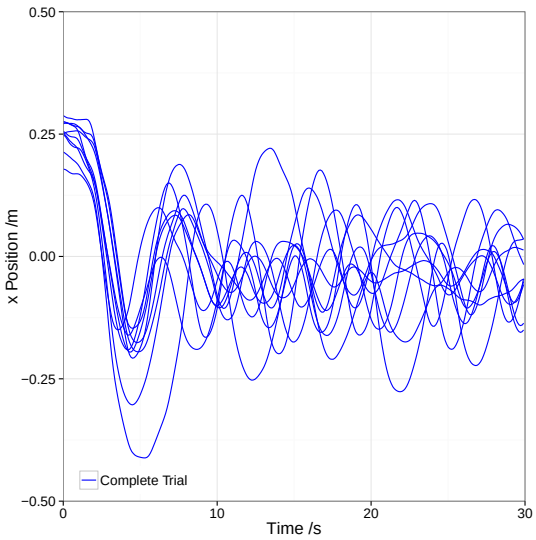

Figure A.14: passive lateral position response: rotor cant 15°; channel slope 10°

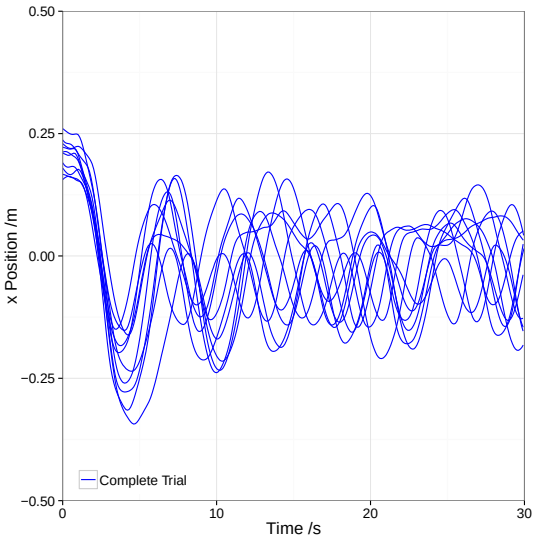

Figure A.15: passive lateral position response: rotor cant 15°; channel slope 15°

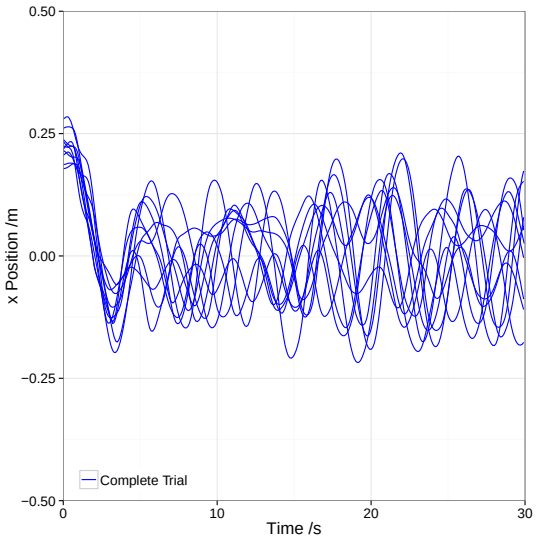

Figure A.16: passive lateral position response: rotor cant 15°; channel slope 20°

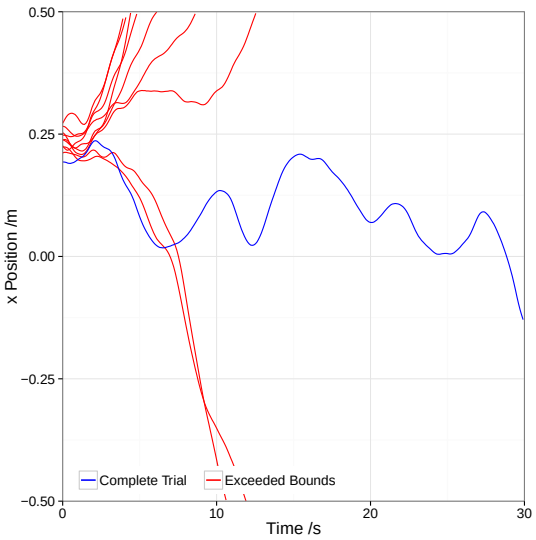

Figure A.17: passive lateral position response: rotor cant 20°; channel slope 5°

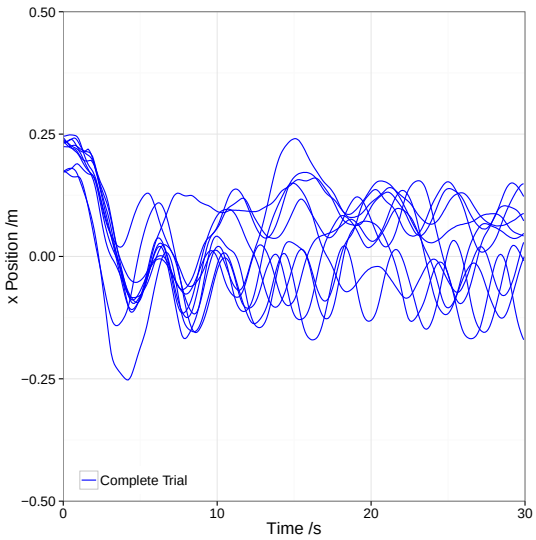

Figure A.18: passive lateral position response: rotor cant 20°; channel slope 10°

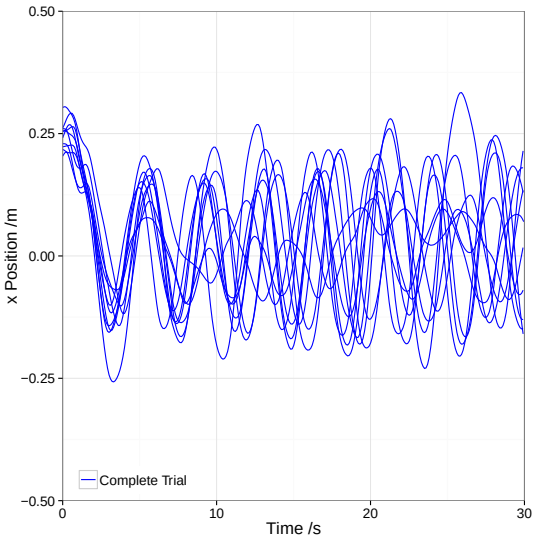

Figure A.19: passive lateral position response: rotor cant 20°; channel slope 15°

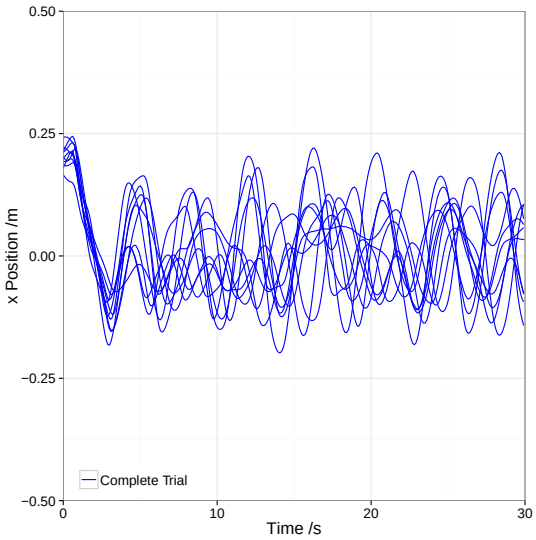

Figure A.20: passive lateral position response: rotor cant 20°; channel slope 20°

Force Sensor Velocity Plots

This appendix contains additional velocity measurement plots using a rotor force sensor as detailed in Chapter 5.

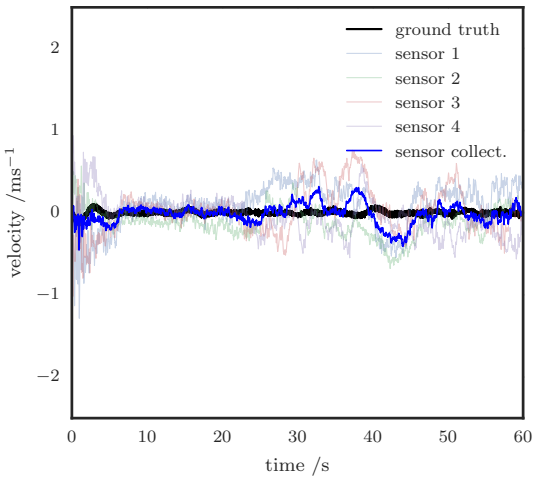

Figure B.1: Stationary hover *dx* measurements.

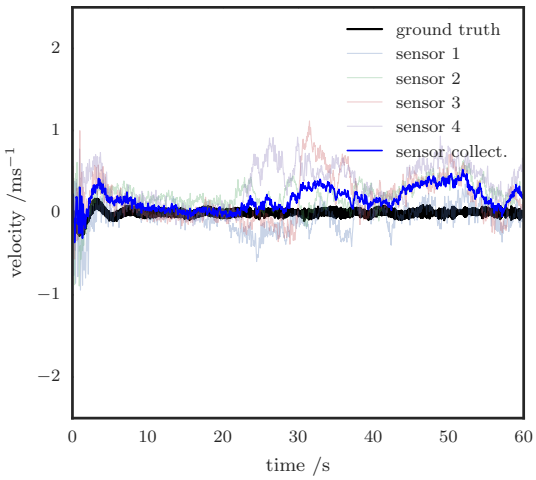

Figure B.2: Stationary hover *dy* measurements.

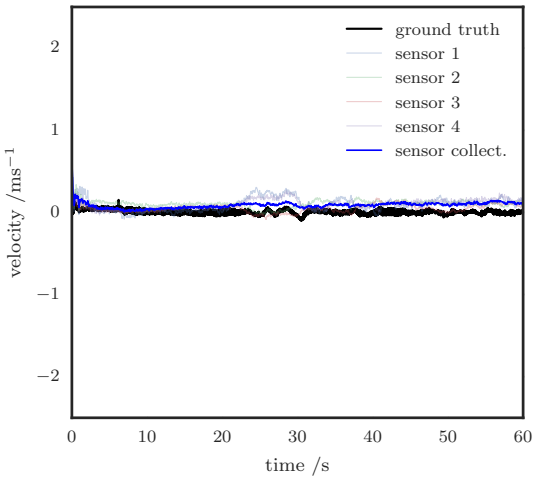

Figure B.3: Stationary hover *dz* measurements.

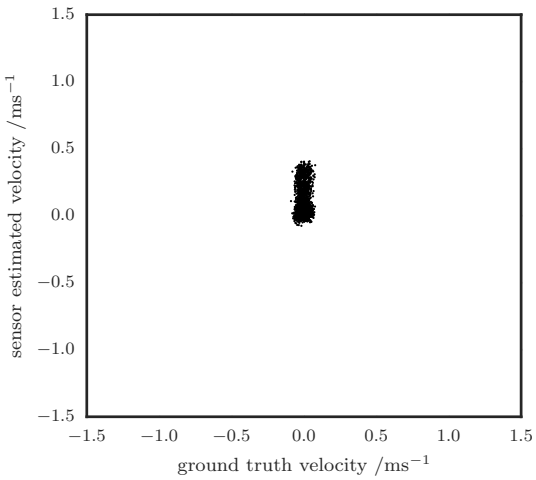

Figure B.4: Stationary hover *dy* linearity plot.

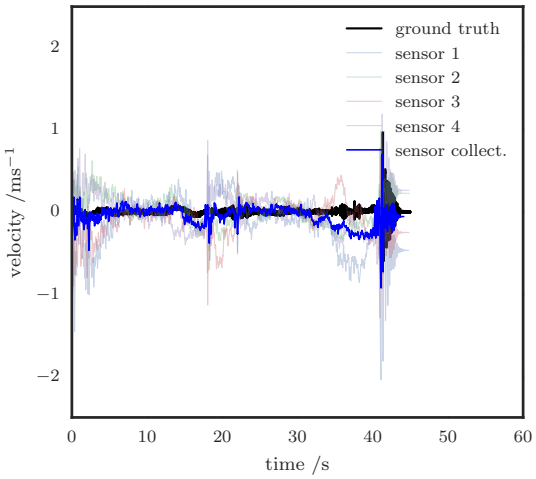

Figure B.5: Linear step path *dx* measurements.

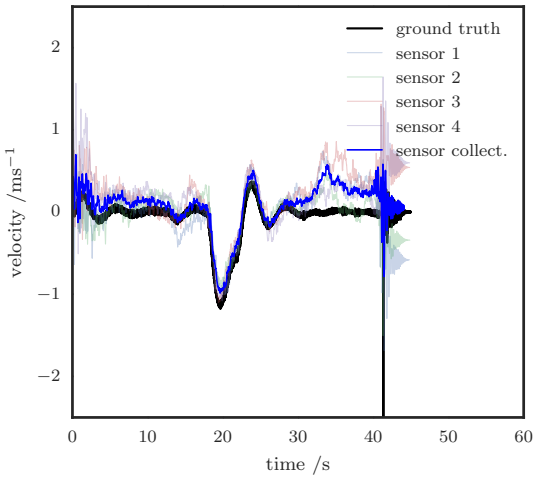

Figure B.6: Linear step path *dy* measurements.

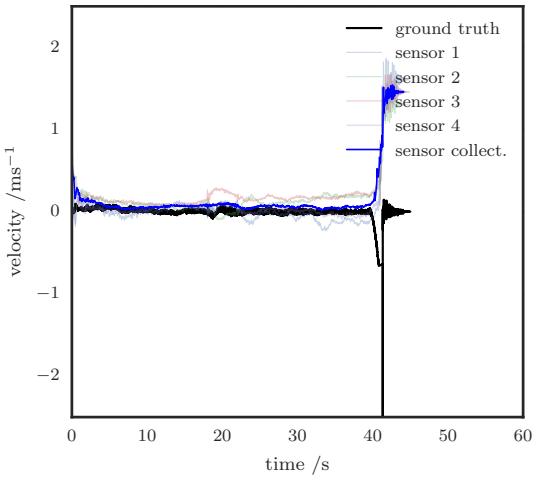

Figure B.7: Linear step path *dz* measurements.

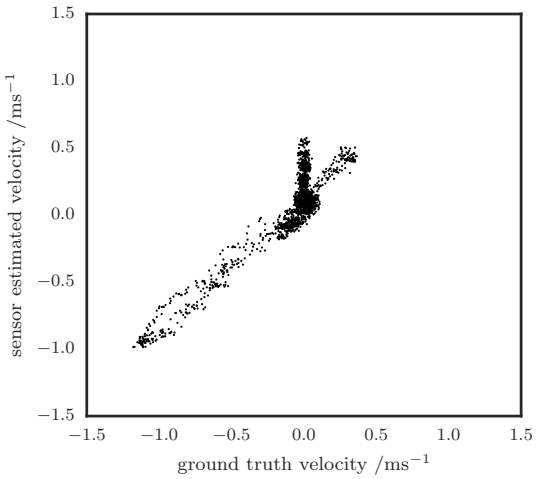

Figure B.8: Linear step path *dy* linearity plot.

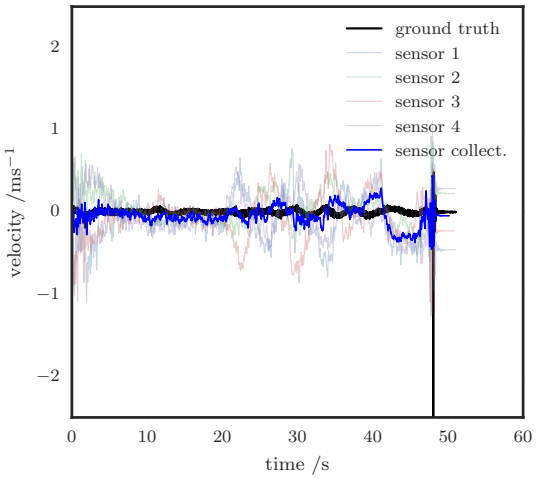

Figure B.9: Linear horizontal sinusoidal path *dx* measurements.

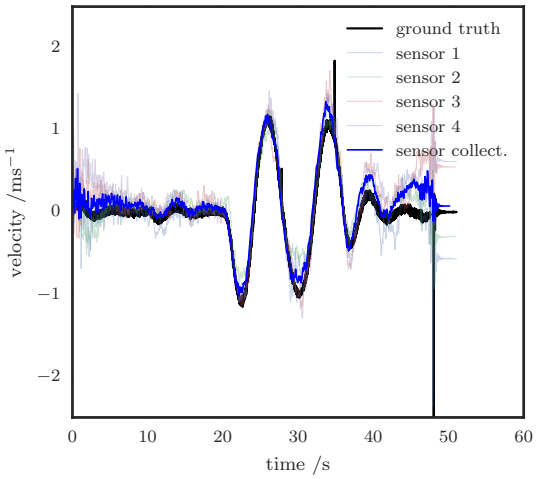

Figure B.10: Linear horizontal sinusoidal path *dy* measurements.

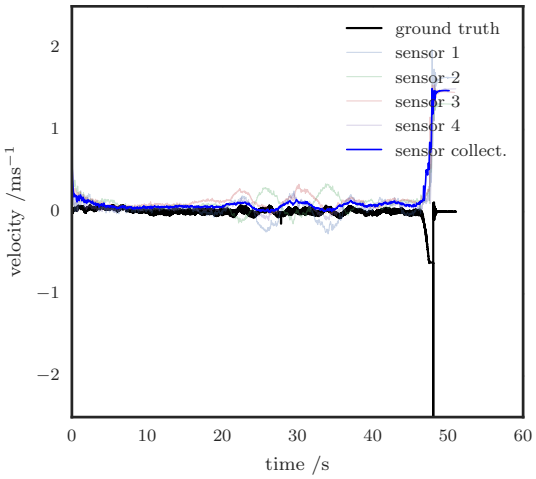

Figure B.11: Linear horizontal sinusoidal path *dz* measurements.

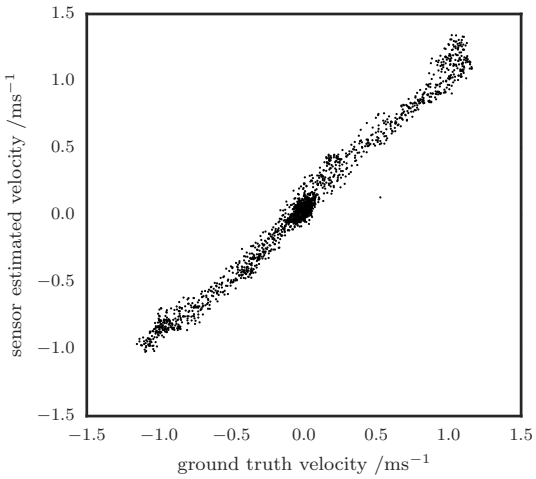

Figure B.12: Linear horizontal sinusoidal path *dy* linearity plot.

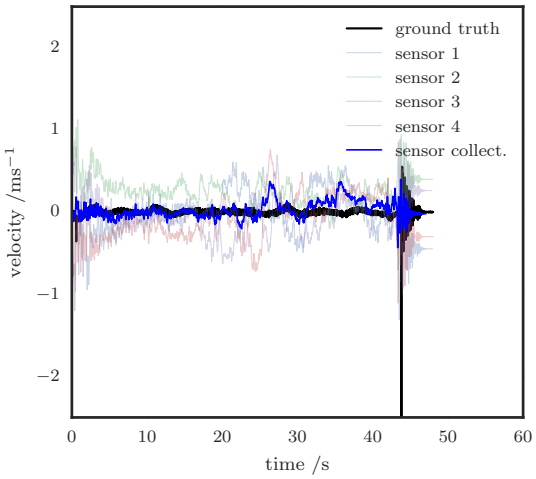

Figure B.13: Linear vertical sinusoidal path *dx* measurements.

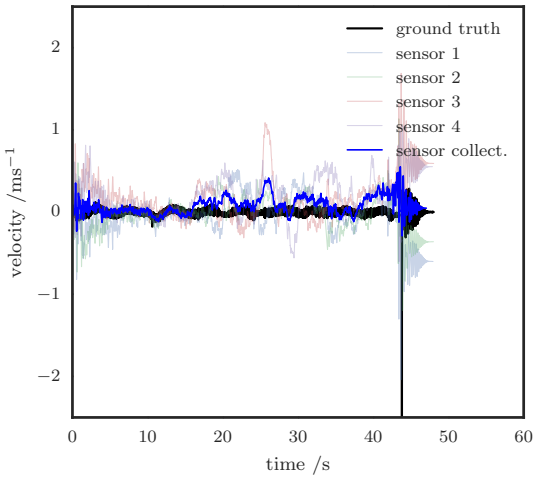

Figure B.14: Linear vertical sinusoidal path *dy* measurements.

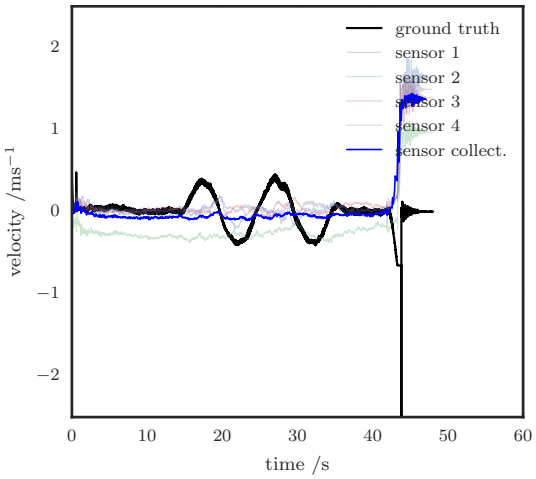

Figure B.15: Linear vertical sinusoidal path *dz* measurements.

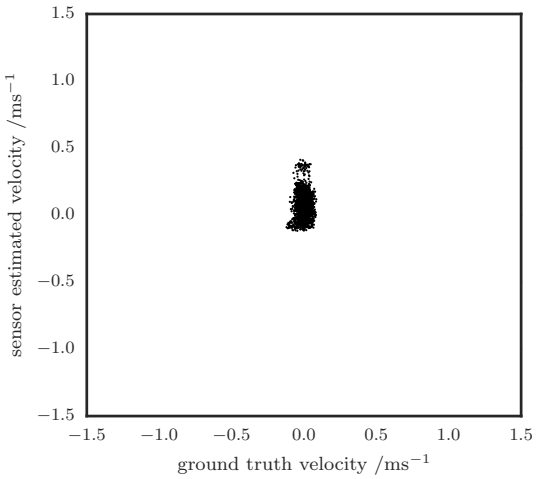

Figure B.16: Linear vertical sinusoidal path *dy* linearity plot.

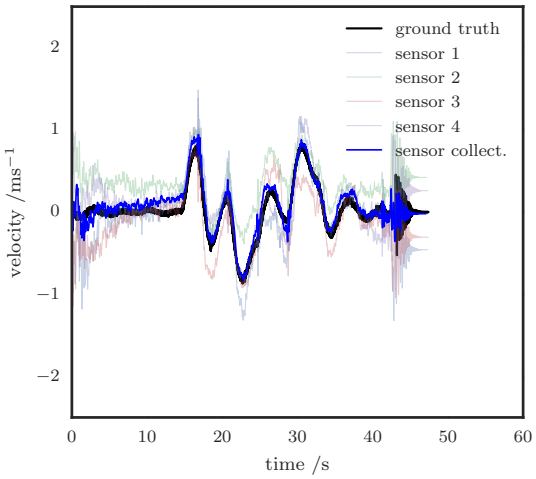

Figure B.17: Square path *dx* measurements.

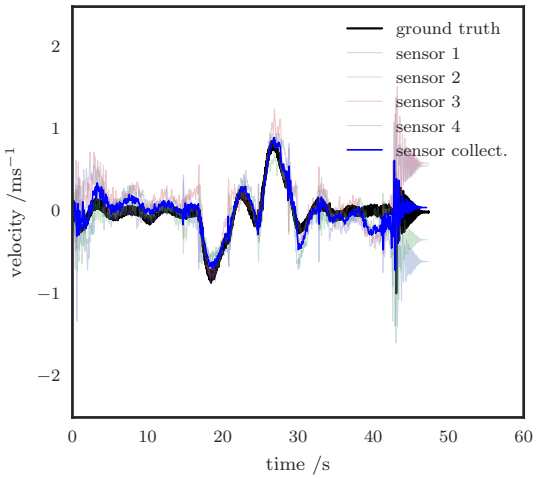

Figure B.18: Square path *dy* measurements.

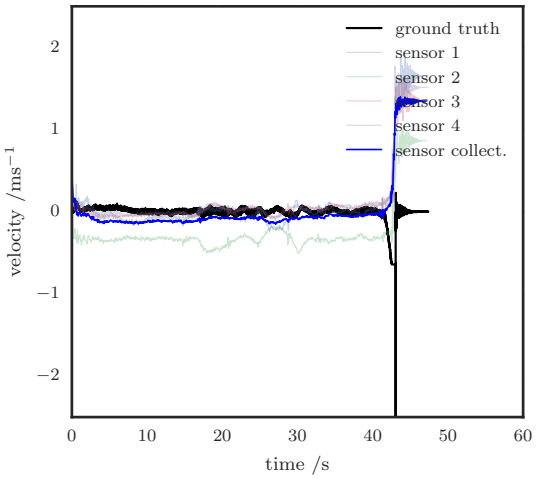

Figure B.19: Square path *dz* measurements.

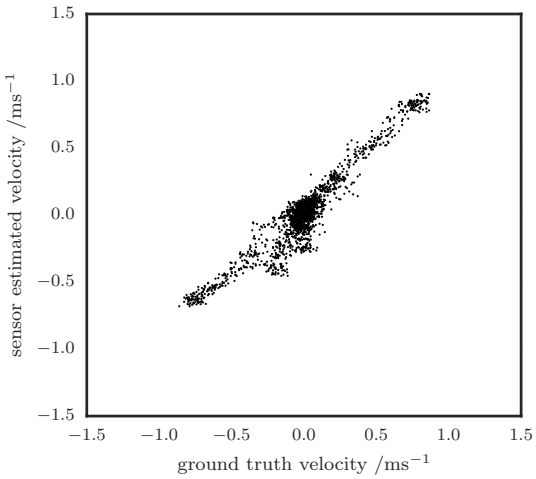

Figure B.20: Square path *dy* linearity plot.

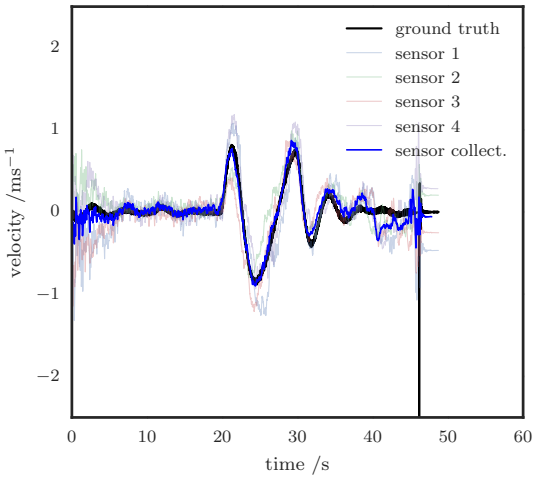

Figure B.21: Circular path *dx* measurements.

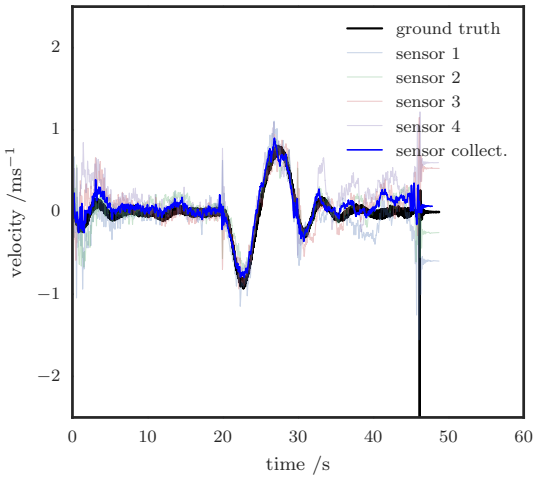

Figure B.22: Circular path *dy* measurements.

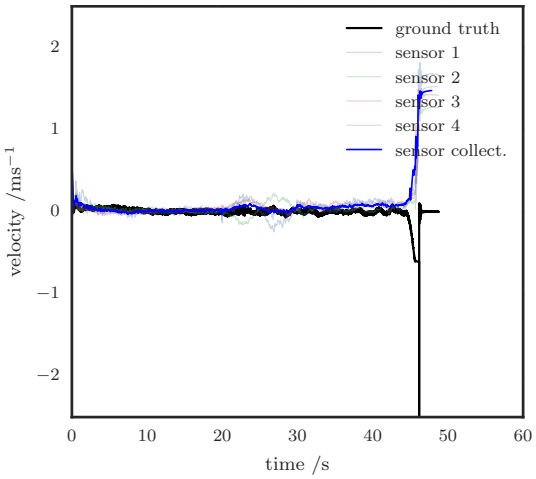

Figure B.23: Circular path *dz* measurements.

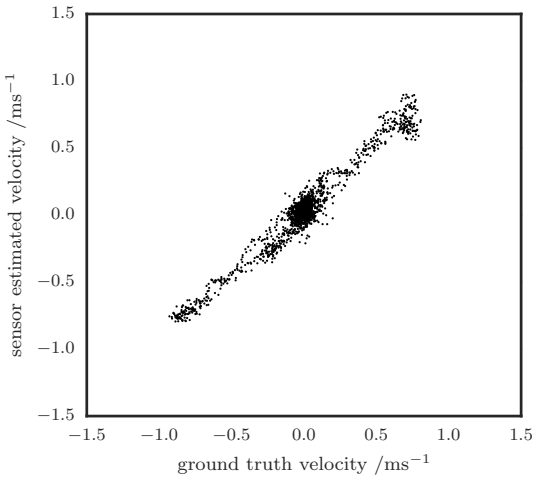

Figure B.24: Circular path *dy* linearity plot.

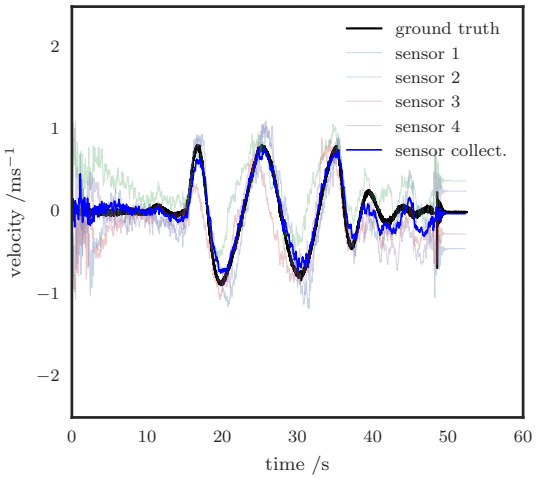

Figure B.25: Double circular path *dx* measurements.

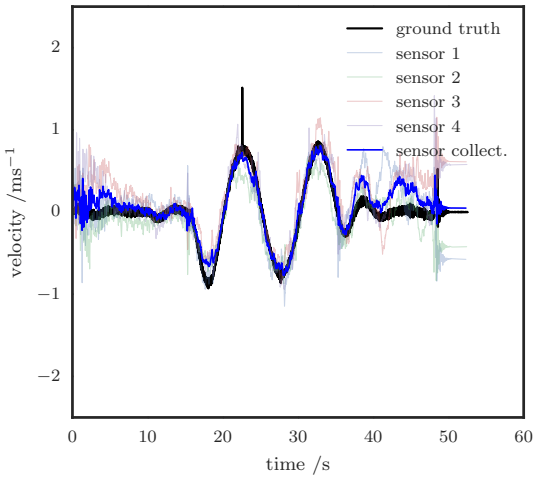

Figure B.26: Double circular path *dy* measurements.

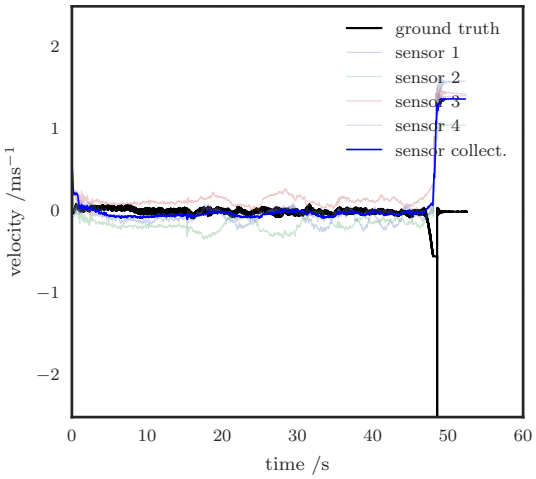

Figure B.27: Double circular path *dz* measurements.

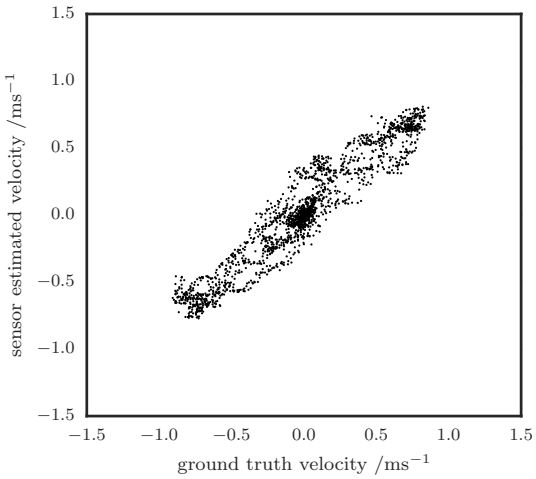

Figure B.28: Double circular path *dy* linearity plot.

Force Sensor Control Plots

This appendix contains velocity feedback control plots using a rotor force sensor as detailed in Chapter 5.

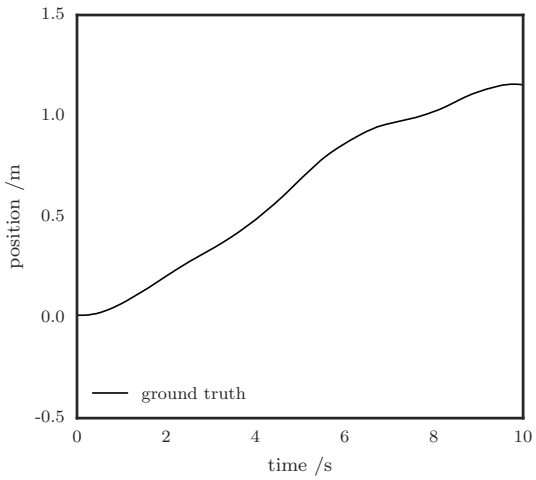

Figure C.1: Zero reference drift position using sensor.

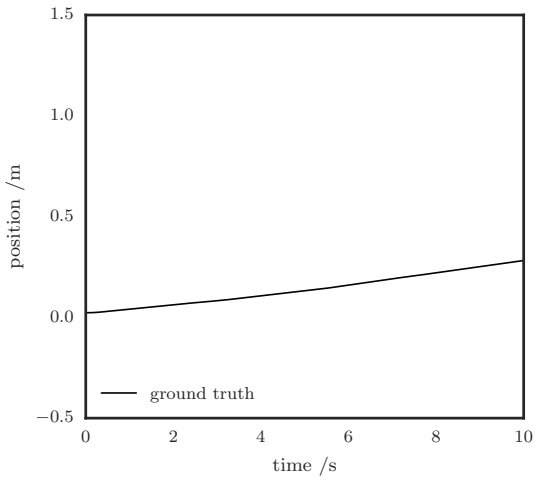

Figure C.2: Zero reference drift position using Optitrack.

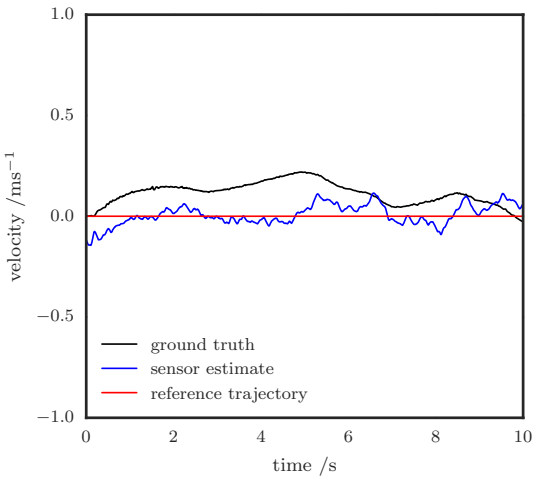

Figure C.3: Zero reference drift velocity using sensor.

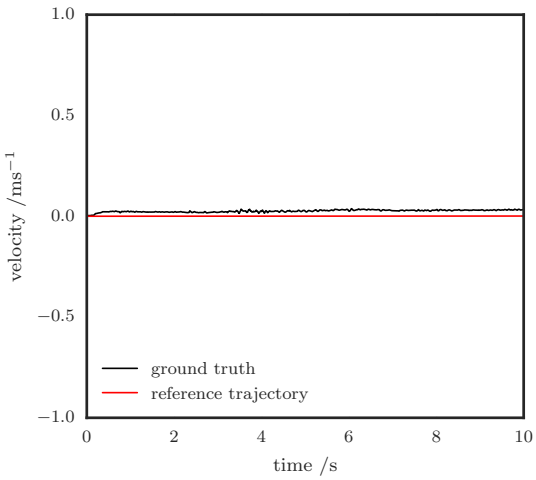

Figure C.4: Zero reference drift velocity using Optitrack.

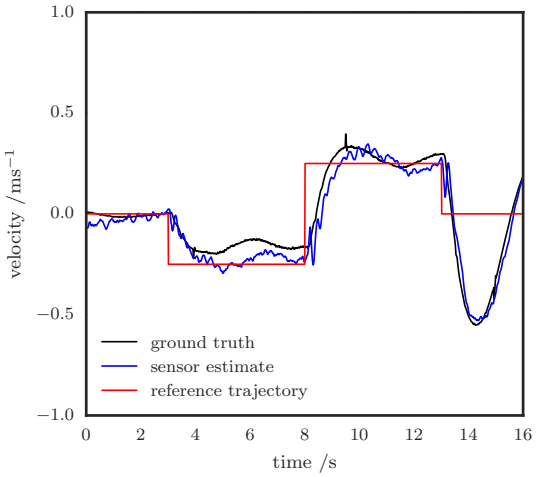

Figure C.5: Velocity small step response using sensor.

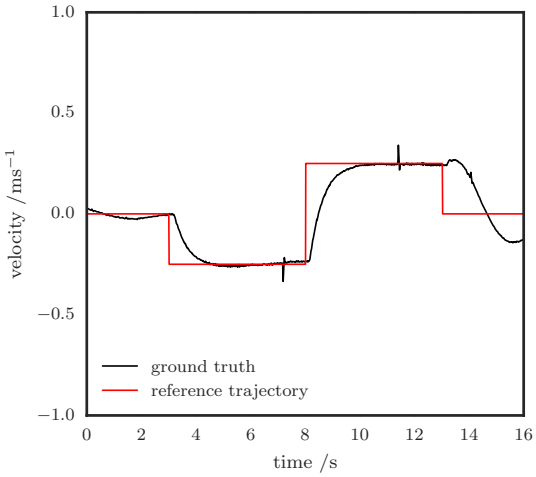

Figure C.6: Velocity small step response using Optitrack.

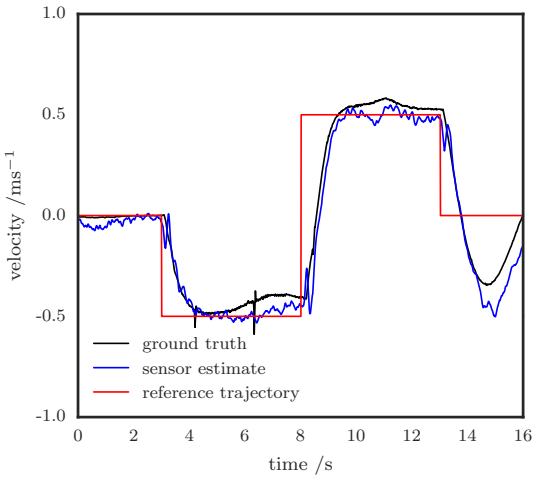

Figure C.7: Velocity large step response using sensor.

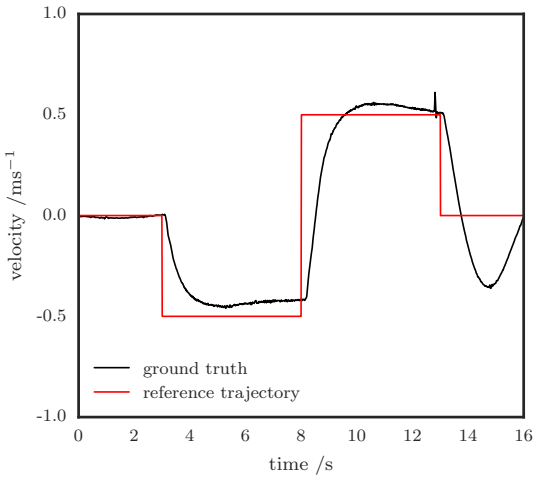

Figure C.8: Velocity large step response using Optitrack.

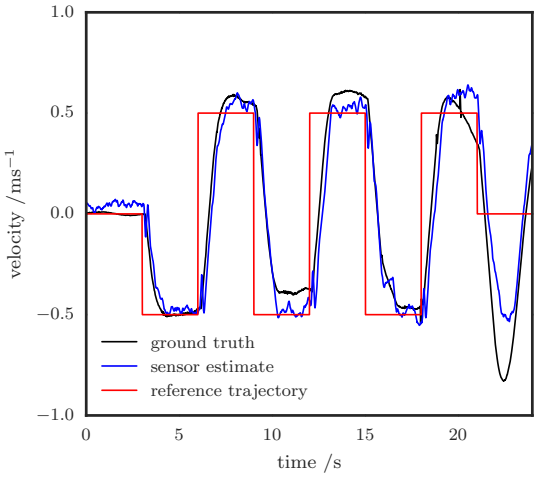

Figure C.9: Velocity tick-tock response using sensor.

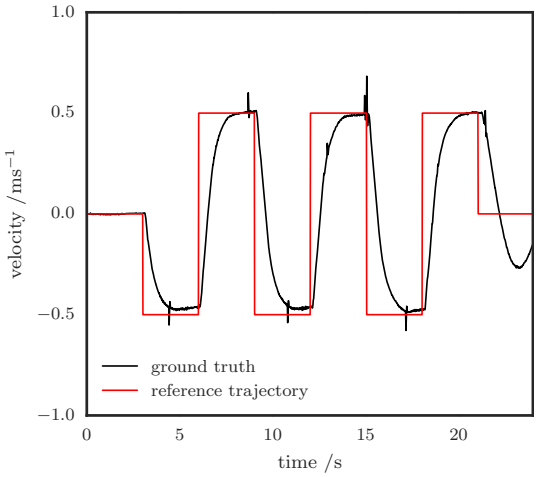

Figure C.10: Velocity tick-tock response using Optitrack.

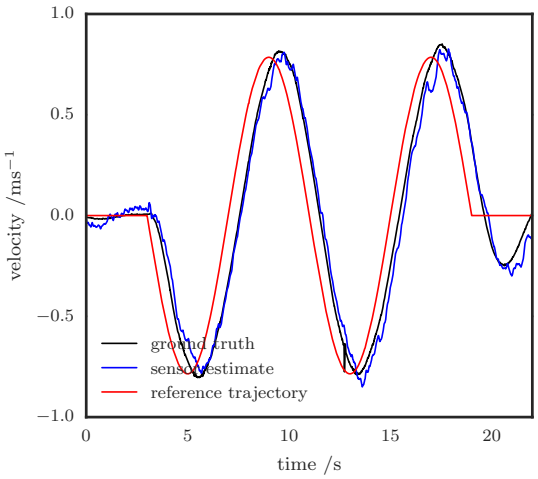

Figure C.11: Sinusoid velocity trajectory using sensor.

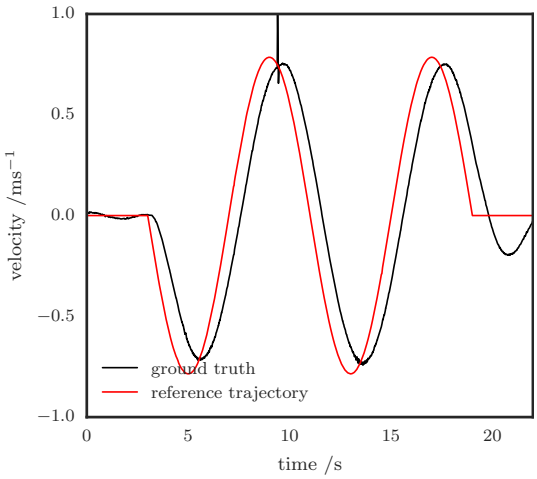

Figure C.12: Sinusoid velocity trajectory using Optitrack.